

Manuel García Pérez

# **MODELING THE EFFECTS OF UNSTEADY FLOW PATTERNS ON THE FIRESIDE ASH FOULING IN TUBE ARRAYS OF KRAFT AND COAL-FIRED BOILERS**

Thesis for the degree of Doctor of Science (Technology) to be presented with due permission for public examination and criticism in the Auditorium of the Student Union House at Lappeenranta University of Technology, Lappeenranta, Finland on the 22<sup>nd</sup> of October, 2016, at noon.

Acta Universitatis  
Lappeenrantaensis 715

Supervisor Esa Vakkilainen  
LUT School of Energy Systems  
Lappeenranta University of Technology  
Finland

Reviewers Markus Bussman  
Mechanical & Industrial Engineering  
University of Toronto  
Canada

Antti Oksanen  
Department of Chemistry and Bioengineering  
Tampere University of Technology  
Finland

Opponent Seppo Korpela  
Department of Mechanical and Aerospace Engineering  
Ohio State University  
United States

ISBN 978-952-335-000-7  
ISBN 978-952-335-001-4 (PDF)  
ISSN-L 1456-4491  
ISSN 1456-4491

Lappeenrannan teknillinen yliopisto  
Yliopistopaino 2016

## Abstract

**Manuel García Pérez**

Modeling the effects of unsteady flow patterns on the fireside ash fouling in tube arrays of kraft and coal-fired boilers.

Lappeenranta, 2016.

107 pages. Acta Universitatis Lappeenrantaensis 715

Diss. Lappeenranta University of Technology

ISBN 978-952-335-000-7, ISBN 978-952-335-001-4 (PDF), ISSN-L 1456-4491, ISSN 1456-4491

The modeling of ash deposition trends, rates, and shapes has been the target of numerous investigations since slagging and fouling constitute a major penalizing factor in boiler performance. Also, they are the most usual cause of unscheduled downtimes. Unfortunately, the ash deposition is a rather challenging phenomenon to model due to its complicated and multidisciplinary nature which may combine complex species chemistry (ash aerosol formation), mineralogy, ash particle drag and impaction mechanics, and fluid dynamics. This motivates the research of ash deposition models.

Ash deposition issues can be studied by using computational fluid dynamics (CFD). These tools are particularly attractive due to their versatility, although their current state-of-the-art is still somewhat inaccurate and qualitative, as it has been pointed out by some authors. It is certainly challenging and ambitious to achieve satisfactory fouling predictions. This thesis presents a CFD model for ash deposition trends and deposit shape predictions. The model has been used with the aim to explain relevant fouling phenomena in kraft and coal-fired boilers. Special care has been taken regarding an accurate solving of the flow patterns around tube arrays and on the necessary grid resolution for proper discrete particle trajectory tracking. The necessity for unsteady flow simulation is emphasized, remarked and justified due to the swinging flow patterns.

The model validity was tested with some experimental work. The challenges which arose regarding the implementation and determination of the original phenomena are pointed out and detailed, as well as a comparison between the experimental and modeled results. Especially, a proper determination of the thermal conductivity and the solid fraction or porosity of the deposits are essential for reliable model results.

Thermophoresis was found to be the main impaction mechanism for submicron particulate. On the other hand, it becomes negligible for larger particles (from 3 microns and larger) whose arrival rates are mainly influenced by inertial impaction. In addition, the importance of accurate flow solving was remarked by non-uniform distributions of particle sticking efficiency and arrival rates around the tube perimeters. The self-limiting nature of fouling (i.e., fouling rates tend to decrease with the time) is briefly quantified and explained. The deposit growth over relatively long fouling times is simulated and studied with the usage of dynamic mesh routines.

Keywords: ash, boilers, combustion, thermophoresis, CFD, fouling, unsteady flow



*Thank you, Masha*



# Contents

**Abstract**

**Acknowledgements**

**Contents**

<b>List of publications</b>	<b>11</b>
<b>Nomenclature</b>	<b>13</b>
<b>1 Introduction</b>	<b>17</b>
1.1 Background and problem statement .....	17
1.2 Objectives and methods.....	18
1.3 Outline of this thesis.....	22
<b>2 Background</b>	<b>23</b>
2.1 Brief overview of ash deposition research.....	23
2.2 Ash and deposits in kraft recovery boilers .....	23
2.2.1 Fume .....	24
2.2.2 Carryover .....	25
2.2.3 Intermediate size particles (ISP) .....	25
2.2.4 Deposits .....	25
2.3 Ash particle deposition mechanisms .....	26
2.3.1 Particle inertial impaction.....	26
2.3.2 Thermophoresis.....	28
2.3.3 Brownian motion.....	28
2.3.4 Turbulent eddy impaction.....	28
2.3.5 Growth by condensation and chemical reactions.....	29
2.4 Models for ash deposition.....	29
2.5 This thesis: unsteady model for ash deposition .....	32
<b>3 Modeling unsteady flue gas and ash deposit growth</b>	<b>33</b>
3.1 The solver and other main model guidelines .....	33
3.2 Meshing guidelines .....	33
3.3 Discrete particle tracking and impaction modeling .....	35
3.4 Deposit growth model .....	36
3.5 Setting up a dynamic mesh in Ansys FLUENT.....	38
3.6 Model strategy.....	39
<b>4 Findings and contributions</b>	<b>43</b>
4.1 On the unsteadiness of the flow patterns .....	43
4.2 On the flow patterns and particle trajectories past tube arrays.....	45
4.3 On particle deposition trends .....	47
4.3.1 Particle size and flow effects on thermophoresis .....	48

4.3.2	Particle size effects on stickiness .....	49
4.4	On fume fouling of transversally-periodic four-tube bundles .....	49
4.4.1	Effect of the transverse tube spacing .....	50
4.4.2	Long-term unsteady fouling rates .....	50
4.4.3	Particle size effects on fouling .....	50
4.4.4	Fouling model comparisons and model complexity.....	52
4.5	On the particle-wise determination of the Cunningham effect.....	54
4.6	On the ash particle behavior on a staggered tube array.....	55
<b>5</b>	<b>Validation</b> .....	<b>57</b>
5.1	Introduction.....	57
5.1.1	Case study .....	57
5.1.2	Previous considerations and uncertainties .....	58
5.1.3	On notation.....	59
5.2	The mesh and the solver .....	60
5.3	Boundary conditions and injection of particles .....	61
5.3.1	Upstream longitudinal gas velocity and temperature .....	61
5.3.2	Ash particles size distributions and discrete injections .....	62
5.3.3	Other boundary conditions.....	64
5.4	Properties of materials .....	65
5.4.1	Properties of ashes and deposits.....	65
5.4.2	Gas properties.....	66
5.4.3	Sticking model properties .....	66
5.5	Fouling model characterization.....	66
5.5.1	Dynamic mesh parameters.....	66
5.5.2	Sample duration.....	67
5.5.3	Time-dependent inlet conditions .....	68
5.5.4	Mass spreading parameters .....	68
5.6	Results and discussion .....	69
5.6.1	On the heat transfer rates .....	69
5.6.2	On the deposit shapes .....	73
5.7	On the limitations of the model.....	75
<b>6</b>	<b>Conclusions</b> .....	<b>77</b>
<b>Appendix A: Outline of the particle sticking—rebound model</b>		<b>81</b>
A.1	Relevant magnitudes and definitions .....	81
A.1.1	Particle magnitudes .....	81
A.1.2	Material and surface properties.....	82
A.1.3	Surface properties.....	82
A.1.4	Critical impact angle.....	83
A.2	Mechanistic model for non-oblique impacts .....	83
A.2.1	Starting parameters and definitions .....	83
A.2.2	Stored mechanical energy and contact radius .....	84
A.2.2.1	Case of purely elastic particle deformation .....	84
A.2.2.2	Case of plastic-elastic particle deformation.....	85





---

## List of publications

This thesis is based on the following articles, which are referred to in the text by using the Roman numerals I—VII. The rights have been granted by the publishers to include these publications in this dissertation, except for Paper [VII] which was under review at the moment of the defense.

- I. García Pérez, M., and Vakkilainen, E. (2014). CFD model for prediction of initial fume deposition rates in the superheater area of a Kraft Recovery Boiler. In: *Proceedings of the 27<sup>th</sup> International Conference on Efficiency, Cost, Optimization, Simulation and Environmental impact of Energy Systems*. Turku, Finland; 15—19 June.
- II. García Pérez, M., Vakkilainen, E., and Hyppänen, T. (2015). 2D dynamic mesh model for deposit shape prediction in boiler banks of recovery boilers with different tube spacing arrangements. *Fuel*, 158: 139—151.
- III. García Pérez, M., Fry, A., Vakkilainen, E., and Whitty, K. J. (2016). Fouling analysis of the convective section of a pilot-scale combustor firing two different subbituminous coals. *Energy & Fuels*, in Press.
- IV. García Pérez, M., Vakkilainen, E., and Hyppänen, T. (2016). Unsteady CFD analysis of kraft recovery boiler fly-ash trajectories, sticking efficiencies and deposition rates with a mechanistic particle rebound-stick model. *Fuel*, 181: 408—420.
- V. García Pérez, M., Vakkilainen, E., and Hyppänen, T. (2016). A brief overview on the drag laws used in the Lagrangian tracking of ash trajectories for boiler fouling CFD models. In: *Proceedings of the 26<sup>th</sup> International Conference on Impacts of Fuel Quality on Power Production*. Prague, Czech Republic; 19—23 September.
- VI. García Pérez, M., Vakkilainen, E., and Hyppänen, T. (2016). Fouling growth modeling of kraft recovery boiler fume ash deposits with dynamic meshes and a mechanistic sticking approach. *Fuel*, 185: 872—885.
- VII. García Pérez, M., Vakkilainen, E., and Hyppänen, T. (2016). The contribution of differently-sized ash particles to the fouling trends of a pilot-scale coal-fired combustor with an ash deposition CFD model. Submitted to *Fuel*, 20<sup>th</sup> of August of 2016.

I am the principal author and investigator in all the aforementioned publications. Esa Vakkilainen participated actively as technical advisor providing guidance, ideas and valuable interpretations of the results in all these publications.

Timo Hyppänen contributed with valuable improvements, suggestions and strategies towards more scientifically rigorous approaches of this work and towards a clearer text interpretations for Papers [II, IV—VII].

Paper [III] was elaborated from laboratory work in the Combustion Research Facility of the University of Utah, in Salt Lake City in 2015. The laboratory director Andrew Fry supervised the combustor operation providing the researchers with materials, coal definitions, combustor technical data and usage guidelines, ideas, and procedures. He also suggested ideas for results interpretation. Kevin Whitty supervised the entire work, facilitated the SEM analysis of the ash samples and participated actively in the manuscript elaboration with improvements, suggestions, and valuable ideas.

### Relevant conference proceedings not included in this thesis:

- García Pérez, M., Vakkilainen, E., and Hyppänen, Timo. (2014). CFD for deposit formation in kraft recovery boilers. In: *Proceedings of the 50<sup>th</sup> International Chemical Recovery Conference*. Tampere, Finland, 2—6 June.
  - Brief review of kraft recovery boiler ash deposition: formation, models, research, practices. The dynamic mesh model proposed in this thesis is introduced and presented in this paper.
- García Pérez, M., and Vakkilainen, E. (2014). 2D Dynamic mesh model for deposit shape prediction in boiler bank of recovery boiler with different tube spacing arrangements. In: *Proceedings of the 10th International Conference on Heat Transfer, Fluid Mechanics and Thermodynamics*. Orlando, USA, 14—26 July.
  - This manuscript is an earlier conference article version of Paper [II].

## Nomenclature

In the present work, scalar variables and constants are denoted using *italics style*, vectors are denoted using an upper arrow ( $\vec{x}$ ), and abbreviations are denoted using regular style.

Note: the units shown in this list's right column correspond only to International System base or derived units in their standard prefix, although in the text other International System accepted or derived units (such as °C, or minutes) or with prefixes (such as  $\mu\text{m}$ , kPa) are used at convenience. Nonetheless, the units shall always be explicitly specified in the text (except for dimensionless numbers, fractions and ratios).

### Latin alphabet

$\vec{a}$	mesh face area vector of the deposit, pointing towards the gas	$\text{m}^2$
$A$	heat transfer exchange surface	$\text{m}^2$
$c$	size distribution parameter (for a Rosin-Rammler distribution)	—
$C_L$	tube lift coefficient	—
$C_m$	ratio of affected deposit mass to hitting particle mass	—
$c_p$	flue gas specific heat at constant pressure	$\text{J}\cdot\text{kg}^{-1}\cdot\text{K}^{-1}$
$D$	diameter (tube)	$\text{m}$
$d_p$	diameter (particle)	$\text{m}$
$\bar{d}$	mean particle size (for a Rosin-Rammler distribution)	$\text{m}$
$E$	Young modulus	$\text{Pa}$
$E$	energy (at particle impaction), requires subscript	$\text{J}$
$e$	restitution coefficient (for particle rebound)	—
$F$	force	$\text{N}$
$f$	deposit surface friction coefficient	—
$H$	transverse height of computational domain	$\text{m}$
$H_v$	material Vicker's indentation hardness	$\text{Pa}$
$h$	convective heat transfer coefficient	$\text{W}\cdot\text{m}^{-2}\cdot\text{K}^{-1}$
$k$	thermal conductivity	$\text{W}\cdot\text{m}^{-1}\cdot\text{K}^{-1}$
$m$	mass of deposited material	$\text{kg}$
$\dot{m}$	mass flow rate (of a particle stream)	$\text{kg}\cdot\text{s}^{-1}$
$n$	number of steps of the deposit growth	—
$\vec{n}$	deposit surface normal unitary vector	—
$p$	mass spreading factor	—
$\dot{q}$	heat transfer rate (per unit of perpendicular length of 2D model)	$\text{W}\cdot\text{m}_\perp^{-1}$
$\dot{Q}$	heat transfer rate	$\text{W}$
$R_{cd}$	conductive heat transfer resistance	$\text{m}^2\cdot\text{K}\cdot\text{W}^{-1}$
$\vec{r}$	node displacement vector	$\text{m}$
$r$	radius (multiple uses depending on required subscript)	$\text{m}$
$s$	tube spacing (requires subscript)	$\text{m}$
$\Delta t$	flow time-step	$\text{s}$

$\vec{t}$	deposit surface tangential vector	—
$T$	temperature	K
$T_k$	kinetic energy loss (of a rebounding particle)	—
$U$	global heat transfer coefficient	$\text{W} \cdot \text{m}^{-2} \text{K}^{-1}$
$u, \vec{u}$	velocity (fluid)	$\text{m} \cdot \text{s}^{-1}$
$v, \vec{v}$	velocity (particle)	$\text{m} \cdot \text{s}^{-1}$
$\Delta V$	increase volume of deposit, per unit of tube length	$\text{m}^3 \cdot \text{m}_L^{-1}$
$\Delta x$	mesh cell length or side	m
$\Delta y$	mesh cell height	m
$Y$	uniaxial yield stress	Pa
$Y_d$	mass fraction of particles below a given diameter	—

### Greek alphabet

$\gamma$	surface energy	$\text{J} \cdot \text{m}^{-2}$
$\Gamma$	surface work of adhesion	$\text{J} \cdot \text{m}^{-2}$
$\delta$	tube angular coordinate	rad
$\varepsilon$	deposit solid fraction (one minus the porosity)	—
$\theta$	particle trajectory angle with surface impaction surface	rad
$\lambda$	maximum internal plastic stress to uniaxial yield ratio	—
$\mu$	dynamic viscosity	$\text{kg} \cdot \text{s}^{-1} \text{m}^{-2}$
$\nu$	Poisson's ratio	—
$\xi$	under-relaxation factor	—
$\pi$	the mathematical constant $\pi = 3.14159\dots$	—
$\rho$	density, of the fluid if not otherwise specified with subscript p	$\text{kg} \cdot \text{m}^{-3}$

### Dimensionless numbers

C	Courant number
Nu	Nusselt number
Re	Reynolds number
Stk	Stokes number

### Superscripts

\* effective (for particle contact mechanics)

### Subscripts

1	first cell adjacent to a deposition surface
a	area (for the particle-gas and particle-deposit surface energies)
c	contact (for particle contact radius)
cr	critical (regarding Konstandopoulos' critical incidence angle)
el	elastic
g	flue gas

---

i	inertial (for the forces over a particle)
I	incident (before particle impaction)
k	kinetic
lim	limit
l	longitudinal (tube spacing)
loss	loss (for particle energy loss due to plastic deformation)
m	model
n	normal (perpendicular direction to the deposit surface)
out	outer boundary of the domain (for the temperature)
p	particle
pl	plastic
R	rebound (after particle impaction)
t	transverse (tube spacing)
t	tangential (for a particle impact in a deposit)
th	thermophoresis
tot	total (for the particle contact radius in a plastic-elastic deformation)
$\infty$	upstream conditions (for flue gas temperature and velocity)

**Abbreviations**

2D	two dimensional
3D	three dimensional
CFD	computational fluid dynamics
Eq.	equation
LTD	logarithmic temperature difference
ISP	intermediate size particle
KRB	kraft recovery boiler
UDF	user-defined function



# 1 Introduction

## 1.1 Background and problem statement

Ash deposition issues are of major importance in industrial boilers of any kind, up to a point that they determine certain aspects of their design. Baxter [1] stated that the understanding and modeling of the inorganic material combustion, ash formation and depositions are less understood than the organic material combustion.

As a result, there is great interest in developing a better understanding of how fouling occurs, aiming to find strategies to predict and reduce it. Unfortunately, experiments in operating boilers are challenging to conduct, and so modeling is attractive, yet also difficult, as fouling is a very complex phenomena which involves a variety of physics. The present thesis deals with ash deposition modeling issues and challenges in coal-fired boilers and, with some more emphasis, in kraft recovery boilers (KRB).

Since their invention in 1934, KRB have been used in the pulp and paper industry. As a part of the kraft pulping process, KRB allow for the recovery of inorganic cooking compounds which are necessary for fiber extraction and further cyclical reutilization. They also provide the necessary process energy by generating steam for the mill. Unfortunately, KRB tend to suffer particularly from ash deposits due to the large ash content in black liquor, as discussed by Vakkilainen [2] and Adams *et al.* [3], when compared to other fuels. Fouling and slagging are the most usual causes of industrial boiler unplanned shutdowns. In addition, these fireside deposits impose a resistance on the overall heat transfer, which is reduced penalizing the boiler efficiency, thus causing serious economic losses [4]. Moreover, these deposits may plug the flow area and also lead to tube corrosion issues [3]. Figure 1.1 shows photographs of deposits in a KRB.



Figure 1.1: Deposits observed during a KRB shutdown. Left: Fouling between the boiler bank and the boiler bank screen. The deposits on the leading edge were close to plug the whole space between them. Right: Superheater area, with molten-ash deposits (slagging).

Pulverized-coal boilers suffer from ash deposition as well. These issues could be illustrated by the subbituminous coal-fired boilers being around a 70 % larger than a bituminous coal-fired boiler, for a similar input power, as pointed out by Baxter [1]. As they are often used as power production units, the performance penalty caused by ash depositions entails a certain environmental impact. This is why ash deposition and other related problems (economic impacts, tube corrosion, and dependence on fuel blending) is a very active research topic.

For the aforementioned reasons, proper understanding and prediction capabilities about fouling are required for proper boiler design and operation. However, the large quantity of factors involved complicates the estimation of the boiler performance. The fuel properties, boiler design and operation affect the ash deposition in a complex manner to an extent that predicting tools and models are, unfortunately, still considered to be in an early stage and marginally accurate [1, 5].

## 1.2 Objectives and methods

This study makes use of a computing fluid dynamics (CFD) model for fouling prediction in boiler tube arrays acknowledging the unsteady nature of the flue gas flow patterns and its effects on the fine ash particle trajectories. Some improvements and enhancements are presented, tested, and proposed. A particular enhancement of the models, which is aimed to predict and simulate the growth rates with the use of dynamic meshes for the deposits, is studied in deeper detail.

These models are tested with the target of explaining certain observed flow phenomena which are present in boiler tube arrays and their fouling issues. Regarding flow and fouling, the targets of the present work may be summarized by the following questions

- How time-dependent is the flow? Under which conditions could steady-state simulations be acceptable? How do these flow patterns develop over the tube arrays? How are the ash particle trajectories affected by these flow patterns?
- How do the deposition rates and deposit formation vary with the time? How does fouling affect itself? Are the fouling rates stable with the time, or do they change as the tubes becomes fouled?
- Are there differences among the deposition trends at different tubes of a row? Are the particle sticking probability and fouling rate uniform within a tube perimeter?
- What are the effect that thermophoresis, turbulence, inertia, and other deposition mechanisms have on the deposition trends? Also, how may the design parameters (flue gas temperature, velocity, tube arrangements) affect these deposition trends?
- How are the particles dragged within the flue gas? How do differently-sized particles behave regarding their deposition magnitudes?

---

This work focuses also on the modeling issues and challenges which arise naturally when trying to refine the methods for predicting ash deposition. The following questions outline the objectives of this work regarding the modeling of fouling processes:

- How do current CFD investigations for ash deposition handle accuracy requirements (mesh resolution, time-step length)? How fine must the grids be?
- What must be considered when modeling the deposit growth by means of dynamic meshes? What possibilities do they offer, what challenges do they present?
- How complex do models need to be? How reliable are the common used modeling approximations (stationary fluid flow, grid resolution, sticking models, etc.)? May their reliability be case-dependent?
- How long should the calculated fouling cycles take, in terms of simulated flow time? What kind of considerations should be taken if the deposition results over a few flow oscillations are extrapolated to longer periods of several minutes?
- What challenges and issues arise when trying to implement these models to predict ash deposits and heat transfer performance? What considerations must be taken? What are the critical model parameters and material properties affecting the results?

The articles included in this dissertation aim to answer these questions. A list of these publications was given in page 11 and are appended at the end of this thesis. Paper [I] presented CFD simulations which account for the particle arrival rates to probes with different tube arrangements. Constant particle sticking probability was assumed. The results were contrasted to empirical field data of ash deposition in KRB. The unsteadiness of the flow patterns past those different tube geometries (superheater plates vs. tube rows) was analyzed.

Further development of Paper [I] is presented in Paper [II], to account for the deposit growth in a KRB boiler bank. Issues regarding the dynamic-mesh usage for fouling prediction were addressed. The high computational cost of this model was pointed out and strategies to circumvent it were suggested. The effect of the transverse tube pitch  $s_t$  of a transversally-periodic row of four tubes was studied. The deposition among different tubes was compared.

The CFD model is further enhanced with a mechanistic particle-sticking model proposed by van Beek [6], which is slightly modified and adapted to account for particles with oblique impaction angles as pointed out by Konstandopoulos [7]. This allowed for the determination of the particle behavior upon its arrival to a tube and of the fouling trends depending on their size (addressed along with a flow pattern study in Paper [IV]).

In Paper [V], the particle drag laws recommended by CFD User's guides are reviewed and criticized. The limitations of those laws are highlighted. A newer drag law, which is especially suitable for small particles, is proposed and tested.

Paper [VI] is an improved version of the dynamic mesh model of Paper [II] enhanced with a better grid resolution, the sticking-rebound model used in Paper [IV], and the drag law suggested in Paper [V]. The model presented in Paper [VI] is the most advanced version of the tool proposed in this dissertation.

Experimental fouling measurements were carried out in a lab-scale 100-kW coal-fired combustor. This study is reported in Paper [III] and the results are used to test the validity of the final model used in Paper [VI] and proposed in this thesis. This validation attempt is detailed in Chapter 5. In addition, Paper [VII] simulates the conditions of these empirical measurements to study the behavior of differently-sized particles and the flow velocity on a complete tube array, which had not been performed so far in the previous publications. The methodologies were similar to the ones used in Papers [IV, V]

The models in publications [IV—VII] accounted for numerical accuracy guidelines suggested by Weber *et al.* [5, 8].

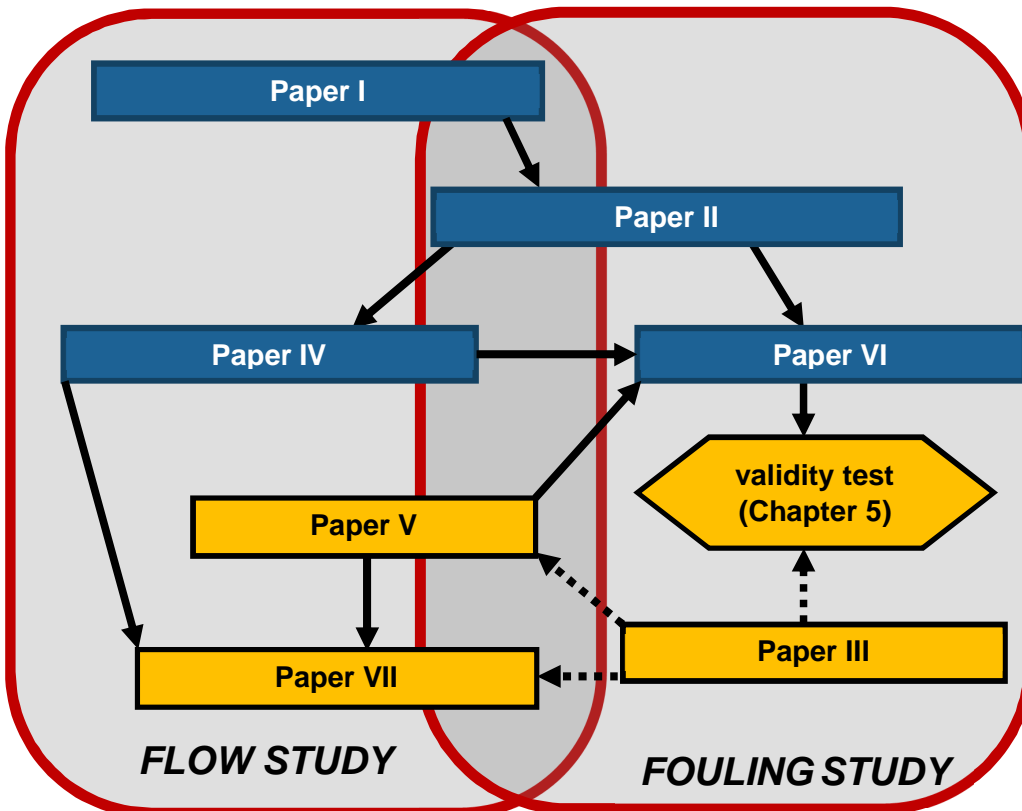


Figure 1.2: Overview of the appended publications and their relation, along with the study reported in Chapter 5. Blue boxes are articles related to kraft recovery fume. Orange boxes are works related to pulverized coal ash. Full arrows denote modeling improvement or application. The dashed arrows coming from Paper [III] denote the usage of its empirical data.

The aforementioned papers included in this thesis could be classified between two main research targets, namely: the flow fields in tube arrays and the fouling itself. Figure 1.2 sketches roughly the relations among the articles.

A more formal and precise compendium of the objectives and methods is provided below for each one of the publications included in this thesis:

Paper I: *CFD model for prediction of initial fume deposition rates in the superheater area of a Kraft Recovery Boiler.*

Objectives: The study of the particle-laden flow patterns over different boiler tube geometries (platen and tubed). Emphasis is placed on the unsteadiness of the flow.

Methods: Development of the unsteady (time-dependent) CFD ash deposition preliminary model. Comparison with empirical field measurements performed previously at a Finnish kraft recovery boiler.

Paper II: *2D dynamic mesh model for deposit shape prediction in boiler banks of recovery boilers with different tube spacing arrangements.*

Objectives: Study of the tube spacing effects on the fouling of a transversally-periodic two-dimensional tube array, simulating the boiler banks of a typical kraft recovery boiler. Dynamic mesh model statement and presentation.

Methods: Development and presentation of the CFD model with dynamic meshes that simulate the ash layer growth. The strategy and other model issues are addressed.

Paper III: *Fouling analysis of the convective section of a pilot-scale combustor firing two different subbituminous coals.*

Objectives: Analysis of ash deposits and measurement of their thickness after more than 15 hours of monitored combustor operation for coal test campaigns. The collected data should be of use for a qualitative model validation.

Methods: Laboratory work on a pilot scale 100-kW coal-fired combustor. The ash deposits of the convective heat exchangers were examined after the test were completed.

Paper IV: *Unsteady CFD analysis of kraft recovery boiler fly-ash trajectories, sticking efficiencies and deposition rates with a mechanistic particle rebound-stick model.*

Objectives: Detailed study of the flow patterns over a tube array and their effects on the deposition of differently-sized ash particles. More detailed study of the deposition mechanisms. Sticking and deposition trends as a function of the particle properties.

Methods: Enhancement of the previous CFD model with better numerical accuracy (grid resolution) and a mechanistic sticking submodel. Emphasis on particle fate statistics regarding sticking or rebound in different tube surfaces.

Paper V: *A brief overview on the drag laws used in the Lagrangian tracking of ash trajectories for boiler fouling CFD models.*

Objectives: A review of the traditional drag laws. To study and to understand the particle slip within the flow, and the Cunningham correction. A critic analysis of the typical

implementations of the drag laws in CFD packages. Elaboration of a newer drag law which should be suitable for particles of different sizes (i.e., for particle distributions).

Methods: Literature review of the studies done on spherical particle drag within rarefied flows. Development of a newer drag law, which combines the Cunningham correction with the previous standard drag law. Test this new proposed drag law and contrast it with the formulation proposed in CFD packages user's guides and documentation.

Paper VI: *Fouling growth modeling of kraft recovery boiler fume ash deposits with dynamic meshes and a mechanistic sticking approach.*

Objectives: More accurate study of the fouled layer growth, with emphasis on the unsteady nature of fouling. Study the effects of the average fume particle size on deposit shapes. Considerations regarding necessary model complexity are addressed.

Methods: Development of an ash deposit growth CFD model by combining the original primitive model of Paper [II] with the improvements of Papers [IV, V]. The solutions yielded by both approaches are contrasted.

Paper VII: *The contribution of differently-sized ash particles to the fouling trends of a pilot-scale coal-fired combustor with an ash deposition CFD model.*

Objectives: Study of the effects of the flow inlet velocity. Study of the behavior of the different particles as a function of their diameter. Study the deposition rates over a complete tube array. Contrast the deposition on clean tubes vs. on fouled tubes.

Methods: Execution of a newer CFD model (similarly as the one in Paper [IV] with the drag law of [V]), which is used to implement the particle size distributions, the flow properties, and heat exchanger which were empirically studied in Paper [III]. Diameter-wise analysis of the particle impaction log. Use of normalized magnitudes for particle behavior understanding.

### 1.3 Outline of this thesis

Chapter 2 presents a deeper introduction to fouling phenomena and a brief review of the current state-of-the-art of fouling modeling, with emphasis in KRB. Chapter 3 describes the features and requirements for the model set-up, highlights relevant considerations and also sketches the strategies to be followed. Chapter 4 highlights the key findings of this work and provides explanations about fouling phenomena. Chapter 5 applies the deposit growth model presented here to the conditions of the measurements presented in [III], aiming to contrast the modeled values with experimental data and to test its validity. Concluding remarks are given in Chapter 6.

Appendix A details the algorithm of the particle sticking model used in Papers [IV—VII], and Appendix B contains general information about the behavior and handling of the dynamic mesh model used in [II, VI] and in Chapter 5. The information included in these appendixes is relevant and could not be included in whole in the publications for sake of space.

---

## 2 Background

### 2.1 Brief overview of ash deposition research

Ash formation and deposition, as well as deposit properties, are the current target of numerous scientific investigations, some of which, for instance, focus on global aspects of the phenomena. Bryers [4] studied the ash formation and deposition regarding their causes (ash and impurities in the fuel) and final implications (performance penalties and costs). This research stated that the per-facility economic costs of fireside deposit-related issues could vary from several thousand US dollars per year (if only heat transfer surface cleaning is needed) up to several million (if significant mismatches between design and operation performances occur). Overall, it was estimated that these incidents cost yearly the global utility industry four billion dollars (year 1988). Alternatively, some researchers focus more on empirical reports on the nature and properties of the deposits [1, 9] as well as on ash aerosol formation [1, 10–12].

On the other hand, other investigations emphasize on more specific aspects of ash deposits. As an example, a study by Schumacher and Juniper [13] stated that certain critical slagging regions exist in burner-fired boilers: particularly large slag deposits tend to appear in the near-burner zones (entailing a risk of plugging of the combusting mixture path), under the boiler nose, and around the hopper. For the heat exchangers in the backpass, the transverse spacing was set as key parameter in order to prevent excessive deposits and bridging.

The effects of inorganic chemistry and mineralogy in deposits are also a target of research. Weber *et al.* [5] and Creelman *et al.* [14] remarked the need for mineralogical tools and databases for an appropriate understanding of deposit behavior in boilers. Image analyses of deposits by Juniper *et al.* [15], and own work [III] have highlighted the complicated mineralogical configuration and distribution in deposits: the physical properties of the deposit material depend on the formation of minerals within itself, which can be as varied as, e.g., mullite, quartz, feldspar, cristobalite or iron oxides.

Additional work is carried out regarding ash property models. Shiai *et al.* [16] developed a correlation-based model to predict ash properties from the coal characteristics. The results were reasonably accurate about the ash particle density, specific surface area, size, and shape, among others. This kind of tools may be of great usefulness for developing further deposition models, or for operation and design.

### 2.2 Ash and deposits in kraft recovery boilers

Numerous studies and reports on KRB fouling have been carried out in the past due to its particularly challenging operation. Effort was made towards a good comprehension of this challenge resulting in numerous approaches, fuel studies, predicting models and cleaning techniques in order to estimate and tackle fouling and slagging.

### 2.2.1 Fume

The burning of black liquor droplets leads to alkali salt vaporization. These vaporized salts cool down and/or react with furnace gases. They end up by condensing or coalescing into small particles called fume. Their diameter typically falls between 0.5 and 5  $\mu\text{m}$  (Figure 2.1) [17]. This size is determined by the fuel and combustion conditions in the furnace, since measurements by Mikkanen *et al.* [18] and Baxter *et al.* [19] have proved that the mean particle size does not vary significantly through the boiler. Frederick *et al.* [20] noted that agglomerates tend to form and that the deposits may sinter. After sootblowing, some agglomerates re-enter the flue gas stream. These clusters of particles could be as large as 20–30  $\mu\text{m}$ .

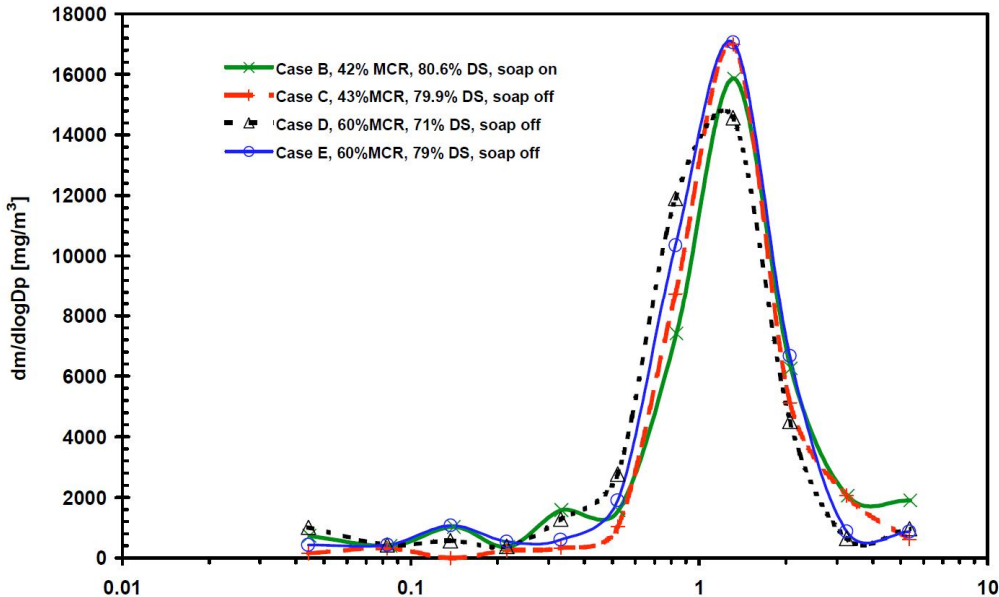


Figure 2.1: Fume ash size concentration of dust samples collected before an electrostatic precipitator at different operating conditions. Janka *et al.*, [17].

Fume is the most significant ash component in the flue gas of a KRB. In the electrostatic precipitator, most of the retrieved ash is fume. The fume formation has been found to depend on the mass rate of fired black liquor by Tamminen *et al.* [21] and on the furnace temperature by Leppänen *et al.* [22]. Additionally, the fume concentration has also been observed to increase with the dry solids concentration in the black liquor. On-site measurements in boilers yielded that typical fume concentration in the flue gas fall between 10 and 35  $\text{g}/\text{Nm}^3$  [2].

The condensation of alkali vapors is often favored by the presence of impurities (typically metal oxides), constituting a propitious environment for heterogeneous nucleation. The

formed condensation nuclei grow until they reach a uniform stable size, typically significantly less than 10  $\mu\text{m}$ .

### 2.2.2 Carryover

Droplets of black liquor tend to swell upon combustion. The increase in volume leads to a decrease in density, making it possible for the flue gas to drag and carry away these droplets. These particles entrained in the main flue gas current are called carryover. Droplets that eventually become carryover have a typical diameter around 1 mm (Vähä-Savo *et al.*, [23], Horton and Vakkilainen [24]).

Costa *et al.* [25] noted that the quantity of carryover depends strongly on the air flow settings and on the chosen air injection system. In modern firing systems, Kaila and Saviharju [26] show that the carryover in flue gas reaches a typical concentration of 2—4  $\text{g}/\text{Nm}^3$ , whereas older conventional systems may present values as high as 5—8  $\text{g}/\text{Nm}^3$  according to Mettiäinen [27].

It is possible to classify carryover into two types. Some particles have still carbon burning when they travel across the bullnose. As the flue gas temperature decreases suddenly the combustion may stop, leaving some unburnt char inside, resulting in a black particle. On the other hand, those other particles that have burnt completely are particularly rich in sodium sulfide. These particles have a pink or red color. This last type of carryover is more typical than the first one, especially in modern boilers where good air injection systems ensure improved combustion efficiencies.

### 2.2.3 Intermediate size particles (ISP)

The particles with size between several microns and 1 mm are very diverse and they are formed from different sources. Some large agglomerates of fume particles may sinter in a tube deposit, and be re-entrained again into the main flow stream, for instance, either by just detaching from surfaces because of the flow drag or by sootblowing. Other particles may be formed from small char fragments entrained in the flow. Other ISP may come from the entrainment of solids directly from black liquor droplet combustion. Robers *et al.* [28] propose that the ISPs do not represent a significant fraction of ash forming particles in the gas.

### 2.2.4 Deposits

Owing to the characteristic impaction mechanisms of different particles (which shall be discussed later), the composition of deposits falls between those of carryover and fume as noted by Janka *et al.* [29]. The deposits in different places of the boiler are constituted by different ratios of mixture of carryover and fume. Due to the inertial impaction, the carryover tends to hit mainly the leading edges of the pipes, and it hardly ever hits the lees. This is why carryover is dominant in the deposits of the superheater area. As the flue

gas travels, carryover is screened away by the heat transfer surfaces or it falls on the ash collectors. After this the fume particles acquire a larger share of the deposit compositions. As a result, the composition of a fouling deposit varies from that of the carryover to the one of the fume as we approach the electrostatic precipitator, where the collected ashes may even not present carryover at all. Figure 2.2 highlights this phenomenon.

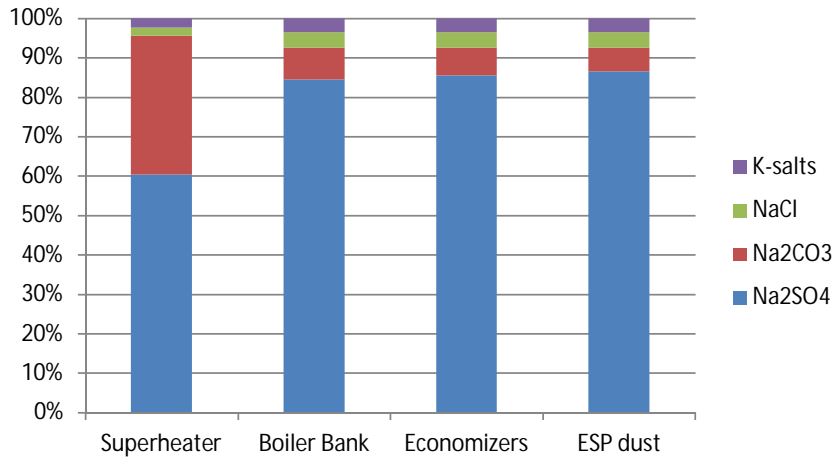


Figure 2.2: A typical composition of deposits of a KRB (Adams *et al.*, [3]). The carryover particle composition may be identified as the superheater composition. On the other hand, the ESP dust can be assumed to be essentially fume. It can be concluded from the figure that carryover is not a major deposit component beyond the superheater area.

## 2.3 Ash particle deposition mechanisms

There exist different physical phenomena involved in the motion of a particle. A particle does not move exactly along with the flow. Hence, it may arrive to a tube surface instead of having avoided it. These mechanisms are of different nature and may affect specific ranges of particles separately.

### 2.3.1 Particle inertial impaction

From the flue gas point of view, a heat transfer surface (a tube or a furnace wall) is an obstacle along a straight trajectory which the flue gas surrounds and avoids. In this process, the gas exerts a drag force on the particulate which might or might not be enough to deviate them. Hence, the entrained particles may not follow the streamlines strictly.

A heavy particle travelling with the fluid possesses a relatively high inertia which makes the particle unable to respond quickly to changes in the flow velocity. Therefore, these large particles hit the wind side of the obstacle in their way. This is called inertial impaction. The particle Stokes number is typically addressed as the tendency of a particle to maintain itself in a straight trajectory, not deviating to avoid an obstacle [5, 30]:

$$\text{Stk} = \frac{\rho_p d_p^2 v_p}{9\mu D}, \quad (2.1)$$

where  $\rho_p$ ,  $d_p$ , and  $v_p$  stand for particle density, diameter, and upstream velocity magnitude (before being affected by the presence of the tube).  $\mu$  is the gas dynamic viscosity and  $D$  the tube diameter. The Stokes number is essentially the ratio of the characteristic time of a particle to the characteristic time of the flow over an obstacle. Also, it may be interpreted as the ratio of the particle stopping distance to the characteristic obstacle dimension. Particles with a large Stokes number are unable to detach with the flow from its path to avoid the pipe. A Stokes number much smaller than the unity implies that the particle tends to follow the stream lines well, thus being able to avoid the obstacle. This is the case of finer fume particles, which typically do not deposit through inertial impact as much as carryover (this is highlighted in Figure 2.3).

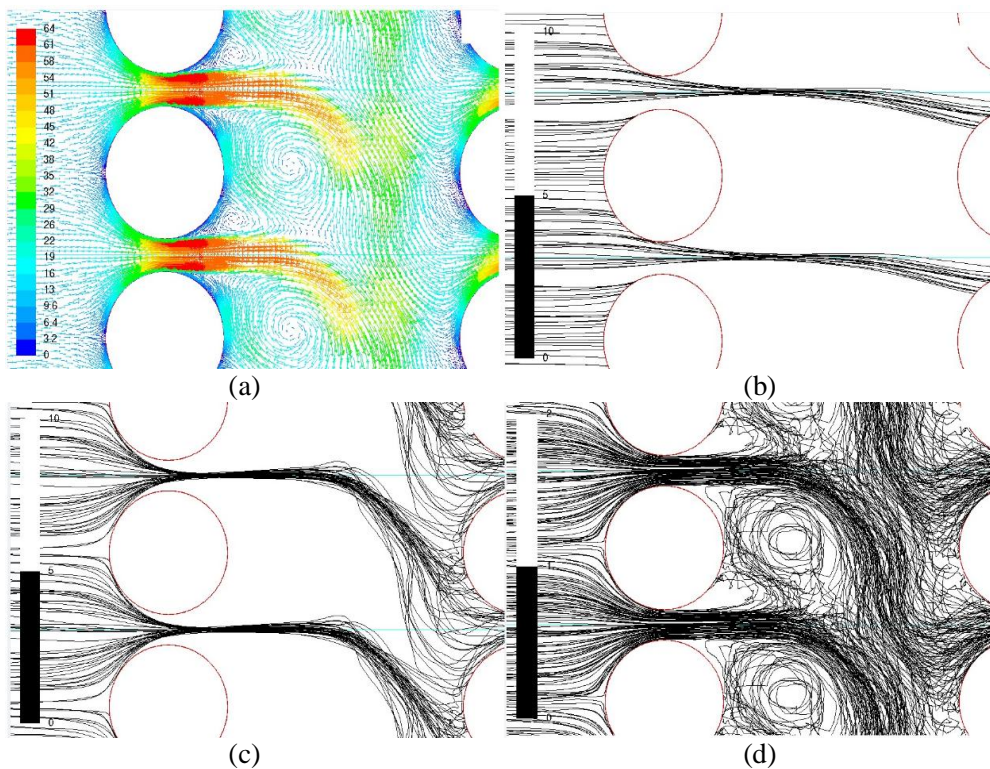


Figure 2.3: Modeled 2D cut of a periodical tube array laden with differently-sized particles. a): velocity field at a given moment between first two tubes of an array. Notice the presence of unsteady and non-symmetrical vortices. b): Trajectories of 0.05 mm particles (carryover) with  $\text{Stk} = 4.34$ . They are unable to avoid obstacles and barely deviate from the flow. c): Trajectories of 0.01 mm particles (ISP), for which  $\text{Stk} = 0.17$ . Some avoid the obstacle but are not able to follow the sudden changes in the gas trajectories, impacting on the second tube. d): Trajectories of 0.7  $\mu\text{m}$  particles (fume),  $\text{Stk} = 8.51 \cdot 10^{-4}$ . They mostly avoid the first tube and enter the vortex. Small turbulent eddies lead to a tortuous trajectory.

Some investigations, notably Israel and Rosner [31] and Wessel and Righi [32], suggest different correlations of the impaction efficiency (the ratio of the quantity of particles that do impact an obstacle to the total quantity of particles which were initially aiming to do it) as a function of a generalized Stokes number for all kind of particles. In [IV] it was found that this sticking probability depends not only on the Stokes number but also on the tube location around its perimeter.

### 2.3.2 Thermophoresis

Thermophoresis is one of the major reasons of fume deposition in the tubes [IV]. In a region under a gradient of temperature, the gas molecule collisions on a particle are more intense on the side of higher temperature than those on the cold side, due to the micro-scale kinetic molecule movements. Therefore, there is a certain driving force in the direction opposite to the temperature gradient. This force can be significant enough to drive small particles towards cold regions. For big ash particles, this effect is not sufficient to alter the path of the particle significantly.

George-Wood and Cameron [33] studied fume formation and deposition in laboratory conditions. They found that the deposition rate (in units of mass per area and time) was directly proportional, among other parameters, to the temperature difference between the bulk flow and the deposition surface. This observation is explained by thermophoresis. One of the objectives of the present thesis is to investigate further the thermophoresis propensity and its effects.

### 2.3.3 Brownian motion

Brownian motion results from the chaotic impactions of the surrounding gas molecules on the particles. At any given moment, a particle may be hit by surrounding molecules more on a certain side than on the opposite side, experiencing a net small pressure fluctuation. This phenomenon differs from thermophoresis in the fact that the direction of the gas molecule hits is random here and the particle motion looks somewhat erratic, not being caused by any macroscopic flow feature. A particle driven only by Brownian motion presents a trajectory which varies chaotically with the time.

This motion can be interpreted as a random diffusion which is macroscopically (or statistically) cancelled, but may be locally significant for some particles if they are driven to deposit onto a surface. Only fine particles may have their paths significantly altered by Brownian fluctuations.

### 2.3.4 Turbulent eddy impaction

A turbulent flow generates and dissipates eddies chaotically. These eddies are fluctuations of the velocity components of the flow. A particle inside the tube boundary layer may be driven to deposit even without net effects of Brownian diffusion due to one of these

eddies. Some eddies which move towards the surface are capable of giving to particles enough momentum to cross the whole viscous boundary layer and deposit eventually.

This mechanism is capable of affecting big particles more significantly. Typically, the smaller a particle is, the greater the turbulent fluctuation of the velocity is required to deposit the particle on a tube surface, as stated by Vakkilainen [2].

### 2.3.5 Growth by condensation and chemical reactions

The deposits and particles themselves may grow due to direct vapor condensation onto their surfaces. These surfaces usually favor heterogeneous nucleation. Eskola *et al.* [34] correlated the vapor condensation rates as a function of several parameters including the Sherwood number, geometry dimensions, vapor diffusivity, partial pressure and temperatures involved. Other researchers (Zhan *et al.* [10–12] and Fry *et al.* [35] from the same research group) have focused on ash aerosol formation, condensation and deposition in coal combustion.

In addition, vapors may react with a particle or with deposit surface materials instead of just condensing, leading to the growth of different solid species. According to Mikkanen [36], the rate of these phenomena are controlled by a mixture of different involved factors like diffusion, chemistry kinetics, vapor concentration, condensation-reaction, and available surface.

These mechanisms may be expected in the furnace and in the beginning of the superheater area, since beyond these the flow temperature is sufficiently low that direct condensation into fume particles takes place.

## 2.4 Models for ash deposition

Methods of computational fluid dynamics (CFD) are attractive and powerful for solving the complex Navier-Stokes partial differential equations numerically. When used properly, these CFD approaches may predict adequately the effects of an increasing number of fluid-involving problems. Indeed they constitute a truly powerful asset for the design and operation of boilers of any type. Multiple different approaches utilize CFD solvers for boiler phenomena, including but not limited to fluid motion, turbulence, heat transfer, chemical reactions and combustion, transport of mass/particles, agglomeration, erosion, and pollutant formation.

Fouling and slagging are also the target of CFD modeling. Weber *et al.* [5] reviewed the state-of-the-art of these tools for ash deposits. They concluded that their results are still mostly qualitative, at their best. It was noticed that often numerical models lack of adequate accuracy standards for a proper determination of the fluid flow over heat exchange tubes or tube arrays. The meshes need to match specific resolution requirements, which are often overlooked, in order to predict the particle motion and the boundary layers effectively. It was also observed that most models do not execute a

transient study of the case, neglecting the importance of von Kármán vortex shedding and the Coanda effect, which combined lead to a swinging fashion in the motion of the flow over tube arrays; as pointed out by Ishigai *et al.* [37] and Zdravkovich [38].

Thus CFD approaches still present important limitations. The phenomena present in a boiler are very complex, requiring multidisciplinary knowledge and understanding to be properly tackled at once. In addition, Weber *et al.* [8, 39] show that the geometry of the tube banks require a particularly fine meshing, which as of today is still prohibitive at boiler-scale. Even with a narrow scope it may happen that a particular problem is still hard to handle, e.g. a chemical analysis should take into account numerous reactions among different phases of reactants, including phase changes.

Due to the aforementioned limitations, CFD approaches for fouling and slagging are typically addressed at two roughly different scales. Global, boiler-scale works aim to calculate fouling trends on the whole boiler or a considerable part of it. These models solve the flow patterns through the different heat exchangers. The macroscopic nature of this sort of models imposes the usage of coarse meshes (e.g., cell sizes of the order of 1 m can be typical). Due to the high complexity of the geometry in the heat exchanger areas, it may not be reasonable to generate a mesh fine enough to reproduce the actual tube geometry. Therefore, the geometry needs to be simplified somehow. These may be adequate, for example, to model the furnace as Vuthaluru and Vuthaluru [40] or to model the superheater plates as rectangular geometries, as in the studies of Leppänen *et al.* [41–45]. Figure 2.4 shows an example of one of these large-scale models.

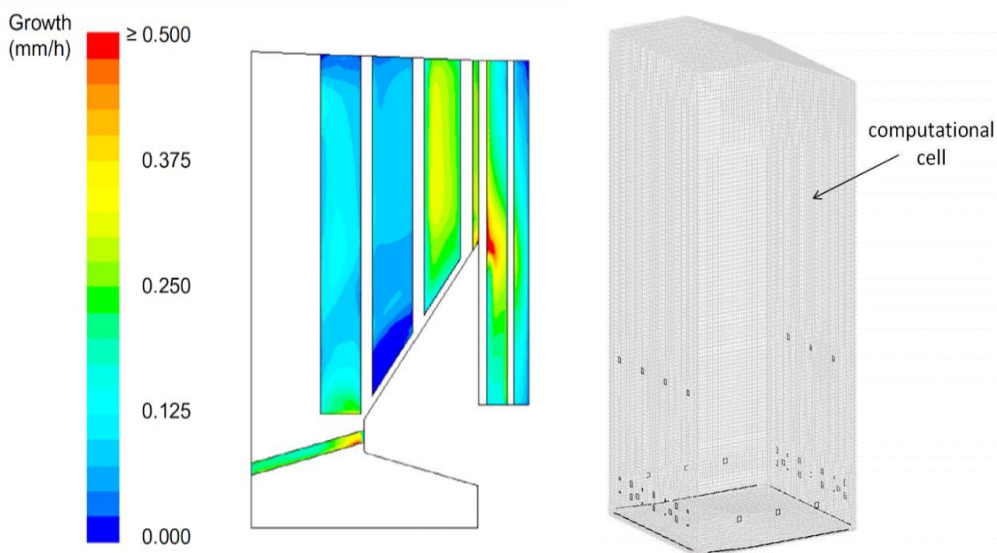


Figure 2.4: Examples of large-scale CFD models. Left: distribution of fume deposit growth rate on the superheaters of a KRB [41]. Right: Outline of the 3-dimensional grid [44] used to mesh the furnace in previous work [41]. Reproduced with permission.

Other researchers such as Wessel and Baxter [46] model the heat exchangers as porous media. In this latter approach, the source terms of the Navier-Stokes equations must be conveniently modified in those regions in order to account for the pressure drop, heat transfer, turbulence generation, and other necessary flow parameters. This is done when the flow crosses a zone where a heat exchanger (e.g., a superheater or boiler bank) is located but not represented in the mesh. In different investigations, such as in Jokiniemi *et al.* [47], one-dimensional approaches for the flue gas path through the boiler to calculate ash aerosol generation and deposition trends have been utilized with good results. The drawback of these models is that the flow might not be accurately predicted up to the detail required for the prediction of the deposition trends, and that the source terms also need to be modeled. Nonetheless, the domain may span back to the combustion stage, giving an appropriate context to particle and chemical species formation, concentration and properties.

Alternatively, other investigations model very specific regions of the boiler at a relatively medium or small scale, namely the corner of a furnace [48], the corner of a superheater plate [49], whole tube plates [50, 51], a deposition probe [30, 52, I, V], or even complete tube banks [53, II—IV, VI, VII]. These approaches typically use meshes with a much finer cell size (usually < 1 mm). The flow patterns, vortices and fluctuations may be predicted with this sort of modeling. However, the context of the domain within the boiler is somewhat lost. The input conditions to these models (pressure, velocity, turbulence intensity, temperature, ash particle concentration, among others) must be estimated or calculated outside the model. Also, the advantage of predicting the flow accurately entails a heavy penalty on computational costs when an unsteady solution is required. The present thesis aims to introduce one of these kind of approaches to model the ash deposition in tube arrays. Figure 2.5 shows two examples of these smaller-scale models.

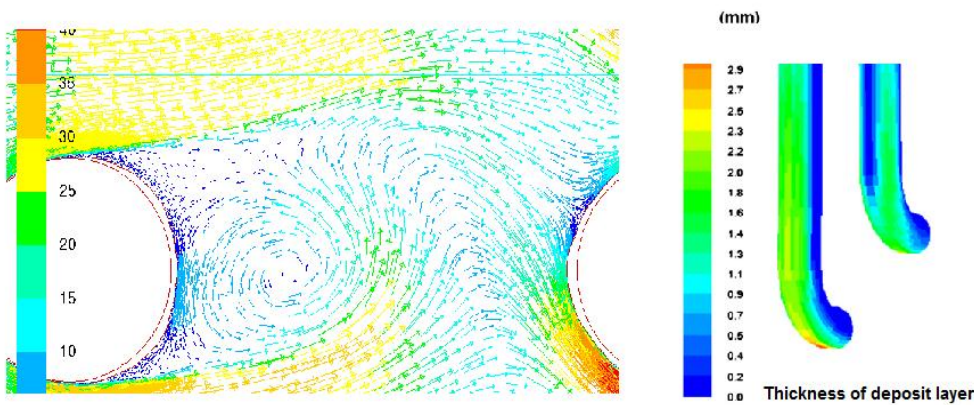


Figure 2.5: Examples of small-scale CFD deposition models. Left: deposit growth in unsteady flow simulation [II]. Right: Deposition model of the corner of a superheater plate [49]. Reproduced with permission.

## 2.5 This thesis: unsteady model for ash deposition

In tube banks, except when they are arranged in a platen geometry, the combination of von Kármán vortex streets and the Coanda effect leads to a periodically unsteady flow pattern with significant oscillations and swings, as already stated [37, 38]. See Figure 2.3 and Figure 2.5 (left). Oscillations may also occur past the trailing edge of tube plates, however, their effects on the flow fields near the tubes and on the deposition trends may be considered negligible since these oscillations are generated somewhat further downstream and their amplitude is typically much smaller than in tube banks [I].

When tubes are arranged in different manners, different patterns of flow are shed [37]. The patterns may favor the deposition of small-sized particles in the leeward part of the tubes due to vortices and swinging of the main flow direction. This justifies the need for a careful transient consideration of the problem.

The present thesis proposes a CFD model for prediction of fouling deposition in tube banks. The model may be enhanced with dynamic meshes which simulate the growth of a deposit layer. A periodical 2D row of four in-line tubes of a KRB boiler bank has been used as the target of the study in Papers [II, IV, VI]. The ash deposition rates were calculated and the growth of a solid cell zone wrapping the tubes was implemented in order to simulate the deposits formation. An example of a modeled fouled shape can be seen in Figure 2.6. The dynamic mesh model procedures and other main features of the model proposed in this work are presented in the following chapter in more detail. In Chapter 5 the model results are contrasted to experimental measurements of deposit thickness of a staggered tube array of a 100 kW pilot-scale combustor [III].

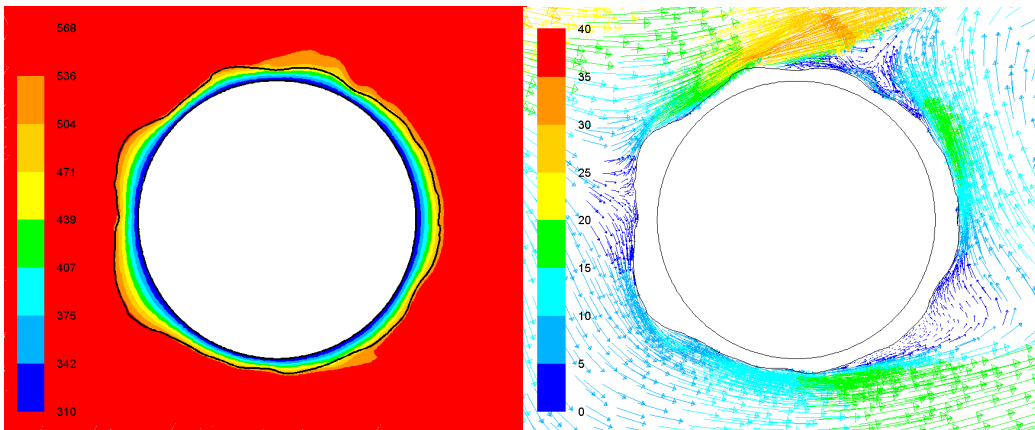


Figure 2.6: Left: Modeled deposit shape of a tube of a boiler bank ( $D = 5\text{cm}$ ) after 2 hours of growth, contours of temperature field in the deposit and in the flow around it [ $^{\circ}\text{C}$ ]. Almost all the temperature drops within the deposit, entailing a loss of heat transfer performance. Right: velocity field [ $\text{m/s}$ ] at the same location at the same moment as in the image on the left. Extracted from the simulations presented in [II].

## 3 Modeling unsteady flue gas and ash deposit growth

### 3.1 The solver and other main model guidelines

In this work, Ansys FLUENT enhanced with user-defined functions (UDF) has been used with a 2D single-precision unsteady SIMPLE solver, except for the validation (Chapter 5) where a double-precision solver was used.

Variable extrapolation for a quicker unsteady convergence is advised. In addition, it is suggested that the solver be added reasonable maximum and minimum temperature and pressure limits, for they would ease calculations and convergence. The limits to the temperature could be, e.g., 5°C above the upstream flue gas temperature (providing that not combustion or other heat sources occur) and 5°C below the coldest tube temperature. To limit the pressure, usually a window of  $\pm 500$  Pa off the pressure boundary condition should be more than enough for most cases. In cases with high flow velocities and tight transverse tube pitches this range may need to be expanded. Under-relaxation factors and other solver parameters that have not been mentioned here could be left as default.

The time-step can be chosen from a maximum allowed Courant number  $C$ :

$$C > \frac{u\Delta t}{\Delta x} \Rightarrow \Delta t < C \frac{\Delta x}{u} \quad (3.1)$$

Where  $\Delta x$  is the length of a cell and  $u$  is the fluid flow velocity. The model user must estimate the worst (minimum) value of the factor  $\Delta x/u$  which is highly case-dependent, varying especially with different kinds of geometry. The FLUENT manuals [54, 55] recommend that the Courant number be generally of the order of 1, and always below 10. Consequently, for these applications the time-step might need to be as fine as of the order of  $10^{-6}$  s in cases with high fluid velocities and fine meshes, entailing significant penalties in the computational cost of the model. Iterations per time-step should be allowed, at least, until residual stabilization.

Turbulence must be modeled, for it affects the trajectories of the finest fraction of particles. Even though in some specific cases (e.g., the lab-scale combustor of [III]) the upstream flow may be laminar or almost laminar, the banks of tubes generate turbulence along the flow path [38]. If large eddy simulation is not feasible, it is recommended to use the *SST*  $k-\omega$  model with standard input since a good near-deposit boundary layer (the deposits are modeled as walls) prediction is essential for the ash deposition.

### 3.2 Meshing guidelines

The surfaces prone to ash fouling must be wrapped with a thin layer of solid mesh cells simulating an initial deposit. This solid cell zone can be as thin as desired (if the user needs to simulate the ash deposits from clean surfaces then this initial surface shall be

very thin), but it must contain at least a whole double layer of triangular cells which will be expanded to simulate the growth of the deposit; since it cannot be created from zero once the model has started. The interface deposit-flue gas must consist of a double coupled wall (the original wall and the shadow, following the terminology of FLUENT).

Some CFD studies for ash deposition are concerned about guidelines on minimal numerical accuracy. Balakrishnan *et al.* [48] performed a grid-independency study of their CFD model, but, unfortunately, this is not the common practice as it is not always possible or reasonable. Beckmann *et al.* [30] confirmed that for a proper determination of the particle trajectories upon an obstacle (e.g., a tube), of the flow field, and of the boundary layers; a particularly fine meshing is needed. Weber *et al.* [8] addressed the needed mesh resolution required to achieve the grid independence of the results for ash deposition models, aiming to provide useful general meshing guidelines. They suggested that the height  $\Delta y_1$  of the cells immediately adjacent to the tube surfaces should be such that at least four cells should fit within the boundary layer for its proper determination. This requirement leads to the following correlation as a function of the tube Reynolds number and tube diameter  $D$ :

$$\Delta y_1 < \frac{0.324D}{4\sqrt{\text{Re}}} \quad (3.2)$$

On the other hand, it is advisable to take a length  $\Delta x_1$  of the cells adjacent to the tube coherently with  $\Delta y_1$  so as not to generate highly skewed elements. Since the cells must be triangular in this model (for the remeshing methods that will be explained later) and two rows of triangles fit within one triangle height, it is suggested in this work to take the  $\Delta y_1$  from the previous equation as the half of the height of a triangular cell of side  $\Delta x_1 = (4/\sqrt{3})\Delta y_1$ . As for the cells within the deposit, it is not so crucial if they are somewhat skewed. In Figure 3.1  $\Delta x_1$  and  $\Delta y_1$  have been sketched.

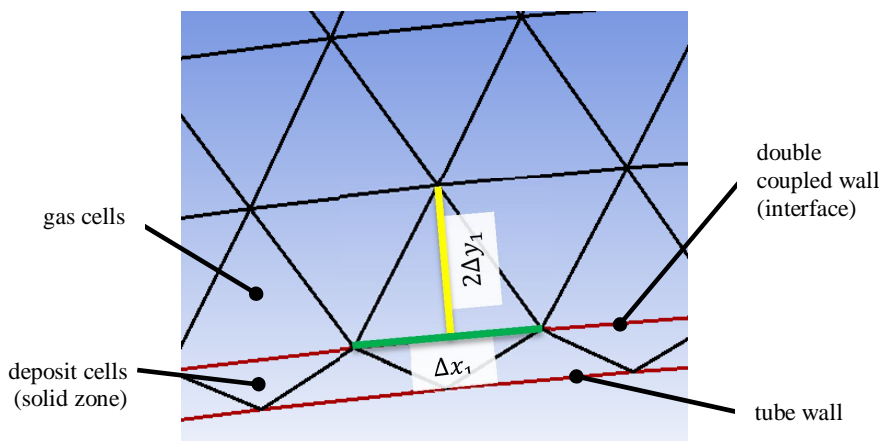


Figure 3.1: Detail of the first layers of cells in the near-wall regions of a tube of Paper [II].

Another study by the same authors [5] conducted a grid convergence analysis of particle-laden flows past a 2D cylinder and recommended to divide the tube circumference in at least 380 elements for a proper prediction of the trajectories of the particles with the smallest Stokes number. The impaction rates of these particles seems to be overestimated if the mesh is not fine enough. Altogether, the selected boundary layer cell size should be the minimum value between  $\pi D/380$  and the previously mentioned  $\Delta x_1$  in order to satisfy both accuracy criteria for the calculation of the fluid boundary layers and fine ash particle trajectories.

Maintaining the fine resolution required in the near-tube surface within the whole modeled domain would not be desirable in most cases for it would result into an unnecessarily very large number of meshed cells. Hence, the use of cell growth-controlling meshing size functions are encouraged. A suitable cell growth ratio (i.e., the size of a cell to the size of its adjacent cell which is closer to a deposition surface) should fall approximately between 1.1—1.3. This growth should, however, be limited to a maximum allowed cell size, recommended here to be of 50—100 times the smallest cell size. This is done not only to accurately solve the flow in the free-shear region flow, but also to maintain a fine discretization of the inlet boundary condition for an appropriate and less biased particle distribution within the domain.

### 3.3 Discrete particle tracking and impaction modeling

The particles are modeled by injecting periodically discrete parcels whose trajectories and dynamics are tracked independently. Each parcel represents a certain number of particles and the total quantity matches that of the ash accumulation at the face through which the parcel was released in the domain. Typically the particles are injected through the inlet, at the same temperature and velocities as the flow, although this may be modified if required in special cases. Paper [V] addresses this discrete model in more detail.

The user is advised to select carefully a suitable particle drag law. Details on the available drag laws and hints on their implementation are given in [V], including a newer customized form of a drag law suitable for small particles. The combined Cunningham-Morsi-Alexander [56, 57] drag law with the corrections proposed by Cunningham [56], Millikan [58], Davies [59] or Allen and Raabe [60] to the particle slip at high Knudsen numbers might be needed for better accuracy when particles of different sizes are being considered at the expense of some additional computational cost. The user must decide also how important the consideration for thermophoresis, Brownian motion and random turbulent eddies are, which affect particularly submicron particles.

When the trajectory tracking of a particle leads to an impaction onto a deposit, the particle may stick to it or rebound. Appendix A contains the equations and procedures of the adapted particle sticking—rebounding algorithm suggested in this work. The original work on particle rebound was done by van Beek [6], Konstandopoulos [7], Brach *et al.* [61] and Li *et al.* [62], used as well in other CFD models [52, 53]. Nonetheless, a different sticking/rebound approach could be used, if required.

FLUENT may be configured to call the UDF routine `DEFINE_DPM_EROSION` every time a particle parcel impacts a wall face. This routine can be used to implement the sticking—rebound algorithm detailed in the FLUENT UDF manual [63]. In the event of a rebound, the routine must modify the particle velocities appropriately (which are accessible with the macro `P_VEL(p)`). Otherwise, the parcel will remain stuck to the deposit. Consequently, it should be removed from the flue gas by using the macro `MARK_PARTICLE(p, P_FL_REMOVED)`. Then, its mass should be added to a variable responsible for storing the accumulated deposited mass on the impacted mesh face: `F_STORAGE_R(f, t, SV_DPMS_EROSION)` as it was suggested first by Tomeczek and Waclawiak [51]. Further details and examples of this code are available in the documentation of `DEFINE_DPM_EROSION` [63].

### 3.4 Deposit growth model

The solid cell zone constitutes the deposit which will grow according to the mass that has been collected in each face, determined by the aforementioned UDF routines. The CFD model shall compute the accumulated deposition, in mass units, individually for each one of the outer *faces* of the discretization of the deposit-gas interfaces. However, the mesh motion is achieved by moving its *nodes* where these faces are joined to each other.

Figure 3.2 shows that the movement of a given node is defined by a displacement vector  $\vec{r}$  (in red) which must be determined. For a better view, the angle between the two faces adjacent to the node has been exaggerated in the figure, but in the real simulation the faces are almost parallel since the deposit perimeter consists of a very large number of elements (e.g. 380 in [II] or 1520 in [IV,VI]).

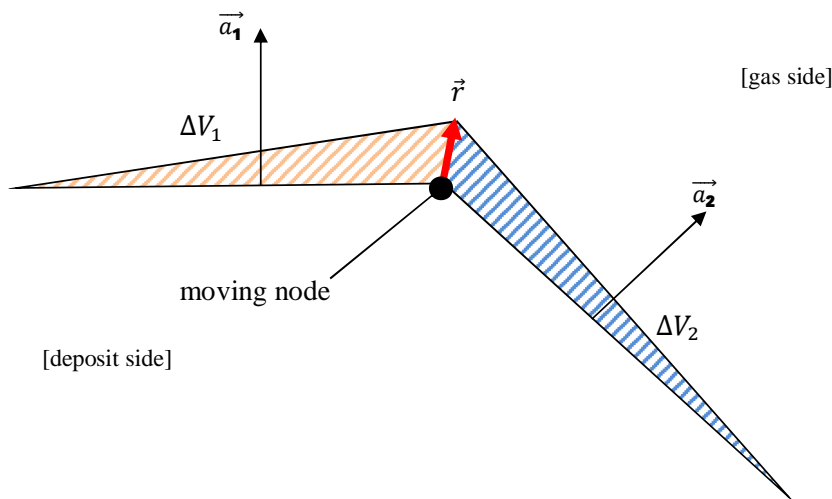


Figure 3.2: Scheme of the variables involved in the movement of a node which belongs to the outer interface of the deposit.

The vectors  $\vec{a}_1, \vec{a}_2$  represent the area vectors of each neighboring face 1 and 2, pointing outside of the deposit (towards the direction of the growth). The displacement  $\vec{r}$  will generate new deposit volumes in each face  $\Delta V_1$  –with orange crosshatching– and  $\Delta V_2$  –with blue–. In 2D, these represent actually volume per area of perpendicular tube length. The desired generated volume of each face would be:

$$\Delta V_i = \frac{1}{2} \frac{m_i}{\rho_p \varepsilon} \quad , \quad (3.3)$$

where  $m_i$  is the mass collected in the face  $i$ , and  $\rho_p \varepsilon$  is the deposit apparent density (the material density multiplied by the deposit solid fraction –i.e., one minus the porosity–). The factor  $\frac{1}{2}$  seen in the equation is introduced to share the effect of the deposited mass on the face between the displacements of the two nodes around it. Another interpretation of this factor comes from the fact that the displacement of one node is obtained by averaging the growth of the two adjacent faces.

With this notation, the volumes swept by a moving face are deduced from the area of a triangle of base  $|\vec{a}_i|$  and height  $[|\vec{r}| \cdot \cos(\widehat{\vec{r}, \vec{a}_i})]$ :

$$\Delta V_i = \frac{1}{2} |\vec{a}_i| \cdot [|\vec{r}| \cdot \cos(\widehat{\vec{r}, \vec{a}_i})] = \frac{1}{2} \vec{a}_i \cdot \vec{r} \quad . \quad (3.4)$$

The combination of the last two expressions yields a system of two linear equations for the determination of the two components of  $\vec{r}$ . However, the coefficient matrix of this system is composed by the vectors  $\vec{a}_i$  in rows, which are quasi-parallel (due to the fine meshing needed over the tube and deposit perimeters). Consequently, the numerical solving of this equation system is notably ill-conditioned and numerically unstable. Indeed, it proved itself not to be reliable at all to calculate the advance of the deposit front for the model proposed here (García Pérez *et al.* [64]).

To circumvent this problem, a more stable method is required. Here, a new approach is suggested where firstly the direction of the vector  $\vec{r}$  is assumed to be the average direction between  $\vec{a}_1$  and  $\vec{a}_2$ . Then, the magnitude of  $\vec{r}$  should be such that the total generated deposit  $\Delta V_1 + \Delta V_2$  matches the expected deposit growth in order to maintain the conservation of the deposited mass. With this procedure, the obtained growth does not match the mass collected in each surface separately, but the sum of them. Nevertheless, this solution does not entail significant error (especially with the fine meshing that is required), generates much smoother displacements, and is numerically stable. The final expression for this new approach to obtain the displacement results in:

$$\vec{r} = \frac{\vec{a}_1 + \vec{a}_2}{|\vec{a}_1 + \vec{a}_2|} \cdot \frac{m_1 + m_2}{|\vec{a}_1| + |\vec{a}_2|} \cdot \frac{1}{\rho_p \varepsilon} \quad . \quad (3.5)$$

The first term at the right hand side of this equation is the unitary vector in the desired direction. The second term is the average deposition density, in  $\text{kg}/\text{m}^2$ . The last term converts this deposition density to the actual displacement magnitude.

### 3.5 Setting up a dynamic mesh in Ansys FLUENT

The CFD grid is deformed by enabling a FLUENT capability which is called “dynamic mesh”. This dynamic mesh incorporates a series of routines to perform the motion of the deposit boundaries and the proper adaption and reallocation of the adjacent deforming cell threads. Details can be found in the user’s manual [54]. The enabling of a dynamic mesh is straight forward but the specific set-up needed for a coupled-wall movement is not clearly detailed in the manual and it might take an unnecessary long time to the user to figure it out. Hence, a brief guidance for the configuration of the moving threads will be outlined here. It is up to the user to fill in the input text fields appropriately according to the case being modeled.

After enabling the dynamic mesh panel (Figure 3.3 left), the user is able to click the “Create/Edit...” button to open the dialog window (Figure 3.3, right). In this dialog the user must declare the motion of the different threads involved. The motion of the cell threads (typically, the flue gas and the growing deposit cell zones) must be set as “Deforming”, meaning that they should adapt themselves automatically to the movement of their adjacent boundaries. The interior face threads (typically labeled as default-interior) must *not* be set or declared at all. Any boundaries that are known not to move (typically the domain boundary conditions) may be marked as “Stationary”.

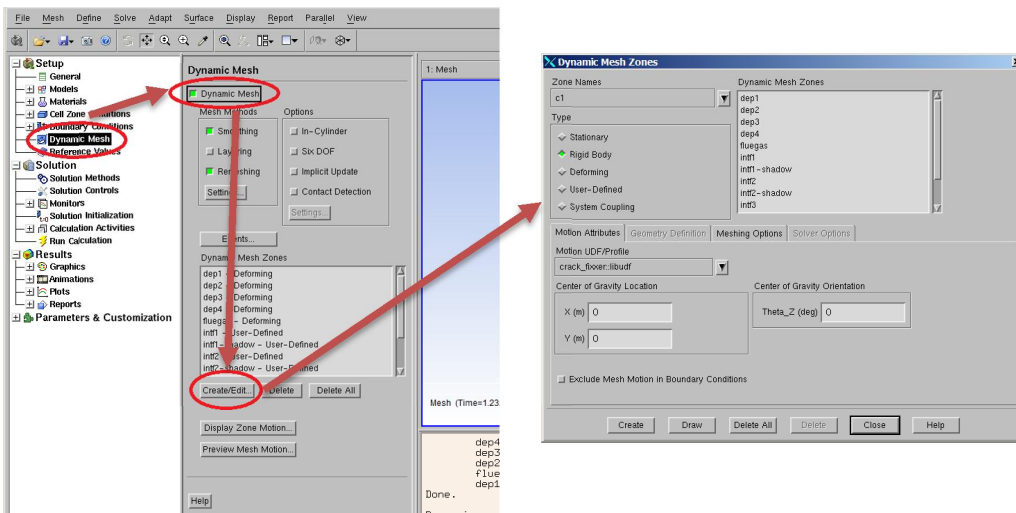


Figure 3.3: Left: Dynamic mesh panel. Right: Dynamic Mesh Zones dialog box (FLUENT 16.2). The appearance and available options may differ slightly with different versions of FLUENT.

The configuration of the interfaces (double coupled walls) is not evident. They must be set as “User-defined”. UDF routines `DEFINE_GRID_MOTION` are implemented to govern the movement of the outer deposit surface, deforming the deposit-gas interface. When coded and compiled, this UDF routine shall be available for selection after declaring the moving boundary as “User-defined”. Since the interfaces consist of a double coupled wall, it is advised to move first the gas-adjacent wall thread –by implementing Eq. 3.5 appropriately in the UDF–, and to force afterwards the adjacent deposit wall nodes to move to the new position of the already-moved gas-adjacent wall. For this purpose, it is useful to know that FLUENT moves the threads one by one in the exact order by which they have been declared (i.e., set as “User-defined” in the dialog of Figure 3.3, right).

There are several ways to code in the routine this movement-copying among walls. For instance, the coordinates (before and after moving) of each node of the interface may be stored in a globally accessible array when moving the gas-adjacent wall, so that afterwards the deposit-adjacent wall uses it to update itself.

While moving and deforming the mesh, smoothing and remeshing algorithms are usually required in the cell zones (those ones that were marked as “Deforming” in the Dynamic Mesh Zones dialog box) in order to avoid early crack generation, cell overlapping, negative cell formation and extremely skewed cells in the process [II]. These methods are essential for any deformation larger than the size of one cell. These tools are detailed in Appendix B with guidelines for understanding their relevant settings. These settings are introduced for the “Deforming” threads in the “Dynamic Mesh Zones” dialog box.

### 3.6 Model strategy

As stated, the typical cases of unsteady flow modeling require fine time-steps (usually,  $\Delta t < 0.1$  ms). It is not reasonable to simulate the flow over minutes or hours of fouling with such a fine time-step. This is why a certain strategy is required.

The strategy done in Papers [II, VI] and in Chapter 5 was to simulate the flow over a *sample* time of a limited duration (typically a few tens of flow oscillation periods) to estimate the deposition rates distributions (kg/s) on the deposition surfaces. These rates may be used to extrapolate the amount of deposit that would have accumulated after a longer period of time. This longer period of time is referred to as a *cycle*, and it is of the order of minutes. The duration of this cycle should be selected as a compromise between computational time (if it is too short, then too many cycles must be computed) and accuracy (very long cycles may lead to inaccurate predictions of time-varying deposit growth rates). The simulation of the flow and particulate is stopped after a sampling with the aim to calculate the deposition rates; then it is possible to activate the dynamic mesh and trigger a deposit growth with the button “Preview Mesh Motion” in the Dynamic Mesh panel (Figure 3.3) or with the TUI command `/solve/mesh-motion`.

A remark concerning the mesh deformation should be mentioned here. When a very fine mesh is used and the deposit advances are comparable to, or larger than the cell size (as

it happens in [VI]), it is desirable and sometimes necessary to divide the cycle deformation into several steps. That is,  $n$  movements are carried out, each one with magnitude  $|\vec{r}|/n$  instead of one unique move of magnitude  $|\vec{r}|$  (Eq. 3.5). This way the smoothing and remeshing will be executed  $n$  times within one cycle of deformation, allowing for smoother and much better mesh adaption and node re-allocation. Sometimes this approach is indispensable for stable calculations [VI].

The collected mass distributions of the relatively short samples may be too scattered (even if samples of a few hundred oscillation periods were taken) and they may need pretreatment prior to the mesh motion. The target of this is to convert the somewhat biased probed data to the more realistic collection distributions which would have been obtained if the flow had been actually simulated during several minutes. In addition, if this distribution is too scattered, the node displacements become highly unstable and erratic. A method called mass-spreading was elaborated, proposed, implemented and detailed in Papers [II, VI]. It was also used in Chapter 5 of this thesis.

This mass-spreading takes the mass collected by a face during a sample and spreads it among the neighboring faces. The spreading is done for each face of the deposition surfaces, repeatedly, over a selected number of times or iterations. This process is executed on the deposition distributions at the end of each sample. The model parameters (spreading weights, number of neighboring faces to spread among, and number of spreading iterations) may be chosen separately if several deposition surfaces are being modeled. It is recommended (if possible with a reasonable effort) to run a long initial sampling in order to have a less biased deposition distribution with which optimize and tune the mass-spreading parameters of the shorter samples [VI].

The simulations are brought to an end after a desired quantity of calculated cycles conclude [VI] or when the dynamic mesh fails and produces negative-volume cells [II]. This mesh failure is better detailed in Appendix B regarding the behavior of dynamic meshes.

Figure 3.4 is a sketch of the steps taken in this strategy. The mass-spreading algorithm and the node position update (Eq. 3.5) require a UDF code to access the neighboring faces of a given node and are thus difficult to parallelize, since each parallel computer node has access to a limited partition of the whole domain. That is, if the parallel partition borders cross any gas-deposit interface, the dynamic mesh will not be able to update it. Thus, it is recommended to simply run those steps in serial FLUENT. Fortunately these hard-to-parallelize steps represent a very minor share of the total computational costs of this model. Step 4 is usually the most computing-demanding stage. The duration of step 2 is highly case-dependent and is usually of the same order as that of step 4. The usage of Rosin-Rammler particle size distributions may increase the computational costs of the Lagrangian tracking of the discrete particle parcels to be even heavier than the flow solving (as it happened in the calculations of Chapter 5). The duration of the other steps should not be significant compared to those two.

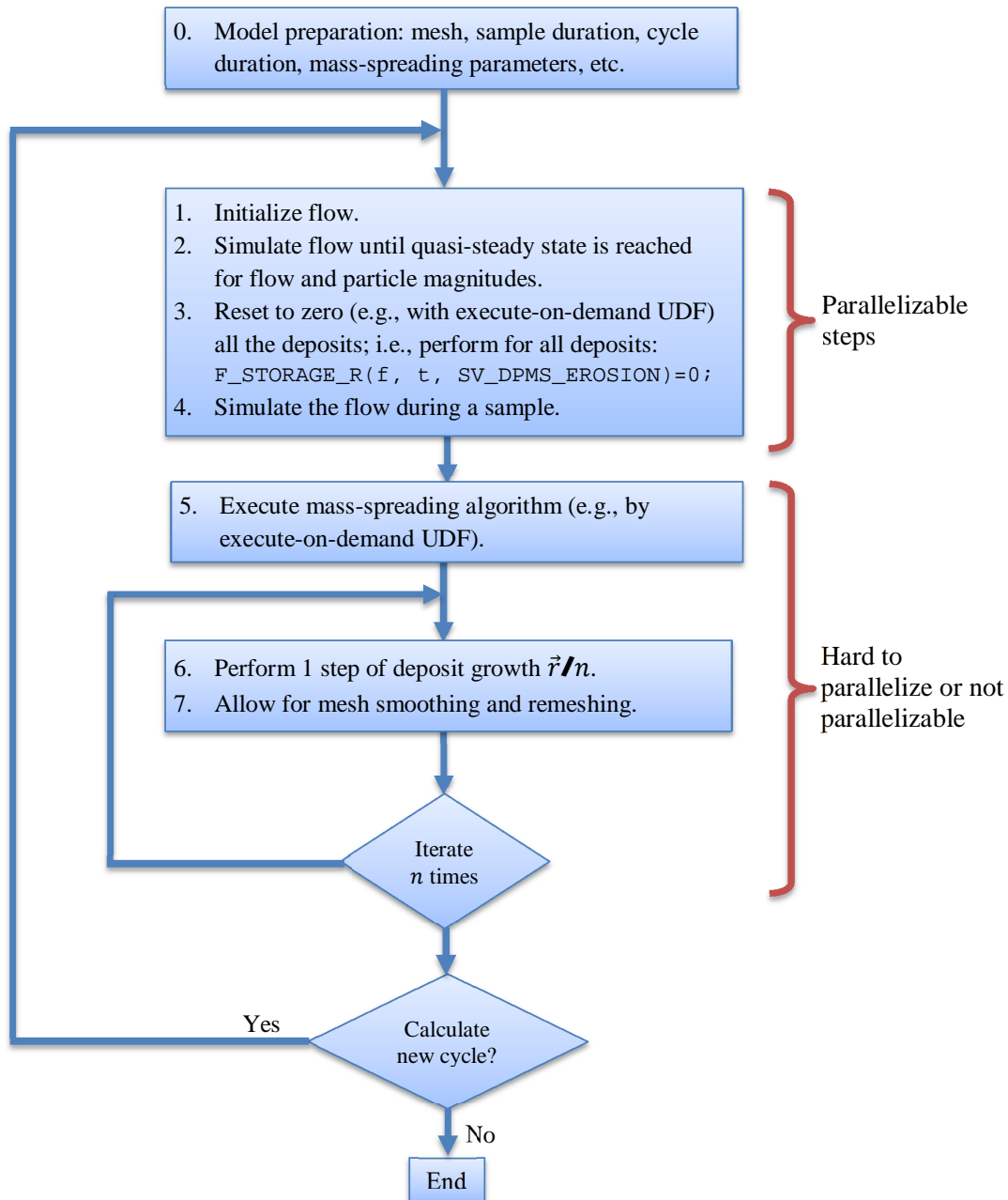


Figure 3.4: General outline of the model flow.



## 4 Findings and contributions

This section aims to list and to summarize the key findings of this work. Most of them can be also found in the conclusions of the attached papers with more detail.

In this work, every figure showing a 2D image of a tube or of a tube array is set so that the flow comes from left to right.

### 4.1 On the unsteadiness of the flow patterns

Paper [I] consisted of four CFD simulations of particle-laden flows past probes with different geometries. Field work by Tuomenoja *et al.* [66] was carried out with these probes (Figure 4.1) and their results were compared to the model calculations.

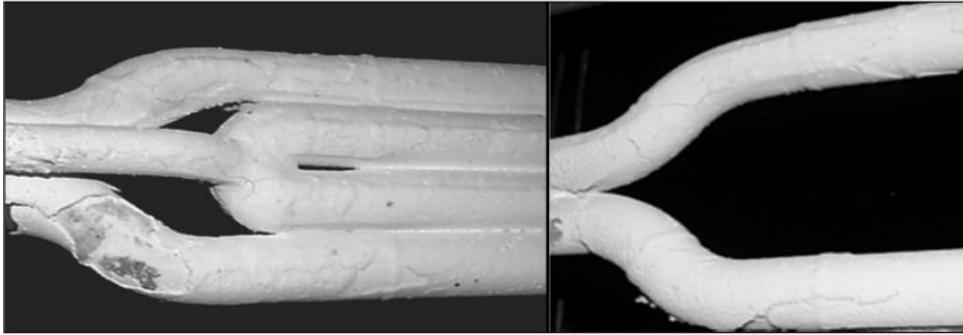


Figure 4.1: The two experimental probes used by Tuomenoja *et al.* [66] showing the deposit layer after fouling. Left: platen probe. Right: tubed probe.

Different boiler locations were simulated by adjusting the upstream gas conditions. A total of four simulations, the conditions of which are given in Table 4.1, were executed.

Table 4.1: Main simulation conditions of Paper [I].  $T_\infty$  and  $u_\infty$  stand, respectively, for the upstream flue gas temperature and velocity.

Simulation ID	1	2	3	4
Probe	Tubed	Tubed	Platen	Platen
Boiler location	Cavity, front wall	Vertical screen, left wall	Cavity, front wall	Vertical screen, left wall
$T_\infty$ [°C]	839	686	839	678
$u_\infty$ [m/s]	8.54	3.80	8.62	3.69

The flow patterns past the different geometries were analyzed. Transversally-periodic oscillations could be observed for all cases. For the tubed probe, these oscillations extended over two tube diameters in the lateral extent at the location of the first tube, and

before the flow reached the second tube. For the platen probes, these oscillations would occur about 3—4 tube diameters downstream of the trailing tube. The effect of these oscillations on the particle trajectories is shown in Figure 4.2 for the simulations 2 and 4:

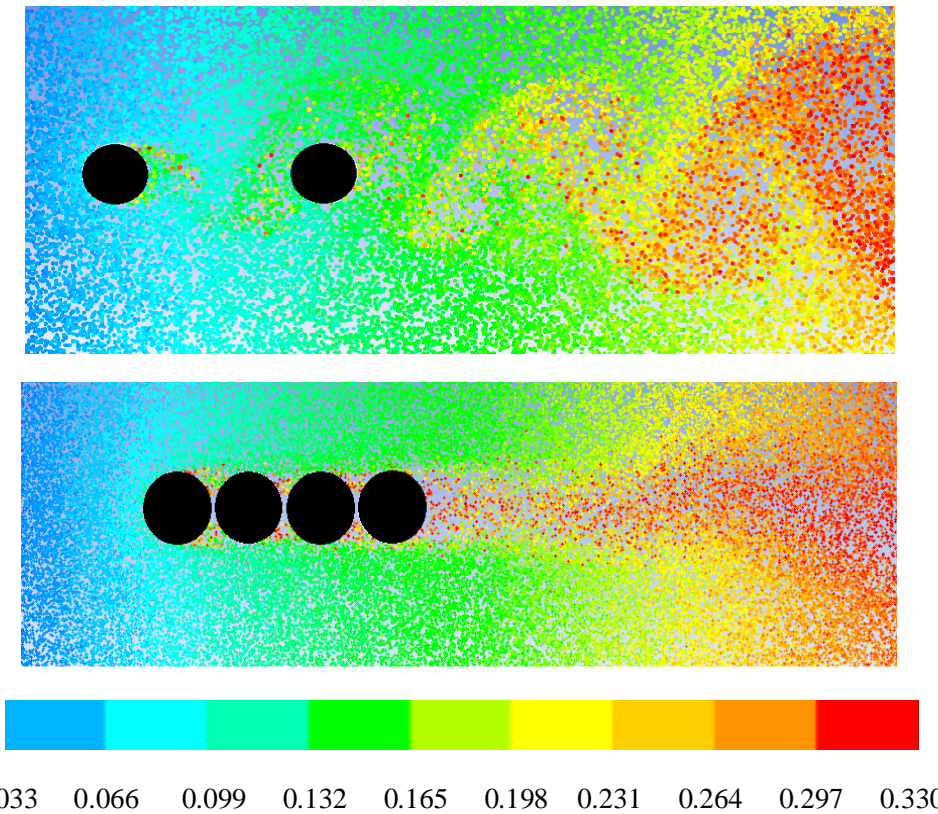


Figure 4.2: Fume particles colored by residence time, in seconds (i.e., the time that has elapsed since the particle was injected from the inlet of the domain) for a flow across the two probe geometries. Red particles are the oldest. Particles following an oscillating motion take more time to travel and are colored accordingly.

It can be noted from the tubed geometry of Figure 4.2 that some particles spend a certain time already in the space between the two tubes (colored in green surrounded by other blue particles) and some of them are even trapped in vortices (yellow and red). These flow patterns and particle trajectories may be captured only with unsteady simulations. On the other hand, the somewhat static wake of red colored old particles downstream the platen probe denotes that the flow field is such that the particles stay there for long time and do not travel significantly. This condition would favor the thermophoretical deposition of the smallest particles. These flow patterns might be simulated with steady-state approaches since the oscillations are located reasonably far downstream of the plate, at least for the largest fraction of particles, as done by Tomeczek and Waclawiak [51].

In the introduction to this thesis (Chapter 2), unsteady flow pattern and ash trajectories were shown in Figure 2.3. The steady-state particle trajectories of the aforementioned study by Tomeczek and Waclawiak [51] are highlighted in Figure 4.3. The agreement between these two studies is fairly good, as our unsteady calculations yielded a reasonably stationary flow for the platen geometry near the plate.

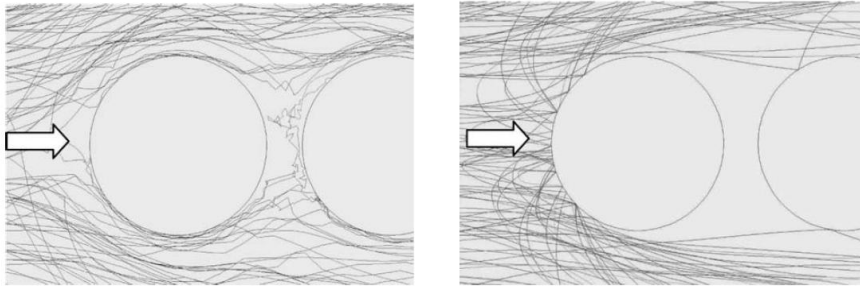


Figure 4.3: Steady-state simulated particle tracks over the first two tubes of a pulverized coal-fired boiler superheater [51]. Left:  $1\mu\text{m}$  particles. Right:  $33\mu\text{m}$  particles. Reproduced with permission.

## 4.2 On the flow patterns and particle trajectories past tube arrays

Paper [IV] was concerned with the flow patterns past tube banks. The periodical phenomena involving vortex generation, their growth, detachment, stretching and fading are described. Figure 4.4 sketches the flow patterns.

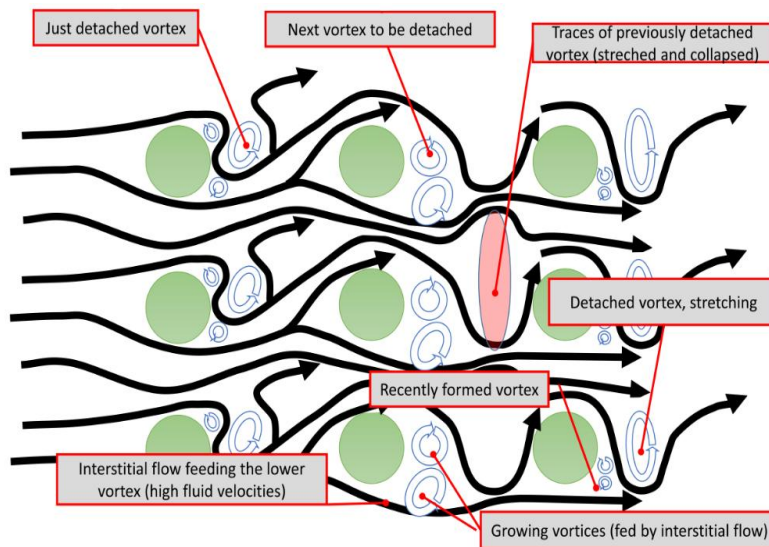


Figure 4.4: Unsteady flow patterns past a tube array (Section 3.2 and Figure 4 in [IV]).

These patterns lead to two key features which have direct consequences on the particle trajectories:

- Vortices: The wakes of the tubes generate low pressure and temperature vortices which oscillate and trap ash particles. These vortices grow in size until the interstitial flow (i.e., the main, bulk flow which actually travels through the bundle and is not part of the vortices) pushes and detaches them away. Fume particles of 0.7 and 3.62 microns were trapped in these formations [IV].
- Flow deviation: The interstitial flow deviates due to the Coanda effect as pointed out by Ishigai *et al.* [37] and Zdravkovich [38], following a swinging unsteady trajectory. The direction of the deviation oscillates, and hence, the flow points towards the following tube of the row while changing the direction, giving inertia and projecting particles towards the windward side of that tube. This is shown qualitatively in Figure 4.5. This effect occurs for the ISP [IV] which end up travelling in streams with high particle concentration, clusters, or fronts after rebounding off of the first tubes.

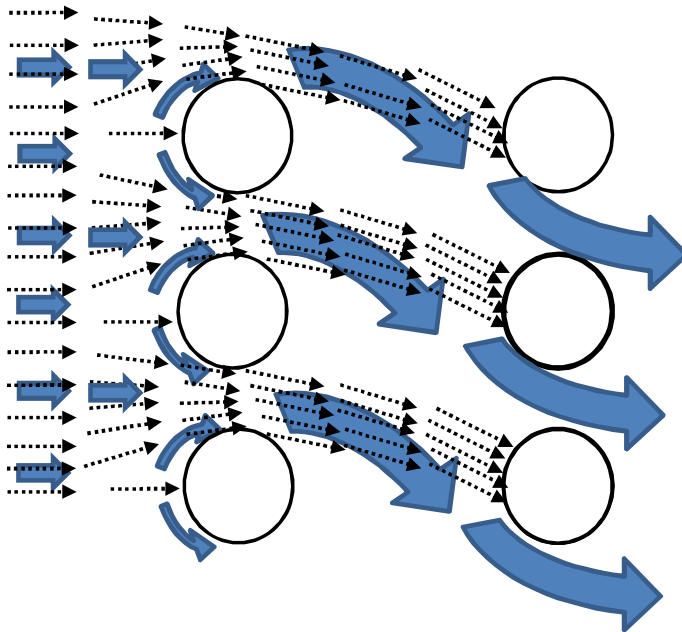


Figure 4.5: Sketch of the interstitial flow deviation (blue arrows) dragging particles (black dotted arrows) towards the following tubes.

The consequences of the aforementioned issues are highlighted in Figure 4.6, where the location and distribution of the particles within the flow are shown.

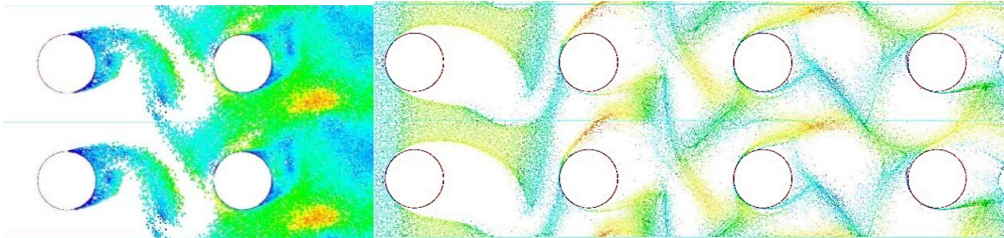


Figure 4.6: Instantaneous particle distributions past tube arrays (colored by particle velocity). Left: fume particles trapped in vortices. Right: ISP particles travelling in streams and fronts.

It was observed that the fume particles ( $0.7\text{--}3.62\ \mu\text{m}$ ) moved along with the flow and showed very similar inertial characteristics, up to a point that they could not be distinguished apart in videos. Thus, any observed differences in their depositions must be happening at microscopic scale in the tube boundary layers. On the other hand, the ISP ( $18.7\ \mu\text{m}$ ) had high inertia and they mainly did not follow the flow streams.

### 4.3 On particle deposition trends

As it has been approached by other authors [5, 30], the deposition trends may be explained by a combination of the particle arrival rate (which depends on the deposition mechanisms) and the particle stickiness. It has been observed in this work that these trends depend significantly on the particle size and on the tube location [IV]. As an example, the sticking efficiency variations over the tubes are shown in Figure 4.7. Other trends and deposition magnitudes are studied with more detail in Paper [IV].

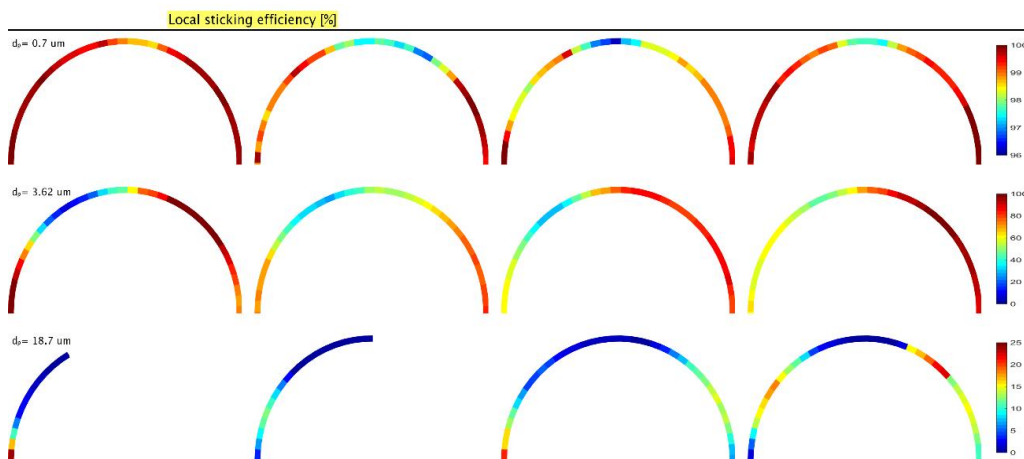


Figure 4.7: Local sticking efficiency for the four tubes of the row and for particles of different diameters. This is Figure 8 of [IV].

It was found that the particles with diameter of 3.62  $\mu\text{m}$  showed the smallest arrival rates, suggesting the existence of a critical particle diameter of minimal arrival rate. Unfortunately, this conclusion was deduced from the results obtained by using the default drag laws. This has to be interpreted with care since the newer customized drag laws proposed in Paper [V] would cause different conclusions, as it has been stated that the deposition rates of the very fine particles (such as the 0.7  $\mu\text{m}$  particles of [IV]) are usually misestimated by the default drag laws used in [IV]. It was thus necessary to repeat the simulations for the 0.7  $\mu\text{m}$  particles of Paper [IV] with the new drag law of Paper [V].

Table 4.2 summarizes the results of these new executions and compares them to the values already reported in [IV]; highlighting that the deposition rates had been overestimated. The total normalized impaction rates of the coarse fume particles (3.62  $\mu\text{m}$ ) was 5.87, therefore this value does not represent anymore the minimum. Consequently, the conclusion that those coarse fume particles were large enough not to be affected by thermophoresis, yet too fine to present inertial impaction, is no longer applicable.

Table 4.2: Normalized integrated quantity of impactions of 0.7  $\mu\text{m}$  particles [IV], comparing with and without the new drag law of [V]; and with and without the thermophoresis simulation enabled.

Tube	Old drag law, th. enabled [IV]	Old drag law, th. disabled [IV]	New drag law, th. enabled	New drag law, th. disabled
1	1.44	0.073	0.397	0.104
2	2.45	0.158	0.687	0.182
3	2.87	0.156	0.821	0.173
4	3.44	0.221	1.04	0.250
sum	10.3	0.608	2.95	0.709
relevance of thermoph.	94 %		76 %	

Unfortunately, the new drag law of Paper [V] was elaborated after the publication of Paper [IV]. Therefore this improvement could not be included in Paper [IV].

#### 4.3.1 Particle size and flow effects on thermophoresis

The propensity to thermophoresis has been addressed in this work [III, IV] as the quotient between the thermophoretical force  $F_{th}$  and the advective or inertial forces  $F_i$  of a particle:

$$\frac{F_{th}}{F_i} \sim \text{Re}_p^{-2} \frac{\rho_p}{\rho_{\text{fluid}}} \cdot \frac{d_p}{T} |\vec{\nabla} T| \quad (4.1)$$

This term is  $\mathcal{O}(d_p^{-1})$  since the particle Reynolds number depends linearly on the particle diameter. Consequently, the thermophoresis increases its significance for the particles with smaller diameters. This explains that thermophoresis was responsible for the 76% of the deposition of the submicron particles, whereas it represented only the 0.07% of the deposition of the ISP particles [IV].

This propensity can be observed as a field, highlighting which areas and flow patterns favor more thermophoresis-caused particle motions. The thermophoresis itself becomes weaker along the flow path because of the decrease of the temperature gradient magnitude [33, 67]; but the flow velocities become also smaller, entailing a more remarked decrease of the advective forces:  $F_{th}/F_i = \mathcal{O}(|u|^{-2})$ . Hence, the global significance of thermophoresis (Eq. 4.1) is expected to increase as shown in Figure 4.8.

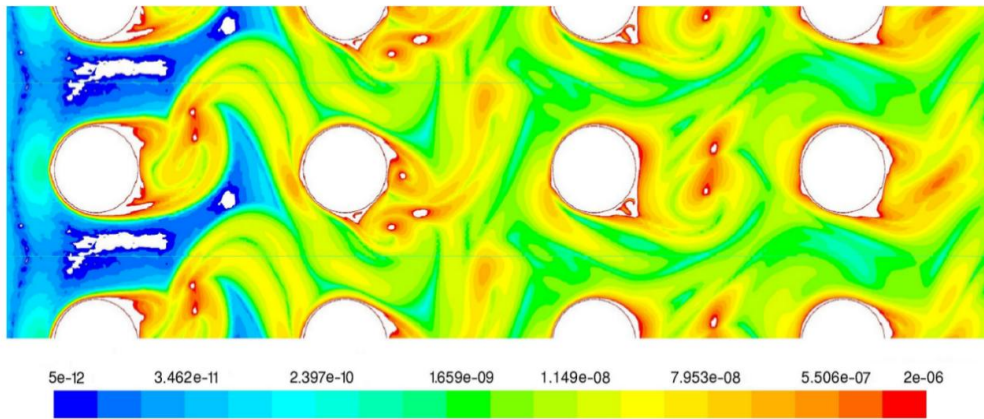


Figure 4.8: Field of thermophoresis propensity (right hand side of Eq. 4.1) based on a particle size of  $0.7 \mu\text{m}$ . This is Figure 11 in [IV]. The colormap is dimensionless, in logarithmic scale.

#### 4.3.2 Particle size effects on stickiness

An analysis of the energies and considerations taken in the stickiness approach used in this work, which is detailed in Appendix A, was used to address the propensity of a particle to rebound or stick as the quotient between the energy available for rebound and the necessary energy to create new surfaces upon possible particle detachment [IV]. It was concluded that particles with a diameter within the range  $3.62\text{--}18.7 \mu\text{m}$  showed a tendency to rebound which varied on their diameter as  $\mathcal{O}(d_p^{2.90})$ . The consequence is that smaller particles tend in general to stick more, just because of their mechanical behavior. This finding gives explanation to the results obtained ([IV] and Figure 4.7) and to the empirical findings of Zhan *et al.* [12, 35], where the fine fraction of ashes was found to be significantly more sticky than coarser particles.

### 4.4 On fume fouling of transversally-periodic four-tube bundles

The fouling growth model presented in Chapter 3 of this thesis has been tested on a periodic row of four in-line tubes of kraft recovery boilers. These simulations are detailed in Papers [II, VI]. The diameter of the tubes is  $D = 0.05 \text{ m}$ . The results are summarized below.

#### 4.4.1 Effect of the transverse tube spacing

Different geometries were tested with different values of the tube transverse pitch ratio  $s_T/D$  in [II], with a constant particle sticking efficiency approximation. The overall observed trend was that tighter tube spacing geometries showed higher fouling rates, as it can be seen in Figure 4.9.

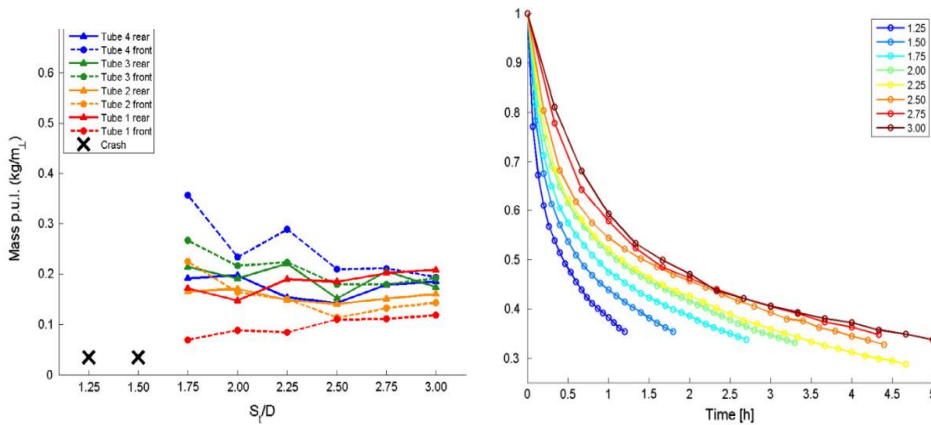


Figure 4.9: Left: collected mass in each tube side, per unit of tube length, after two hours of deposition (Figure 13 of [II]). Right: Evolution of the heat transfer performance (relative to the performance with clean tubes) for each different geometry factor  $s_T/D$  as a function of time (Figure 15 of [II]).

#### 4.4.2 Long-term unsteady fouling rates

Another general observed trend was the decrease of the fouling rates with the time, which was attributed to a decrease of the thermophoresis strength as the tubes become coated and absorb within themselves most of the temperature gradient.

This is highlighted in Figure 4.10, which shows the collected 4-minute deposition in a clean third tube (referred to as 1<sup>st</sup> cycle) versus the collected 4-minute deposition when the tube has been fouled after 100 minutes (referred to as last cycle).  $\delta$  is the angular coordinate to denote a location along the tube perimeter in such a way that  $\delta = 0$  corresponds to the tube lee and  $\delta = \pm \pi$  corresponds to the windward side. Similar figures for other tubes of the row can be observed in Paper [VI].

#### 4.4.3 Particle size effects on fouling

The final deposit shapes after 100 minutes of fouling are reported in Paper [VI] and shown in Figure 4.11.

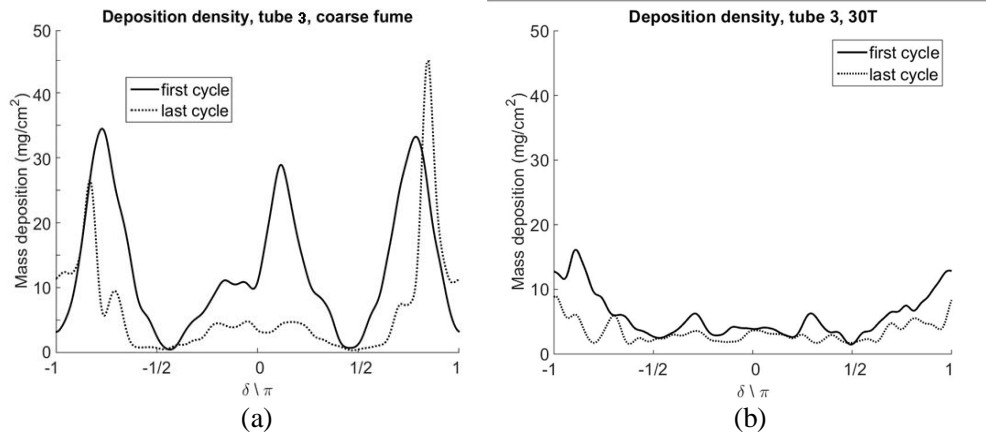


Figure 4.10: Deposition collected over the perimeter of the third tube [V], for: a) fine ( $d_p = 0.7 \mu\text{m}$ ) and b) coarse ( $d_p = 3.62 \mu\text{m}$ ) fume particles.

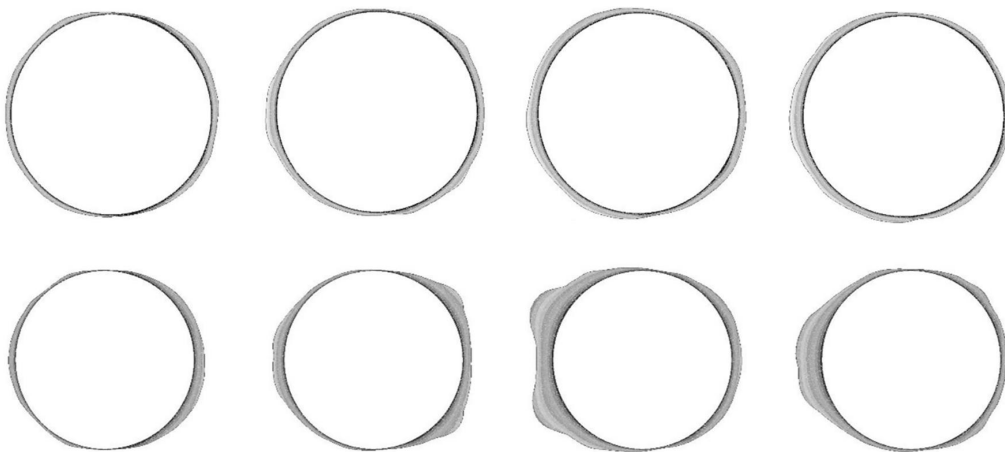


Figure 4.11: Fouling shapes of the four tubes after 100 minutes of fouling. Up: fine fume particles ( $d_p = 0.7 \mu\text{m}$ ). Bottom: coarse fume particles ( $d_p = 3.62 \mu\text{m}$ ). The longitudinal pitch between the tubes has been reduced in this figure for sake of space. Figures 10 and 11 of [VI].

Fine fume particles presented more round and uniform depositions, whereas coarser fume particles did not, showing particularly thick accumulations of material especially between the second and third tubes. As a consequence, the collected material in e.g. a single-tube probe might differ from what it would be observed on a multi-tube probe or on a tube bank. The deposition observed in one probe is often extrapolated to whole tube arrays [23] and, in light of these results, this practice must be done with care.

Due to the condensation and nucleation origin of fume particles, their average or mean size in KRB depends on the black liquor dry solids content, combustion conditions and temperature profile upstream of the locations where they have already reached their stable and definitive size [2, 18, 19, 68]. Consequently, these conditions which occur far upstream of the boiler bank may have a direct impact on the fouling trends of the coldest boiler heat exchange surfaces.

#### 4.4.4 Fouling model comparisons and model complexity

The conditions of the model in Paper [VI] were simulated again on simpler and earlier approaches of the model itself, to test the value of the relevant enhancements and to evaluate whether or not the increase in computational cost and model complexity is necessary. Three additional tests were made: A first test (a) of a coarse fume particle fouling growth modeled with a constant particle sticking efficiency of 61.07% (as given in [IV]), whose results were included in Paper [VI]; a second test or comparison (b) of fine fume particle fouling growth with the coarser meshes and time-step used in the model [II]; and a last test (c) with the fouling growth of a model which uses finer meshes, does not use the constant sticking efficiency, but which uses the old, default particle drag law used in this thesis before the elaboration of Paper [V].

- a) The target of this comparison is to test the validity of the constant particle sticking efficiency approach. For this case, the two different simulations showed similar result which can barely be distinguished one another. This is reflected in Figure 4.12 and Figure 4.13. Figure 4.12 should be compared to Figure 4.11 (bottom). Differences exist, but they are subtle and minor. Hence, for this case it may be stated that a constant-uniform sticking efficiency is good and reliable enough. Two remarks should be considered, though:
- The value of the constant sticking efficiency was obtained beforehand with the mechanistic sticking model itself. This means that if this simplification is to be considered, a reliable value of this efficiency must be obtained beforehand.
  - The constant sticking efficiency simplification may not be reliable in other cases, as empirical work has shown discrepancies between this approach and proper particle sticking considerations [30].

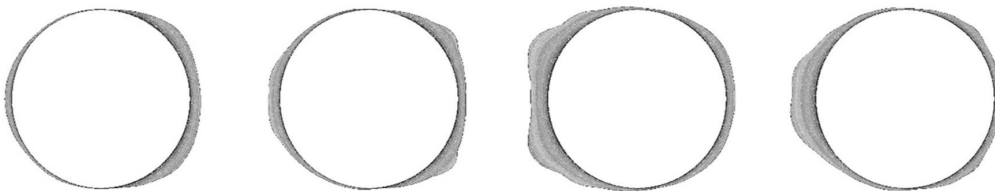


Figure 4.12: Tube bundle fouled with coarse fume, with a constant particle sticking efficiency. The deposits are very similar, but not identical, to the deposits of Figure 4.11 (bottom).

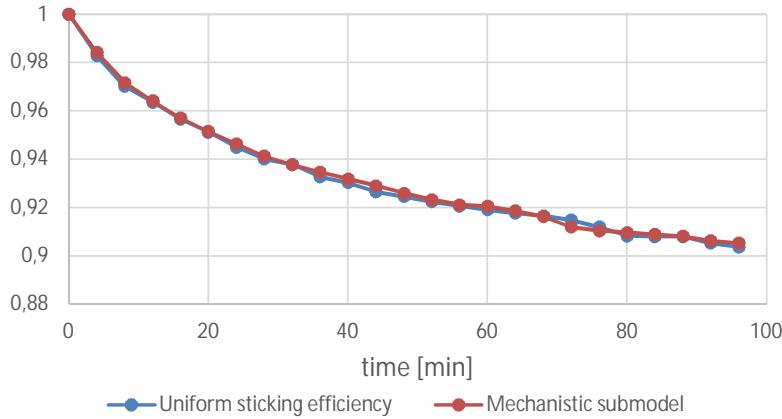


Figure 4.13: Evolution of the relative heat transfer performance for the coarse fume case of Paper [VI], with the uniform sticking efficiency versus the mechanistic submodel.

- b) The target of this comparison is to find out the effects of the grid resolution. Applying the model used in Paper [II] with a coarse mesh to the conditions simulated in Paper [VI] yielded significantly different results. When the coarser mesh was applied, the deposition rates seemed to be overestimated. The results can be observed in the deposit shapes (comparing Figure 4.14 to the top of Figure 4.11).



Figure 4.14: Fouled bundle with fine fume calculated with coarser meshes [II].

- c) The target of this comparison is to evaluate the effect of the drag laws used for very fine ash particles. For this purpose, the calculations of Paper [VI] were re-executed with the default drag law suggested by the FLUENT manuals, instead of using the newer drag law suggested in Paper [V]. This comparison differs from comparison (b) in that the drag law has been changed, but not the grid resolution. Whereas for the coarse fume particles no significant differences were observed (as it could be expected for the largest Cunningham corrections were about 1.12%), for the case of fine fume particles, the model with the old drag law overestimated the deposition as shown in Figure 4.15.



Figure 4.15: Final ash deposit shapes of fine fume particles after 100 minutes of fouling, with the drag law suggested by default in FLUENT manuals. These shapes should be compared to the shapes of Figure 4.11 (top). The underestimation of the particle drag has led to thicker and rounder deposits.

Altogether, the grid resolution and the drag laws are of a major importance. The computational cost of the improved model [VI] is about 25—30 times larger than the costs required to solve the primitive approach [II]. Nonetheless the differences, at least in accuracy and results, may justify the usage of finer numerical grids.

#### 4.5 On the particle-wise determination of the Cunningham effect

In Paper [V] a newer form of drag law which is generally valid for ash particles of any size is derived, proposed and tested. This customized drag law has, as an advantage, that it calculates the mean free path and the Cunningham correction factor independently for each particle at each time-step, instead of using a constant and uniform parameter.

Figure 4.16 highlights the erroneous trends and discontinuities that might arise in the behavior of the smaller particles if these effects are neglected. In the previous section, the comparison (c) showed the differences between these drag laws.

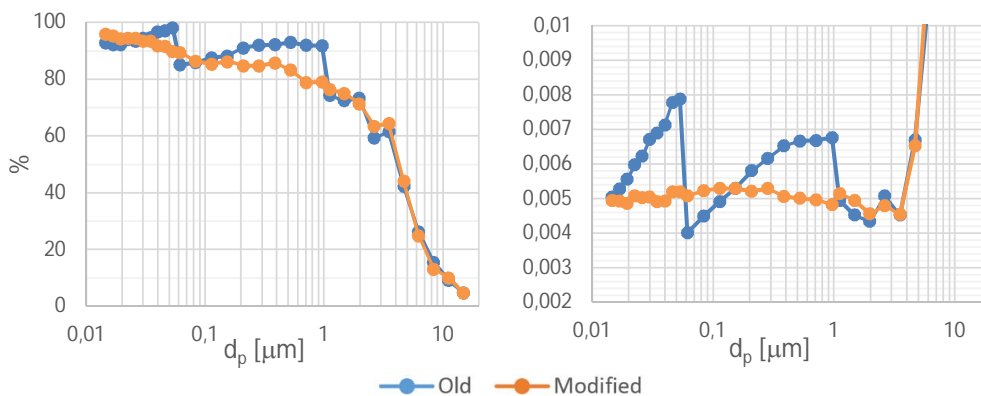


Figure 4.16: Particle sticking efficiency (left) and normalized tube arrival rates (right) to the probe simulated in Paper [V] for both drag law schemes, being the ‘Old’ the default one, and the ‘Modified’ the proposed in Paper [V] and used in Papers [VI, VII]. From Figure 4 of [V].

## 4.6 On the ash particle behavior on a staggered tube array

The methodologies of Paper [IV, V] was applied to an ash deposition model of the heat exchangers of the laboratory work carried out in Paper [III]. This led to the development of Paper [VII]. Two different geometries were tested (one with clean tubes and another geometry with fouled tubes), and the effect of the upstream gas velocity  $u_\infty$  was investigated.

Both the particle arrival and deposition rates were found to increase with  $u_\infty$ . All particles sizes below approximately 1—2 microns showed a uniform sticking behavior (arrival, sticking efficiency and deposition) which was dependent only on  $u_\infty$  and on the cleanliness of the tubes but not on the particle size. This is shown in Figure 4.17. Thermophoresis seemed to be more dependent on the gas velocity than in the temperature gradients, as suggested already by the thermophoresis propensity (Eq. 4.1). Higher deposition rates were observed with fouled tubes, possibly as a consequence of the variation of the ash particle trajectories and their impaction angles.

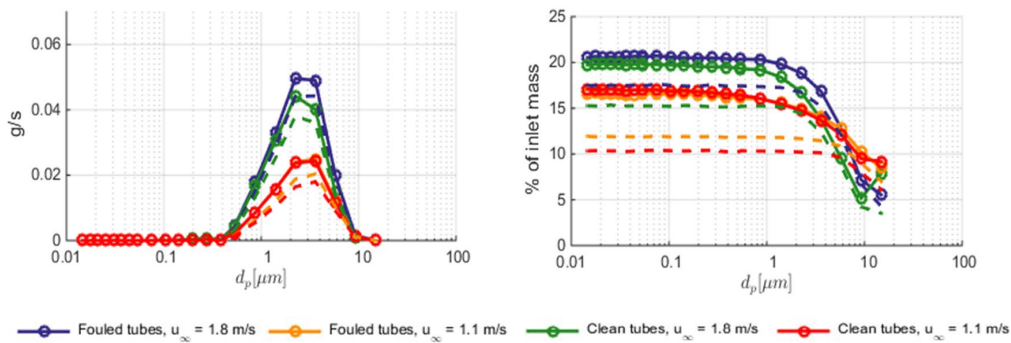


Figure 4.17: Total deposition rates (left) and normalized deposition rates (right) as a function of the particle diameter for the whole tube array. Figures 5 and 7 of [VII].



## 5 Validation

This chapter reports the usage of the deposit growth model simulating the 100-kW coal-fired combustor operation, for which deposit thickness measurements were performed [III]. Emphasis is placed on comparing the results with the measured data and on highlighting issues and challenges that may arise, rather than focusing on explaining fouling phenomena.

### 5.1 Introduction

#### 5.1.1 Case study

A pilot scale coal-fired combustor was run to test the combustion properties of different subbituminous coals. Two test campaigns were reported [III]. This work will focus on the first one of these test campaigns (referred to as *test 1* in [III]), where a subbituminous coal from Wyoming was fired with a target output power of approximately 27 kW. Further details of these experiments are properly defined in Paper [III] and here only the most relevant ones for the validation will be explained.

The fouling measurements focused on the heat exchangers of the convective section. Two water-cooled heat exchangers were located in series along the flue gas path. This work attempts to validate the measurements in the *second* (as it was referred to in [III]) heat exchanger, located right downstream of the first one. The tubes of the heat exchangers are submerged in a horizontal cavity with a square section of 15.2 cm side. The first heat exchanger of the study is disregarded, for the data on its fouling layer thickness is incomplete [III].

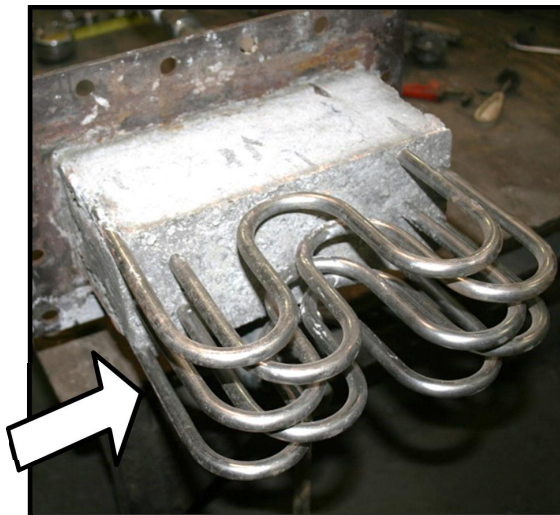


Figure 5.1: Picture of the heat exchanger. The white arrow indicates the direction of the flue gas.

The heat exchanger is composed by five staggered plates. Each one of these plates consists of one tube (1.27 cm outer diameter) which bends three times (four passes).

### 5.1.2 Previous considerations and uncertainties

The validation presented here, unfortunately, is subject to significant uncertainties:

- The working conditions of the laboratory measurements [III], which shall be used to validate the present work, were not constant but showed fluctuations typical of combustor operation, especially at the startup. The long operation of the combustor will be divided into fouling cycles of different durations. The durations of the cycles are selected in order to achieve a maximum deposit growth over the whole bundle of about 0.6 mm. This results in cycle durations of at least 30 minutes; comparable to or longer than most of the upstream flow magnitude fluctuations.
- The mesh is two-dimensional, accounting for the middle cross section of the heat exchanger. However, the tubes are relatively short (5.08 cm) and the toroidal tube bends at each pass (3.81 cm radius) may affect to some extent the flow in the cross section. In addition, the effects of the tube bends and their fouling on the evolution of the overall heat transfer coefficient (a magnitude which will be modeled and compared the measured data) is unknown a priori. Thus, the evolutions and comparison must be interpreted with care. Unfortunately, the computational costs of a three-dimensional deposit growth model are prohibitive here.
- Certain relevant properties of the materials were unknown, for instance, the flue gas composition or some properties of the ashes. These properties of ashes and deposits are of a major importance, up to a point that it would be possible to tune them to match any desired results.
- The empirical data [III] is inherently subject to certain measurement errors.
- The heat exchanger under study was located right downstream of another exchanger. Although the average longitudinal flow velocity was calculated at the inlet of our heat exchanger, the wavy periodical flow patterns in the transverse direction and the turbulence properties are unknown. The transverse component of the velocity field is not uniform over the whole inlet and its time dependence is not just sinusoidal. Consequently, the deposition predicted around the first tubes may be somewhat inaccurate.
- Similarly to the previous bullet point, this model and the measurements [III] are not exempt of other simplifications and approximations like, e.g., the combustor heat leakages through the refractory walls and the fraction of particles lost from the particle distribution measuring port to the target heat exchanger.

Owing to the aforementioned reasons, the results presented in this chapter must be regarded with care, as indicative or qualitative. Executing a proper, thorough and quantitative validation of the model proposed in this thesis would be very challenging and costly, as it would require more accurate empirical measurement equipment.

### 5.1.3 On notation

It is recalled that for all figures the flow comes from left to right. The angular coordinate  $\delta$  is used to denote a location within the perimeter of a tube, and it is referenced with respect to the tube direction according to Figure 5.2:

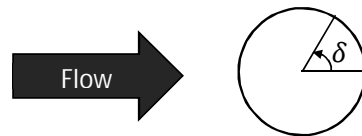


Figure 5.2: Referencing of the angular coordinate  $\delta$ .

To identify a certain tube within the bundle, a notation different from the one used in [III] is applied here. The heat exchanger consists of five plates which will be numbered in order from 1—5 in such a way that plate 1 is the leftmost plate from the flue gas point of view (i.e., the uppermost plate in the figures of this chapter). Within a plate, the tubes are numbered according to the flow path. Figure 5.3 sketches this notation with some examples.

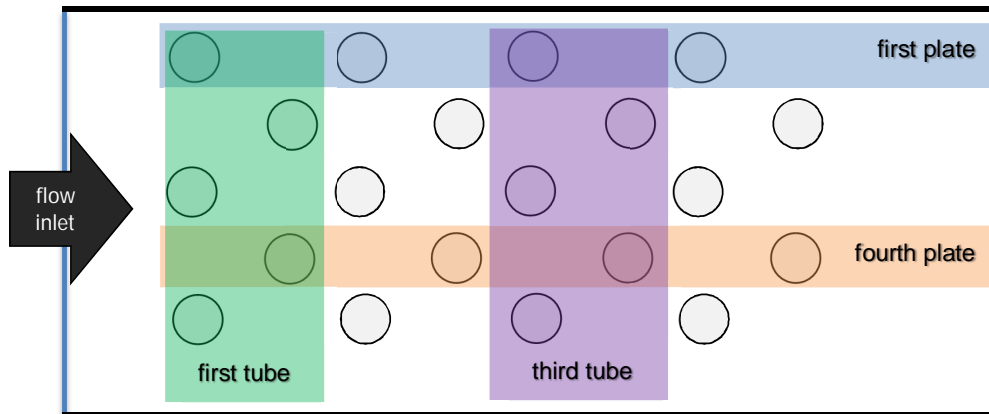


Figure 5.3: Notation used for individual plates and tubes. The tubes pitches and distances are not to scale.

## 5.2 The mesh and the solver

The two-dimensional mesh used is shown in Figure 5.4. The flow comes from left to right. The tubes are holes of  $D = 1.27$  cm outer diameter within a rectangular domain. The domain is 42.54 cm ( $33.5 \cdot D$ ) long in the flow (longitudinal) direction and 15.24 cm ( $12 \cdot D$ ) long in the transverse direction. Further details of the geometry and tube pitches are available in [III]. The velocity inlet boundary is located at  $5 \cdot D$  upstream of the center of the first three tubes of plates 1, 3 and 5. The pressure outlet boundary is set  $7 \cdot D$  downstream of the center of the last tubes (of the plates 2 and 4). The upper and lower boundaries are walls. The initial thickness of the deposits is 0.05 mm.

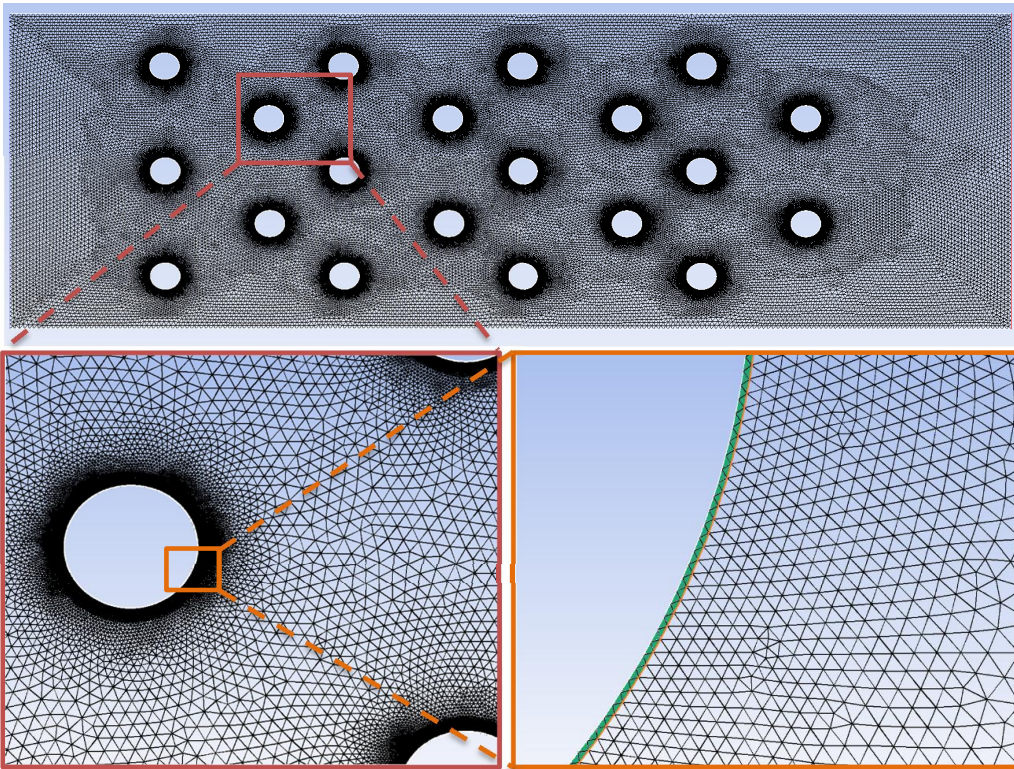


Figure 5.4: The mesh used in this model, with different levels of zooming. The initial deposit layer is identified in green in the bottom-right image.

The domain has been meshed following the guidelines presented in Section 3.2 of this thesis accounting for numerical accuracy criteria advocated by Weber *et al.* [8], which are satisfied with a total of 380 elements over the perimeter of each tube. The grid size function has a starting size of 0.152 mm and a maximum allowed size of 1.520 mm. The cell growth factor is 1.2. The initial mesh resulted into 367982 fluid cells (gas) and 15280 solid cells (initial deposits).

A first-order double-precision unsteady SIMPLE solver of Ansys FLUENT 16.2 is used, with extrapolation of unsteady variables within time-steps. The default solver's upwind schemes use second order differences in pressure, density, momentum and energy equations. The time-step of 0.1 ms satisfies Eq. 3.1 with  $C = 2$ . The effects of turbulence are simulated with a transition  $k-k_l-\omega$  model since the upstream Reynolds number is rather low (285), but turbulence is generated as the gas flows through the tube bundle [38]. The temperature of the solver is limited within the range  $[0, 700]$  °C and the pressure is limited within the range  $[70, 120]$  kPa.

### 5.3 Boundary conditions and injection of particles

#### 5.3.1 Upstream longitudinal gas velocity and temperature

The test lasted over 19h and 19 minutes of fouling for a total of 1159 minutes. Unfortunately, the conditions under which the test took place were subject to certain variations due to startup issues (at the beginning and towards 10h and 16 minutes of operation, when the unit was stopped overnight and the original raw coal was switched for its treated version), slightly different firing conditions (varying between 2.5—3.5 % of  $O_2$  excess), and also the typical unsteady fluctuations due to the nature of combustor operation.

Figure 5.5 shows the upstream gas velocity and temperature evolution for this work. The input of these parameters are modified at each cycle accordingly.

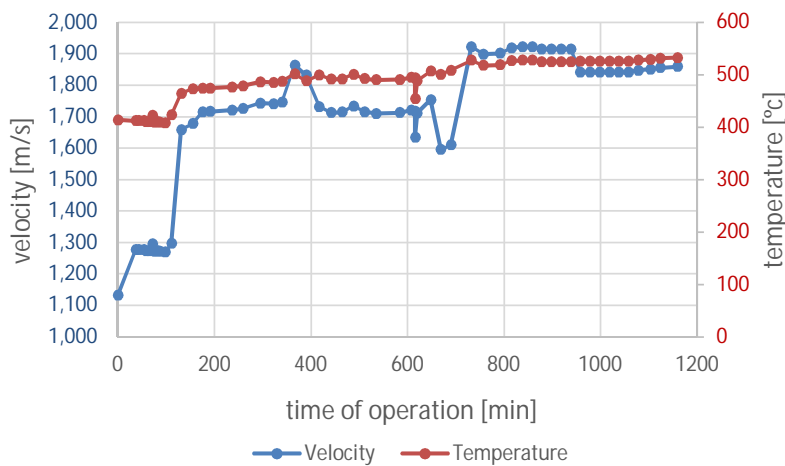


Figure 5.5: Measured temporal evolution of the upstream gas temperature and velocity [III].

Since the duration of the fouling cycles is somewhat long (the shortest one is 30 min) some fluctuations and variations are not captured. Each subsequent calculated fouling

cycle starts at a larger value of the time of operation (Figure 5.5). The values of the upstream velocity and temperature that have been input in this model for each different fouling cycle have been selected according to the value that Figure 5.5 is reflecting at the corresponding time of operation. These input values are detailed in Table 5.3 of Section 5.5.3.

### 5.3.2 Ash particles size distributions and discrete injections

In-situ particle ash size measurements were taken [III]. The diameter distribution of the ash particles is shown in Figure 5.6.

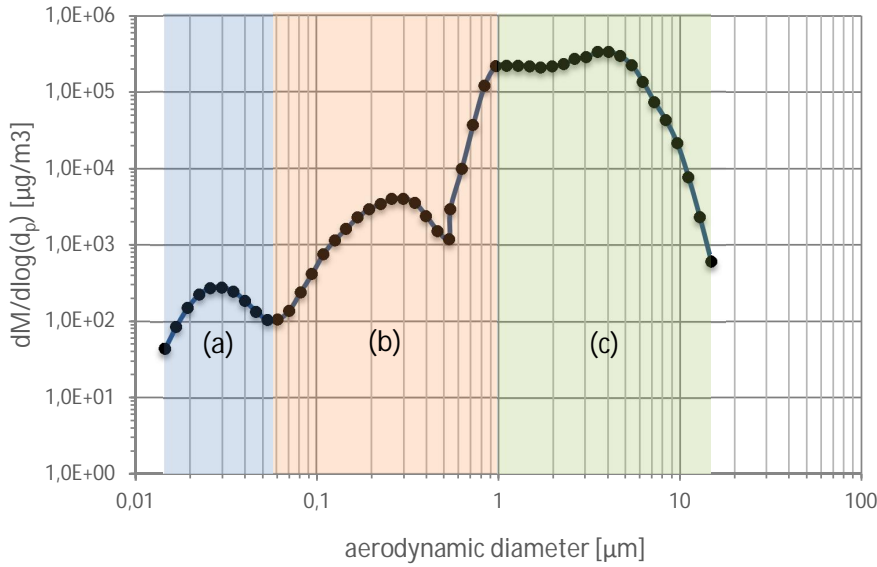


Figure 5.6: Ash particle size distribution for the model validation [III], with the three Rosin-Rammler regions used in this work highlighted.

A Rosin-Rammler distribution is typically used for differently-sized particle streams [54]. Within one of these distributions, the mass fraction  $Y_a(d_p)$  of particles greater than  $d_p$  is modeled as:

$$Y_a(d_p) = \exp \left[ - \left( \frac{d_p}{\bar{d}} \right)^c \right] \quad , \quad (5.1)$$

where the size constant  $\bar{d}$  and the size distribution parameter  $c$  must be determined to match appropriately the distribution. These parameters are computed in this model for the three Rosin-Rammler diameter ranges which have been highlighted in Figure 5.6.

Desirably, a Rosin-Rammler distribution would contain one absolute maximum and no local minima for a good distribution fit.

Good accuracy could be achieved by the use of multiple Rosin-Rammler distributions, although this would entail very heavy computational costs and memory usage. The tracking of a particle distribution is achieved by dividing the whole diameter range into a finite number of subranges of diameters, and injecting a representative particle parcel for each subrange, in each inlet face, at each time-step. Each parcel must be tracked separately, since its representative diameter and mass determine its dynamics, drag and trajectory within the gas.

Thus, the number of parcels to track may escalate remarkably if multiple distributions are implemented. Each one of the three Rosin-Rammler ranges has been divided in this work into 5 subranges of particle diameters, meaning that in each time-step a total of 1125 new parcels are released into the domain. Under stable flow oscillations, the computational domain for this model contains around 2.9 million particle parcels (for the second cycle, with an inlet velocity of 1.3 m/s) to be tracked periodically. The computational time of the particle tracking in this validation attempt was more than twice longer than the time required to solve the flow field (out of the approximately 16 seconds required to solve a whole time-step with 64 processors, only 5–6 seconds were needed to solve the flow). Altogether, the use of numerous particle size distributions may increase almost proportionally the computational costs up to prohibitive levels.

Therefore it was decided to use a total of three Rosin-Rammler distributions as a compromise between computational costs and accuracy at modeling the different particle sizes: range (a) with 0.0146–0.0533  $\mu\text{m}$  particles, range (b) with 0.0615–0.965  $\mu\text{m}$  particles, and range (c) with 1.114–14.86  $\mu\text{m}$  particles. These ranges were highlighted in Figure 5.6. It can be noted that the range (b) contains a local minimum which would worsen slightly its fit to a Rosin-Rammler curve. The reason to do this was so as to fix the separation between ranges (b) and (c) at exactly 1  $\mu\text{m}$  since a unique drag law can be implemented for each particle range: it is recommended [55] to use the Cunningham-Stokes drag law for particles with  $d_p < 1 \mu\text{m}$  –ranges (a) and (b)– and the spherical drag law for particles with  $d_p > 1 \mu\text{m}$  –range c)–. Consequently, some accuracy is sacrificed in range (b) for sake of accuracy in particle tracking and computational costs. Note that the improved drag law of Paper [V] was developed after this validation.

The Rosin-Rammler parameters have been calculated with the methods suggested in the FLUENT manual [54]. The detailed distribution data is summed up in Table 5.1. The mass flow rate of each particle stream  $\dot{m}$  is given per unit of upstream flue gas velocity  $u_\infty$ , since this velocity varies significantly in this work (within 1.1–1.7 m/s) and the mass flow rate of particles must be proportional, in order to match the target ash concentration in the gas. The resulting particle mass fractions curves  $Y_d(d_p)$  are plotted for each Rosin-Rammler range in Figure 5.7. The aforementioned inaccuracy of the distribution in range (b) due to its local minimum can be appreciated. Nonetheless, as it can be seen in Figure 5.7, it does not entail a significant error.

Table 5.1: Parameters of the Rosin-Rammler distributions and mass flow rate per unit of upstream gas velocity for each one of the three particle streams.

Range	$d_p$ [ $\mu\text{m}$ ]	$\bar{d}$ [ $\mu\text{m}$ ]	$c$	$\dot{m}/u_\infty$ [(mg/s) / ((m/s)· m $_\perp$ )]
(a)	0.0146—0.0533	0.03065	3.32	0.2650
(b)	0.0615—0.965	0.87331	3.19	63.436
(c)	1.114—14.86	3.3914	1.65	511.882

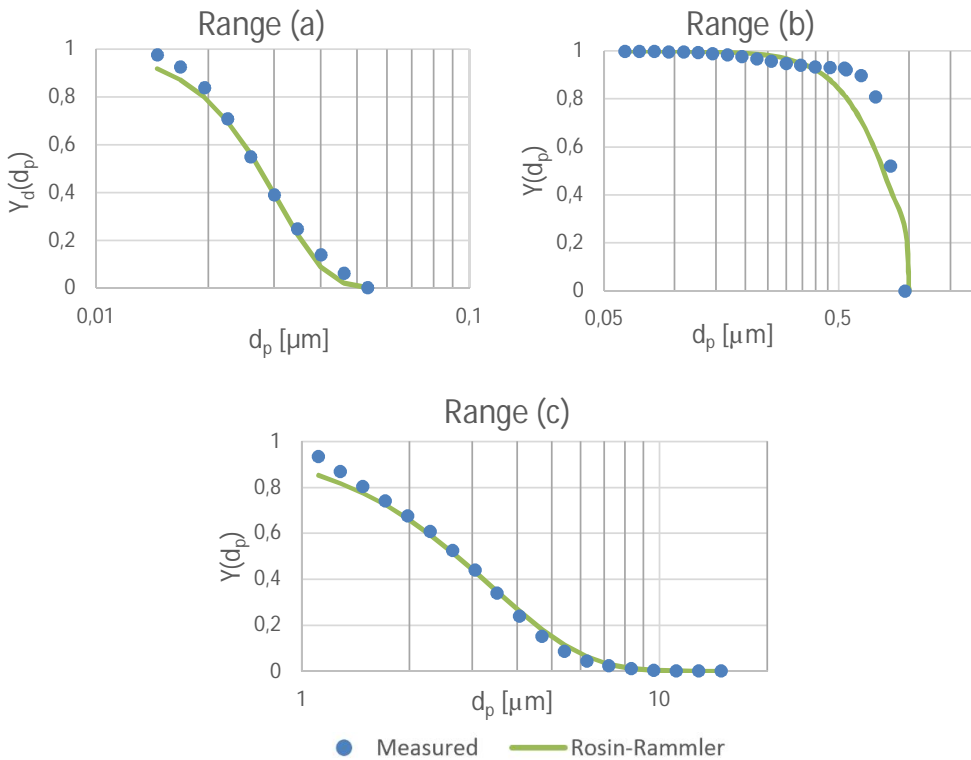


Figure 5.7: Measured particle mass fractions and modeled Rosin-Rammler distributions.

### 5.3.3 Other boundary conditions

The upper and lower domain boundaries have been set as walls with heat leakages of 720 W/m<sup>2</sup>. The outlet pressure is set at 89.3 kPa. The inlet turbulence intensity is 5 % and turbulent to molecular viscosity ratio is 10. The laminar kinetic energy at the inlet is set as 10<sup>-6</sup> J/kg. The temperature of the water-cooled tube walls is 29 °C.

The transverse component of the velocity has been modeled as a sine function in an attempt to simulate roughly the flow coming from a heat exchanger which was located

directly upstream. The amplitude of this variation is 1.8 m/s, which was the space-averaged amplitude of the transverse velocity at the outlet of the first heat exchanger (this value was obtained, although not explicitly reported, in the brief CFD model of [III]). The frequency of this oscillation is approximately 35 Hz, as it was measured by using this CFD model.

It must be noted that the oscillations of the flow as it leaves the upstream heat exchanger are more complex than the sine-like wave that has been assumed. Unfortunately, not much more can be done, since it is not possible to extend the domain further upstream before the first heat exchanger (due to the excessive calculation time that this would entail) to simulate better the incoming flow for this second heat exchanger.

## 5.4 Properties of materials

### 5.4.1 Properties of ashes and deposits

Unfortunately, relevant ash and deposit data could not be measured directly in the field work [III]. By mass-averaging the ash components, it is deduced that the ash density is  $3169 \text{ kg/m}^3$ . Similarly, the thermal conductivity for the particles was computed as  $11.26 \text{ W/(m}\cdot\text{°C)}$  and the specific heat as  $795.72 \text{ J/(kg}\cdot\text{°C)}$ .

The observed deposit thickness after about 19 hours of fouling [III] may be used to estimate the porous deposit density as follows: after conducting the first simulation sampling, it was observed that the deposition rates in the wind of the last tube of the second plate was  $0.164 \text{ g/(m}^2\text{s)}$ . Since it has been stated that the fouling trends typically decrease [41, 45, II, III, V] over time, the time-averaged deposition rates after the entire operation period should be somewhat smaller than this initial deposition rate. Thus, it may be assumed, based on the data of Figure 4.10, that the average deposition rate is around  $0.110 \text{ g/(m}^2\text{s)}$ , which is approximately 1.5 times smaller than the initial one. Furthermore, the calculated evolution of the heat transfer rate, seen in Figure 5 of Paper [III], does not vary appreciably after 15 hours of operation, suggesting that insignificant deposit growth occurs beyond this time. Finally, the final observed deposit thickness is 7.9 mm for that tube and plate [III]. Having concluded altogether that mass depositing at an average rate of  $0.110 \text{ g/(m}^2\text{s)}$  during 15 hours yields a final thickness of 7.9 mm, the resulting deposit bulk density is  $749.0 \text{ kg/m}^3$ . The solid fraction is thus 0.236, within range of typical fresh deposit porosities according to Baxter [1] and Ots [69].

The thermal conductivity of the deposits is a key parameter of the model and, unfortunately, it was not directly measured [III]. Ots [69] measured the thermal conductivity of deposit ash samples as a function of the porosity (or solid fraction). The analyzed coal ash had 31.45%  $\text{SiO}_2$ , 37.18%  $\text{CaO}$ , 6.6%  $\text{Al}_2\text{O}_3$ , 8.03%  $\text{SO}_3$ , 3.15%  $\text{MgO}$  and 8.47%  $\text{FeO}$  [69] in mass. These fractions coincide with the analysis of the ash which is being modeled here into an aggregated value of 79%. Consequently, the thermal conductivity could be assumed to be of the order of the values reported by Ots, which

correlated approximately to  $k[\text{W}/(\text{m}^\circ\text{C})] \approx 0.122 + 1.17\varepsilon$ , where  $\varepsilon$  is the deposit solid fraction.  $\varepsilon$  was estimated as 0.236, thus  $k \approx 0.398 \text{ W}/(\text{m}^\circ\text{C})$ .

The deposit conductivity and porous density are key parameters that determine the heat transfer performance. Since they were not directly measured in [III], but estimated and approximated by indirect and qualitative means, the results obtained here must be interpreted with some caution.

#### 5.4.2 Gas properties

The flue gas is treated as an ideal gas with the properties of combustion gases at the temperature and pressure of the combustor. Vakkilainen [70] suggests that appropriate values are: a specific heat of  $c_p = 1239.3 \text{ J}/(\text{kg}\cdot^\circ\text{C})$ , a thermal conductivity of  $0.0506 \text{ W}/(\text{m}\cdot^\circ\text{C})$ , a dynamic viscosity of  $3.114 \cdot 10^{-5} \text{ kg}/(\text{m}^2\cdot\text{s})$ , and a molecular weight of  $28.38 \text{ g}/\text{mol}$ . These properties are assumed not to vary during the simulations.

#### 5.4.3 Sticking model properties

Coal ash is composed of multiple different substances, making it challenging to determine adequately a set of the relevant properties regarding particle impaction. Silicon dioxide had the largest share in the ash analysis [III], and thus its properties will be used. An exception is made for the density, for which the average particle density value has been chosen. From an online material database [71] it was extracted that the Young modulus is  $E = 70 \text{ GPa}$ , that the Poisson's ratio is  $\nu = 0.17$ , and that the Vickers indentation hardness is  $H_v = 17 \text{ GPa}$  (the resulting uniaxial yield stress is  $Y = 5.67 \text{ GPa}$ , according to Eq. A.1 in Appendix A). According to Miskiewicz *et al.*, the surface energy for  $\text{SiO}_2$  is  $\gamma = 5.18 \cdot 10^{-2} \text{ J}/\text{m}^2$  [72], resulting in a particle adhesion work of  $\Gamma = 0.1036 \text{ J}/\text{m}^2$  (Table A.1).

With these mechanical properties, the resulting limit velocity for plastic deformation is  $71 \text{ m}/\text{s}$  (Eq. A.7), which means that no particle will experience any plastic deformation at all. The selected deposit friction coefficient is 0.5, therefore the resulting critical incidence angle is  $\theta_{cr} = 72.22^\circ = 1.26 \text{ rad}$  (Eq. A.2).

Further explanations and clarifications on these properties and magnitudes, and on their relevance on the sticking/rebound of an impacting particle, are properly detailed in Appendix A.

### 5.5 Fouling model characterization

#### 5.5.1 Dynamic mesh parameters

The selected local-face remeshing thresholds for the dynamic mesh model are summed up in Table 5.2 (further details are in Appendix B, Section B.2.2).

Table 5.2: Local-face remeshing thresholds.

Threshold	Deposit cells	Flue gas cells
Minimum cell size	0.163 mm	0.200
Maximum cell size	0.325 mm	1000
Target cell skewness	0.4	0.5

The spring constant factor is 0, as advised in this work (Papers [II, VI], and Section B.2.1). The deposit growth of every cycle was divided into a total of  $n = 8$  steps, as sketched in Figure 3.4 and explained in Section B.3. These eight divisions were found sufficient to maintain stable growths and a proper remeshing performance.

### 5.5.2 Sample duration

When quasi-steady flow conditions are reached, the observed flow oscillations over the heat exchanger are not exactly periodical, but they vary slightly in amplitude as shown in Figure 5.8.

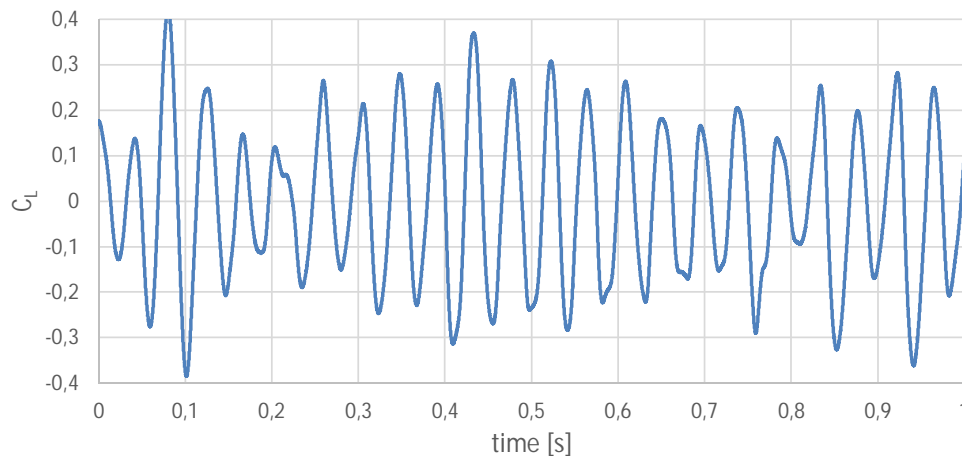


Figure 5.8: Quasi steady-state temporal evolution of the sum of the lift coefficients of the trailing tubes, with the conditions of the first cycle (clean tubes,  $u_\infty = 1.10$  m/s and  $T_\infty = 414$  °C).

Consequently, a long duration needs to be chosen in an attempt to obtain a representative sample. Forty oscillations (eighty sign changes of  $C_L^*$ ) have been selected in this work, making a total sample duration of 0.869 s.

According to Ahlborn *et al.* [73] and Williamson and Brown [74], with the simulation of subsequent cycles the unsteady flow swings are expected to oscillate even faster as the upstream fluid velocity increases, due to the relationship between the Strouhal and

Reynolds numbers. However, the sample duration is kept constant in order to be on the safe side, since it would be spanning over more flow oscillations.

### 5.5.3 Time-dependent inlet conditions

The duration of the cycles is varied between 30 and 40 minutes so as to maintain the largest deposit growth between 0.6 mm and 0.75 mm. Consequently, the duration of a cycle can only be estimated after the previous sampling is calculated. For instance, given the maximum deposition rates collected during the first sample (0.289 g/m<sup>2</sup>s for the first tube of the second plate) and the deposit bulk density, by fixing the cycle length to 30 min, the expected peak growth in that cycle is 0.6949 mm.

The simulation was stopped after the seventeenth cycle since the observed deposit shapes were already significantly larger than the measured values reported in Paper [III]. The direct consequence of this issue is that the deposit porosity had been overestimated. The total simulation time summed up to 550 minutes. The fluid inlet velocity and temperature were adapted individually for each cycle according to the measured data (Figure 5.5). The input values and cycle durations are shown in Table 5.3.

Table 5.3: Summary of input inlet conditions over the different cycles:

cycle #	duration [min]	starting fouling time [min]	$u_{\infty}$ [m/s]	$T_{\infty}$ [°C]
1	30	0	1.10	414
2	30	30	1.30	414
3	40	60	1.30	410
4	40	100	1.30	408
5	30	140	1.67	469
6	30	170	1.71	474
7	30	200	1.71	475
8	30	230	1.72	477
9	30	260	1.72	477
10	30	290	1.74	486
11	30	320	1.74	486
12	30	350	1.74	486
13	30	380	1.85	494
14	30	410	1.80	492
15	30	440	1.71	491
16	40	470	1.71	492
17	40	510	1.71	492
18	—	550	—	—

### 5.5.4 Mass spreading parameters

An optimization of the smoothing parameters was not carried out since, fortunately, the usage of multiple particle size Rosin-Rammler distributions led to much smoother deposition distributions than the results obtained in the simulations of [II, VI]. Therefore,

not much spreading was necessary and it was possible to obtain reasonably good distributions by visual inspection as it had been carried out in Paper [II].

For all tubes, the mass of a given face was spread among itself and the 12 neighboring faces (6 to each side), with a spreading factor of  $p = 4.0$  (the parameter  $p$  in Figure 4 and Eq. 9 of Paper [VI]) and twenty smoothing iterations.

Figure 5.9 highlights the mass distribution (raw and treated) for two arbitrarily selected tubes of the bundle after the sampling of the fourth fouling cycle. It can be noted how the raw distribution was not much scattered already, proving that the selected sample length is sufficient. It can also be noted how for the tube of the fifth plate the distribution is not symmetrical, for that plate is embedded in the refractory fluid boundary layer (the bottom boundary of Figure 5.4).

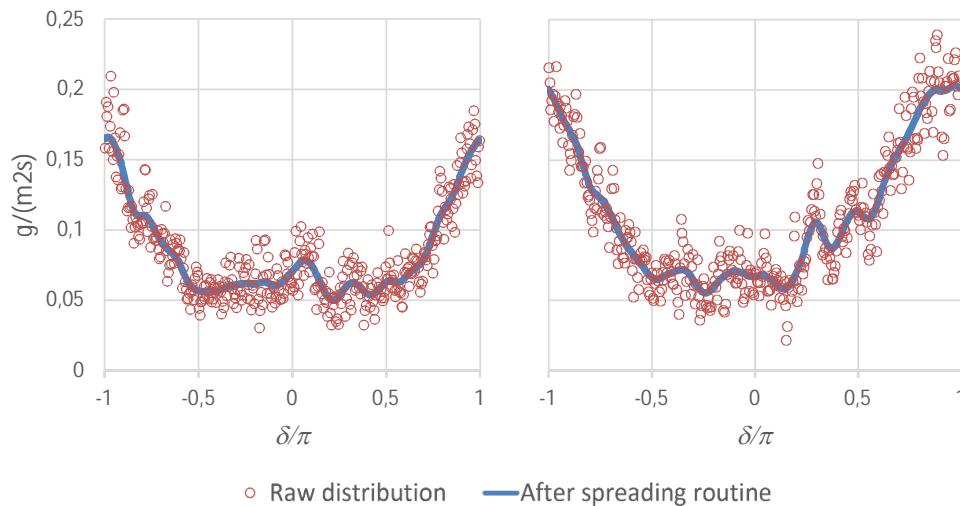


Figure 5.9: Mass deposition rates around the tube perimeters of the fourth cycle for the last tube of the second plate (left) and for the first tube of the fifth plate (right) as a function of the tube coordinate  $\delta$ .

## 5.6 Results and discussion

### 5.6.1 On the heat transfer rates

Seventeen samples were simulated with different fouling conditions and at different inlet properties according to the parameters specified above (Table 5.3), covering about nine hours of combustor operation. The variation of the heat transfer rates were analyzed. There are measurements available for the evolution of the global heat transfer coefficient ( $U$ ) of the combustor [III], defined as:

$$U = \frac{\dot{Q}}{A \cdot \text{LTD}} \quad , \quad (5.2)$$

where  $\dot{Q}$  is the heat rate lost by the gas,  $A$  is the heat transfer area and LTD is the logarithmic temperature difference over the heat exchanger between the tube temperature and the gas temperatures.

The model presented here is two-dimensional. Therefore, any result on the heat transfer rates is computed in units of power per unit of perpendicular length. Thus, the model does not take into account how the heat is transferred in the circular tube bends, which corresponds to a somewhat significant share of the total heat transfer area  $A$ . The heat transfer rate yielded by the model  $\dot{q}$  is computed, in  $\text{W}/\text{m}_\perp$ , as:

$$\dot{q} = \rho_g u_\infty H c_p (T_\infty - \overline{T}_{out}) \quad , \quad (5.3)$$

where  $\rho_g$  is the density of the upstream flue gas,  $H = 15.24$  cm is the transverse size of the computational domain (i.e., the height of the rectangle of the mesh, Figure 5.4), and  $c_p$  is the specific heat of the gas.  $\overline{T}_{out}$  is the averaged (in space and in time) temperature of the gas at the outlet.

The modeled heat transfer coefficient is:

$$U_m = \frac{\dot{q}}{A_m \cdot \text{LTD}_m} \quad , \quad (5.4)$$

where  $A_m = 1$  m<sup>2</sup>. The magnitudes  $U$  and  $U_m$  may not be compared directly since they are referenced with different areas in the two cases: a three-dimensional experiment and its two-dimensional simplification. Nonetheless, the relative evolution of both  $U$  and  $U_m$  should be theoretically similar, under the assumption that the fouling layer on the tube bends affects the whole heat transfer rates in a similar way as the fouling layer on a straight tube.

In Figure 5.10 the measured  $U$  (blue line, [III]) can be contrasted to the modeled  $U_m$  (red line). A modified modeled chart, estimated with a deposit thermal conductivity value of  $k = 0.32$  W/(m·K) is plotted in green. The evolution of the incoming flue gas velocity (also plotted in Figure 5.5) is presented in purple following the right Y-axis. It can be noted how the variations of  $u_\infty$  have a direct impact on the heat transfer rates for all the other lines.

At the beginning of the measurements [III],  $U = 93.38$  W/(m<sup>2</sup>·°C); and the modeled value of  $U_m$  for the first cycle is 36.10 W/(m<sup>2</sup>·°C). These initial values represent the 100% of the heat transfer rate at the zero minute mark. The aim is to visualize the relative time variations of these trends in  $U$  over time. It can be noted how they separate at the beginning.  $U$  increases steeply during the first 30—40 min of operation due mostly to the increase on the upstream flue gas velocity which entails a higher convective heat transfer

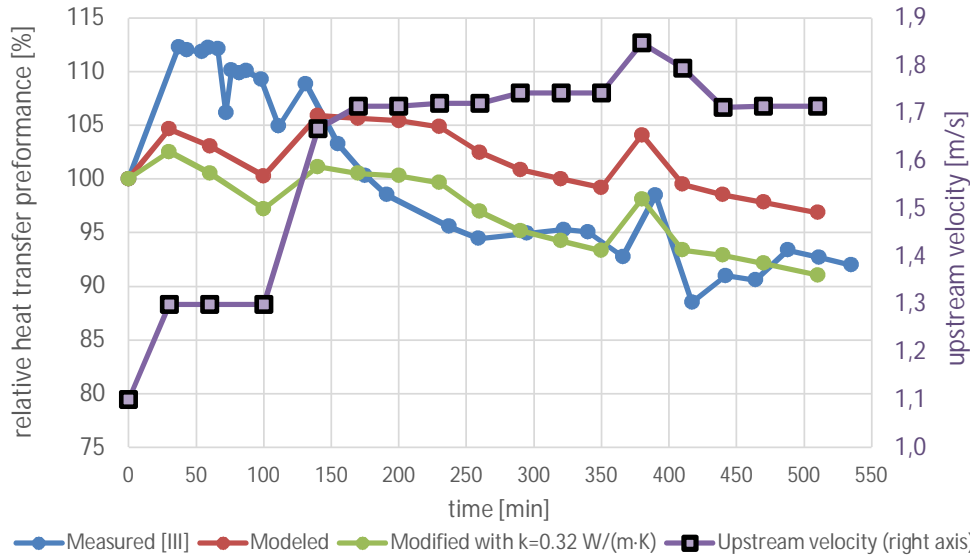


Figure 5.10: Temporal evolution of the relative heat transfer rate (in % compared to the starting value) of  $U$  (measured evolution),  $U_m$  (modeled evolution),  $U'_m$  (modified evolution) and  $u_\infty$  in the right axis.

coefficient. However, after the first cycle the model predicted a slightly lower global heat transfer: the increase on the convection is overcome by the remarked conductive heat transfer resistance. The model has overestimated the conductive resistance during the first few cycles, and this may be caused by a combination of the aforementioned uncertainties (Section 5.1.2), out of which the following ones are stressed:

- The deposition rates may have been overestimated, especially in the first tubes because the incoming upstream flow may not have been adequately modeled as mentioned earlier. This issue is made clear in a subsequent figure.
- The conductive heat transfer resistance is inversely proportional to the deposit thermal conductivity and to its solid fraction, parameters that were not directly measured, but qualitatively estimated.
- A delay in ash deposition after clean probe measurements of industrial boilers was reported by Vähä-Savo *et al.* [23]; meaning that no significant deposition is observed on a clean tube or probe during some time, after which the particles start to deposit and accumulate faster. In other words, the surface of a clean, fresh tube (like it is at the beginning of the study [III]) is not significantly sticky for ash particles, which take some time to start depositing onto a clean surface. Afterwards, subsequent particles may stick much better in an already formed

deposit layer. The model presented here does not take this phenomenon into account.

- The startup of the combustor is particularly characterized by relatively fast fluctuations and magnitude changes that are not captured by the model.

Due to the aforementioned reasons, the model may have failed to predict accurately the heat transfer performance during the first cycles, creating an error. The trend showed to be somewhat more correct in the later cycles.

To highlight up to which point the model depends on the conductive resistance, the outcome that would have been obtained with a different value of the deposit thermal conductivity can be approximated as follows. The global heat transfer coefficient is a function of the convective heat coefficient  $h$  and the conduction resistance  $R_{cd}$ :

$$U_m = \frac{1}{\frac{1}{h} + R_{cd}} \quad (5.5)$$

At the first cycle, with clean tubes,  $R_{cd} = 0$ . Thus,  $h_1 = U_{m,1}$  is known. The convective coefficient for a tube bundle is approximately proportional to  $Re^{0.8}$  (a dependence given, for instance, by Gnielinski *et al.* [75]), and hence the  $h$  for any cycle  $i$  can be calculated as function of the incoming velocity and temperatures (inversely proportional to the density which is part of the Reynolds number):

$$h \sim Nu \sim Re^{0.8} \Rightarrow h_i \approx h_1 \cdot \left( \frac{u_{\infty,i}/T_{\infty,i}}{u_{\infty,1}/T_{\infty,1}} \right)^{0.8} \quad (5.6)$$

It is possible then to approximate  $h_i$  for each cycle and reverse Eq. 5.5 to calculate the corresponding heat resistances  $R_{cd,i}$  that the model is predicting. The results that would have been obtained if a different value of the thermal conductivity  $k'$  had been chosen can be estimated knowing that  $R_{cd,i}$  is proportional to  $k$ . The value of this approximation  $U'_m$  as a function of  $k'$  should:

$$U'_{m_i} \approx \frac{1}{\frac{1}{h_i} + R_{cd,i} \frac{k}{k'}} \quad (5.7)$$

where  $k$  is the original used deposit thermal conductivity, 0.398 W/(m°C).

By choosing adequately a tuned value of  $k' = 0.32$  W/(m°C), a good approximation to the experimental measurements is obtained. In addition, this  $k'$  falls within typical values [69] of deposit thermal conductivities. This variation of only the 19% of the original  $k$  yields much closer results to the measured data (see green chart in Figure 5.10), highlighting the importance of proper measurements of the deposit conductivity which

were not available here. Unfortunately, the results presented here are only speculative since the actual  $k$  of the experiment [III] is unknown, as it was not measured empirically. There would not be scientific value on repeating the model with this new, conveniently working value of  $k'$ . The purpose of these statements is not to defend or criticize the reliability of the model but to highlight how the results are highly dependent on certain key parameters, emphasizing the importance of determining them reliably.

### 5.6.2 On the deposit shapes

Figure 5.11 sketches the shapes of the deposits which were measured after the 19h and 19 min of combustor operation. It should be noted that the figure has been drawn only from three discrete values of the deposit thickness at the tube lee, wind and side (averaged between the two sides). Therefore, the deposits seen in the figure for each tube are symmetrical. Figure 5.12 shows, the predicted modeled deposit shapes after the last calculated fouling cycle, i.e., after 9h and 10 min of fouling.

It can be noted that in general the model has overestimated the deposit thickness, since, thicker deposit layers than those that had been measured after 19 hours of operation were reached by the model in already slightly more than 9 hours. Certainly, the deposits grow slower with time, but usually not slower enough [VI] to compensate this effect. The modeled thickness depends highly on the deposit solid fraction, which was not measured properly either, but estimated (as it happened with  $k$ ). Smaller porosities than the used value of 0.764 are also possible [1, 69] and would have yielded better results, although, as it was stated for the case of the thermal conductivity, repeating the calculations with a tuned value of a parameter would have no scientific value. The approximations and the mechanical material properties that take part in the sticking submodel also may contribute to the aforementioned model deviation from the experimental values.

In addition, it can be appreciated that the model exaggerates particularly the deposits of the first tubes of the plates 2 and 4 over the deposit of other tubes. This is likely to have been caused by the differences between the actual flow patterns and fluctuations at the inlet and the modeled upstream flow. Thus, the modeled flow patterns around these tubes may not have been realistic enough to predict reliably the particle arrival rates. In addition, as it has been stated in other ash deposition studies [1, 9, 69], the deposit solid fraction may not be uniform around the tube circumference. It is more likely that the wind areas, more prone to inertial impaction, show a somewhat denser particle packing than the loose unconsolidated deposits formed in the tube lees by other softer deposition mechanisms (like e.g. thermophoresis or Brownian motion). It would be desirable to account for the local variation of the deposit solid fraction within a deposit in future approaches for better results.

Another source of uncertainties for these differences between the observed and modeled results is the actual ash particle size distribution that comes upstream of the computational domain. The measured values shown in Section 5.3.2 were used in this model. However,

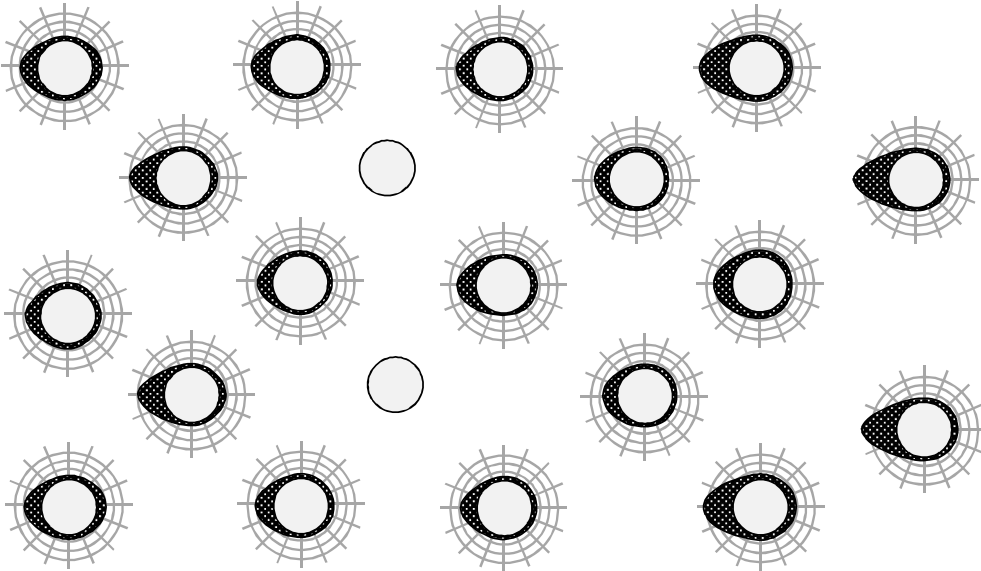


Figure 5.11: Measured deposits after 19 hours of fouling (Figure 7 of [III]). The gas comes from left to right. The spaces between tubes are not to scale. The radial divisions are 2 mm long, the angular divisions are  $\pi/8$  rad. The deposit of the second tube of the plates 2 and 4 could not be measured [III].

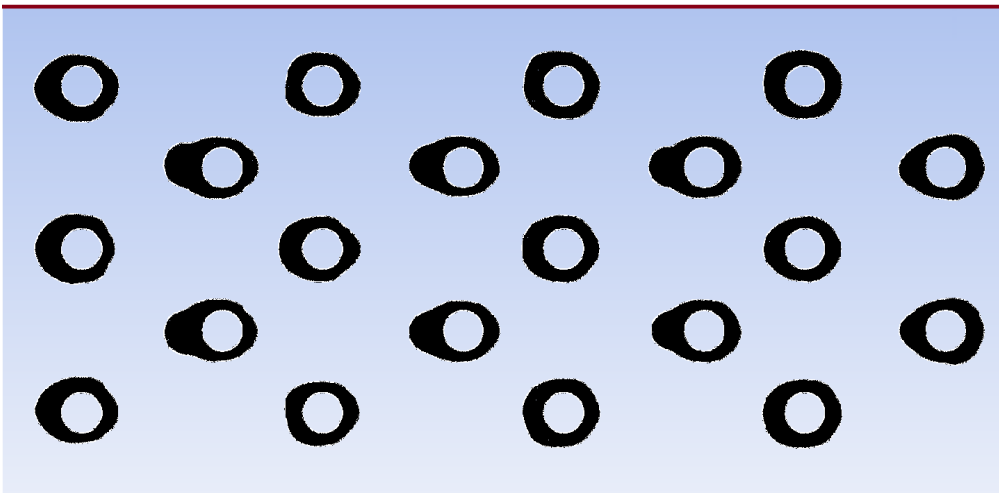


Figure 5.12: Modeled deposits after the last cycle (9 hours and 10 minutes of fouling time). The gas comes from left to right. The spaces between the tubes are not to scale.

those measurements were taken upstream of the first heat exchanger of the combustor, and it is unknown how transversally-distributed and in what fraction these particles make it to the second heat exchanger, the target of this study.

## 5.7 On the limitations of the model

This chapter has highlighted the challenges and difficulties that the model presented in this dissertation may face regarding the accurate prediction of fouling phenomena. Particularly, the importance of the availability of key parameters like the thermal conductivity and the porosity of the deposits has been remarked.

In the articles included in this thesis [II, VI], the lack of relevant empirical data for validation of ash deposition models was briefly underlined. Now, it is also made patent here that even when some empirical values of deposit thicknesses are available, the data may be still insufficient. The second heat exchanger was selected here because the data of the tube deposit thicknesses for the first heat exchanger was incomplete [III]. This has resulted into some added complications, like e.g. the modeling of the fluctuating upstream gas velocity.

Additional limitations of this modeling approach must be acknowledged. For instance, its computational costs. Particularly fine meshes and short time-steps are essential, meaning that high computing power is required especially for the steps 2 and 4 of Figure 3.4. For the model presented in [VI], the calculation of one cycle takes about one day to a cluster of 4 parallel Intel Xeon E5-2660 CPUs (8 logical cores per CPU for a total of 32 parallel logical threads). When larger meshes or more realistic particle distributions are used instead of single-diameter distributions, the computational costs increase significantly: for the validation attempt of this chapter, it takes about 4 days to complete one cycle with 64 parallel threads of the same processor. It would not have been reasonable to perform this later study if the velocity of the flow had been higher (for instance 5—6 m/s), since it would have meant to increase the mesh resolution [8, 30] and a further decrease of the time-step length. It was not reasonable to include the first heat exchanger in the domain for an accurate inlet flow determination. It is still not reasonable to attempt three-dimensional approaches with minimum accuracy, or to model large sections of a boiler while accounting for detailed unsteady flow pattern predictions.

Since this model applicability is limited to relatively small-scale geometries and sections of the boiler, a proper prediction, estimation and implementation of the boundary conditions (not only the flow features but also possibly non-uniform ash particle spatial distributions and formation) may need to be modeled separately (e.g. with the larger-scale boiler models of Leppänen *et al.* [45] and Jokiniemi *et al.* [47]).

Another possible drawback of the model is the need for the coding and debugging of the FLUENT user-defined function necessary routines (the sticking model, the dynamic mesh and deposit growth model, the mass spreading algorithm, and other possible auxiliary

functions). This may be somewhat time-consuming if the user is not familiar with C programming language and UDF-specific macros.

These issues and limitations may be regarded as areas where improvement is possible, pointing to possible additional work. This thesis does not offer an all-terrain, fully reliable solution or tool in the field of fouling modeling, but just attempts to build on the previous state-of-art. Further improvement is encouraged, with perhaps some of the suggestions already outlined above in this section.

## 6 Conclusions

This thesis studied fly ash fouling phenomena. Emphasis was given to the unsteady flow patterns of the flue gas in tube banks which seem to affect significantly the trajectories of the finest ash particles.

A CFD model for ash deposit growth simulation has been developed and presented. The model has been used in an attempt to simulate the flow, to examine the resulting flow patterns and to explain fouling-related phenomena of a periodical 2D row of four in-line tubes of a kraft recovery boiler bank [II, IV, VI]. For verification, it has also been used to simulate empirical measurements of probing in KRB [I] and a coal ash combustor ([III, VII], Chapter 5). The major relevant novelties in modeling were:

- a) The unsteady treatment of the flow and the fouling phenomena. The usage of an unsteady flow solver is not a common practice due to the high calculation times.
- b) The sample—cycle time extrapolation strategy, which is possible and moderately reasonable thanks to the mass spreading algorithms.
- c) The deposition growth model given by the dynamic mesh routines (detailed in Appendix B) used to execute the mesh node displacements (Eq. 3.5).
- d) The improvement of a previously-used sticking models with the inclusion of the empirical correlations by Li, Brach and Dunn for the Konstandopoulos rebound criterion; and the estimator for the internal plastic stress ratio  $\lambda$  (Eq. A.14).
- e) The customized drag law which allows for the spatial and particle-wise determination of the Cunningham factor affecting the trajectories of the smallest particles.

These tools have been used to answer the proposed research questions. The results and findings were summed up in Chapter 4. The key findings of this work are perhaps:

- a) The flow: the velocity field patterns over tube arrays present unsteady oscillations and therefore the flow is not properly predicted under the often-made assumption of steady state flow conditions.
- b) Non-uniform deposition trends and behavior: for instance, it could be observed that  $0.7 \mu\text{m}$  particles formed somewhat rounder deposits wrapping the tubes, in contrast to the deposits observed for  $3.62 \mu\text{m}$  particles which were more uneven. Also, the deposits were different at different tubes; suggesting that the traditional one-tube probing at boilers might not be reliable for the determination of the fouling trends throughout a whole heat exchanger.
- c) Deposition magnitudes: the definition and usage of the normalized particle arrival and deposition rates is given in this study. In addition, the thermophoresis propensity magnitude has been proposed since it seems to be more illustrative and informative than the temperature gradient for the determination of the thermophoresis trends of the ash particles.

- d) Model complexity: for a particular case in this study, it has been found that enhancing the model with more accurate sticking submodel did not mean a significant improvement on the results. A question arises on how complex models should reasonably be, since in some of the cases studied here a primitive model yielded the results which were similar to the ones of an improved version. On the other hand, a fine grid resolution and an accurate particle drag law seemed to be of major importance.
- e) Model accuracy: The need for fine and accurate grids has been remarked in this thesis. In addition, some considerations were given in Paper [VI] on the advantages of increasing the computational costs of the model to simulate as many as thirty flow oscillations of fouling time; as long as adequate mass-spreading is performed to obtain reasonably realistic ash deposition distributions from the scattered and somewhat biased computed (sampled) distributions.
- f) Challenges on using models for actual deposit prediction: it was stated in Chapter 5 that the complex nature of this phenomena makes its implementation and modeling rather challenging. Startup or initial conditions, operation fluctuations, relevant material properties, and boundary conditions are significantly relevant and may be hard to obtain or implement. As a consequence, rigorously scientific model validations might probably require high costs on measuring equipment and/or proper and a very accurate set up of controlled experiment conditions in pilot-scale empirical investigations.

The tools for ash deposition prediction in the current state-of-the-art are still in a somewhat early stage and their results must be interpreted with care. The model presented here is not an exception to this claim, since it was not possible to validate some aspects of the simulations performed. In addition, it was not reasonable to perform grid convergence studies due to the high computational costs of the model with the fine meshes used. Since neither a complete validation nor a grid convergence study were possible, the results that have been concluded here should be regarded as qualitative at their best.

Those issues and limitations may be considered as areas where improvement is possible, encouraging possible additional work. This thesis aims to go one step ahead of the previous state-of-the-art, allowing for the explanation of certain relevant phenomena and issues related with flow patterns and fouling. Especially useful for obtaining the aforementioned results was the time-dependent flow calculations on tube arrays, instead of stationary flows on a single tube.

The model proposed here could be improved further, not only by overcoming the previously mentioned limitations and simplifications, but also by enhancing it with new modeling capabilities. Inertial impaction and thermophoresis have been consistently identified as the causes of deposition, since the model did not account or simulate other

deposition mechanisms. The direct nucleation of ash aerosols, or the synergies between differently-sized particles (e.g., the presence of fine ash particles may rise the stickiness of the larger particles) have not been considered in this study. Moreover, it is possible to account for deposit sintering, reacting chemical species in the gas, partially-molten particles, or other fouling-related phenomena by using the different capabilities of the software package and the user-defined routines. The ash deposition is an active research field with numerous scientists and engineers carrying out further work and developments beyond the current limits. The present dissertation just intended to contribute with a minor improvement.



## Appendix A: Outline of the particle sticking—rebound model

This appendix outlines the algorithm for the particle sticking—rebound computing used in this thesis [IV—VII]. For sake of space, the whole routine could not be stated completely in those papers. This text gives enough guidelines for the full reproduction of the model, without deriving and explaining the origin of each equation and approach used. Further explanations and derivations of this model are given in the works of van Beek [6], Konstandopoulos [7], and Brach, Dunn and Li [61, 62].

### A.1 Relevant magnitudes and definitions

#### A.1.1 Particle magnitudes

This appendix follows the same criteria and notation used in Papers [IV, VI, VII] which are summarized in Figure A.1.

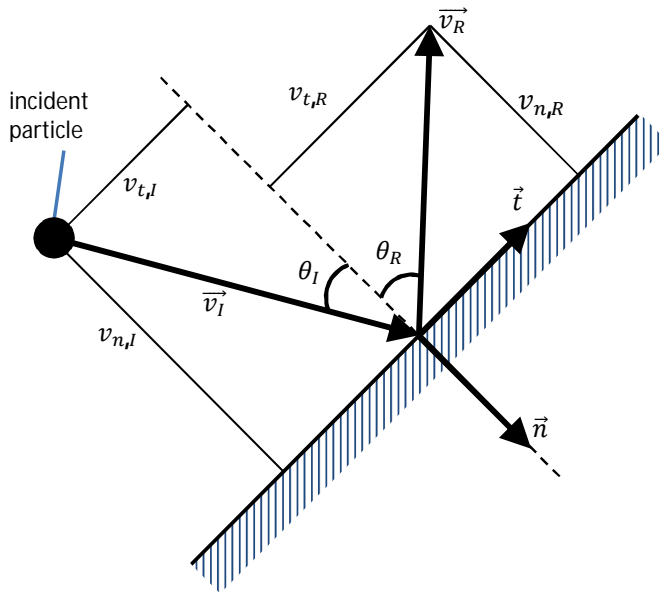


Figure A.1: Nomenclature of a particle impaction.

The vectors  $\vec{t}$  and  $\vec{n}$  constitute an orthonormal base where  $\vec{n}$  must point towards the deposit and  $\vec{t}$  must point along the direction of the impact. The incoming particle velocity  $\vec{v}_I$  can be thus decomposed in this (normal, tangential) base as  $[v_{n,I}, v_{t,I}]$ . In a similar fashion, the rebound velocity (if the particle rebounds) is  $\vec{v}_R = [v_{n,R}, v_{t,R}]$ . Note that, according to these sign criteria, all the components are positive except  $v_{n,R} \leq 0$ .

The particle radius  $r_p = d_p/2$  and mass  $m_p$  are also used in this model.

### A.1.2 Material and surface properties

This model assumes that a particle hits onto another particle that is already deposited, and that the particle and the deposit are made out of the same material. The material properties that are required are summed up in Table A.1.

Table A.1: Material properties used in the model. The values for  $K_2SO_4$  used in Papers [IV, VI] are also shown.

Symbol	Magnitude	Observation, definition	Values for $K_2SO_4$ [6]
$\rho$	Density	density of the material, not the apparent density of a porous deposit	2665 kg/m <sup>3</sup>
$E$	Young modulus	ratio of linear elastic stress to deformation	$3 \cdot 10^{10}$ Pa
$\nu$	Poisson coefficient	negative ratio of transverse to axial strain	0.3
$Y$	Uniaxial yield stress	stress limit beyond which a material experiences plastic deformation	$4 \cdot 10 \cdot 10^8$ Pa
$\Gamma$	Adhesion work per unit of area	$\Gamma = 2\sqrt{\gamma_1\gamma_2}$ where $\gamma_1, \gamma_2$ are the surface energies of the impaction materials	$\gamma_1 = \gamma_2 = 0.15$ J/m <sup>2</sup> $\Gamma = 0.30$ J/m <sup>2</sup>

Talbor [76] recommends that the uniaxial stress  $Y$  be approximated as one third of the Vickers indentation hardness, as this is more often found in material databases than  $Y$ :

$$Y \approx H_V/3 \quad . \quad (A.1)$$

### A.1.3 Surface properties

Contact mechanics are applied to the incident particle and to the deposit. The deposited particles in the vicinity of the impact location receive a certain amount of energy which is involved in the rebound potential of the hitting particle. For this purpose, the deposit response and its mechanics are modeled as those of another particle that would have, generally, larger size and mass than the hitting particle. This depends on how consolidated and tightly packed the particles composing the deposit are. The ratio of affected deposit mass to the mass of the hitting particle is denoted by  $C_m$ .

Also, the friction coefficient  $f$  of the surface becomes relevant for the determination of the critical angle and the slip—rotation rebound condition, if applicable (these shall be explained below). This parameter is somewhat difficult to determine since it depends on the surface smoothness, humidity, and particle distribution within the surface. These factors can vary significantly even locally due to some tube zones being more prone to

certain deposition mechanisms like inertial eddy impaction as opposed to thermophoresis or Brownian motion.

The work of van Beek [6] suggests a value of  $C_m = 2$  for powdery, unconsolidated deposits (as they are for fouling of solid ash particles [1]) and  $f$  to be assumed within typical values of friction coefficients of ash deposits, i.e., between 0.1—0.7.

#### A.1.4 Critical impact angle

The current sticking—rebound model is based on an analysis of the energies (kinetic, internal stresses, surface) involved in an impaction, which is derived by van Beek [6]. Depending on these criteria, a particle may stick if, and only if, it does not have enough energy to detach from the surface after the impaction. However, that theoretical model is not applicable for very oblique impacts. Empirical observations have shown that no particle is able to stick (regardless of the energy criterion) to any surface if the incidence angle  $\theta_I$  is larger than a certain critical value  $\theta_{cr}$  (Figure A.1) [7, 61, 62]. This occurs because at very oblique impacts the local surface roughness and orientation variations become very significant in the contact mechanics, and the assumptions under which the energy model was built do not apply any longer.

Konstandopoulos [7] proposed a semi-empirical method to derive this angle, which correlates approximately to:

$$\tan(\theta_{cr}) \approx 6.547f \sqrt{\frac{2-2\nu}{2-\nu}} \quad (A.2)$$

## A.2 Mechanistic model for non-oblique impacts

When  $\theta_I < \theta_{cr}$  the conditions for the van Beek energy model of particle impaction apply. A deep derivation and justification of this method can be found in [6] with detail. The algorithm is roughly outlined here with minor comments about the expressions and magnitudes involved, except for some steps where modifications to the model have been elaborated. Those modified steps are detailed properly.

In case of oblique impacts ( $\theta_I > \theta_{cr}$ ), this section does not apply (the particle always rebounds). The rebound velocity calculations for this case are given in Section A.3.

### A.2.1 Starting parameters and definitions

The impact between two finite particles of given properties shall be modeled as the contact of a certain particle with so-called *effective* properties (Young modulus, mass and radius) against a particle of infinite mass and radius. Due to the shape and nature of the

actual impacting bodies (incident particle and deposited particle), assumed spheres of same radii and material, these effective parameters are:

$$E^* = \frac{E}{2(1 - \nu^2)} \quad , \quad (A.3)$$

$$m^* = m_p \frac{C_m}{1 + C_m} \quad , \quad (A.4)$$

$$r^* = \frac{r_p}{2} \quad . \quad (A.5)$$

The impaction kinetic energy  $E_{k,I}$  is defined as:

$$E_{k,I} = \frac{1}{2} m^* v_{n,I}^2 \quad . \quad (A.6)$$

When a particle hits a surface, it compresses and deforms. The critical plastic-deformation velocity  $v_{n,lim}$  is the limit of  $v_{n,I}$  below which this internal deformation is entirely elastic. For cases where  $v_{n,I} > v_{n,lim}$ , the particle would experience a mixture between plastic and elastic internal strains, and the equations governing the internal mechanics are different for both cases. This limit depends only on the material and is given by:

$$v_{n,lim} = \frac{\pi^2}{\sqrt{10\rho}} \frac{(0.795Y)^{5/2}}{E^{*2}} \sqrt{\frac{1 + C_m}{C_m}} \quad . \quad (A.7)$$

## A.2.2 Stored mechanical energy and contact radius

The algorithm flow splits in two branches at this point. If  $v_{n,I} \leq v_{n,lim}$  the equations for pure elastic deformations are used (Section A.2.2.1). Otherwise, the algorithm follows through Section A.2.2.2. Regardless of the path followed, the procedure continues further through Section A.2.3. The target of this step is to obtain the stored mechanical energy due to the internal stresses ( $E_{pl} + E_{el}$ ) and the contact radius  $r_c$ .

### A.2.2.1 Case of purely elastic particle deformation

When a particle hits the deposit surface, it reduces its normal velocity to zero and deforms as a consequence of the internal stresses generated from the incoming kinetic energy. The incident kinetic energy  $E_{k,I}$  (eq A.6) and the surface energy  $E_{A,I}$  associated with the contact particle-surface area are converted into internal elastic energy  $E_{el}$ :

$$E_{k,I} + E_{A,I} = E_{el} \quad . \quad (A.8)$$

The new two energies of the previous equation are computed as:

$$E_{A,I} = \Gamma\pi r_{el}^2 \quad , \quad (A.9)$$

$$E_{el} = \frac{2}{5} \frac{F^{5/3}}{\left(\frac{4}{3}E^*\right)^{2/3} r^{*1/3}} \quad ; \quad (A.10)$$

where the elastic contact radius  $r_{el}$  is given by

$$r_{el}^3 = \frac{r^* F}{(4/3)E^*} \quad . \quad (A.11)$$

$F$  is the force acting upon the particle deforming it against the surface. The previous four equations constitute system with four unknowns:  $E_{el}$ ,  $E_{A,I}$ ,  $r_e$  and  $F$ . It can be solved by substituting Eqs. A.9—A.11 into Eq. A.8 and rearranging to obtain an equation of the form of  $x^5 = A + Bx^2$  where  $x = \sqrt[3]{F}$  and the coefficients  $A$  and  $B$  are computable with already-known values:

$$A = 2.5 \cdot E_{k,I} \left(\frac{4}{3}E^*\right)^{2/3} r^{*1/3} \quad , \quad (A.12)$$

$$B = 2.5\pi\Gamma r^* \quad . \quad (A.13)$$

This 5<sup>th</sup>-degree equation may be solved for  $x$  and then cubed to obtain  $F$ . Starting from the initial guess of  $x_1 = \sqrt[5]{A}$ , the subsequent solutions  $x_{n+1}$  converge quickly if the iteration scheme  $x_{n+1} = \sqrt[5]{A + Bx_n^2}$  is used. Once solved, the total stored mechanical energy  $E_{el}$  may be computed with Eq. A.10.

There is no plastic deformation, thus  $E_{pl} = 0$ . Finally, the radius of the contact surface  $r_c$  is equal to  $r^*$  for pure-elastic deformation (it will not be so if plastic deformations take place).

### A.2.2.2 Case of plastic-elastic particle deformation

For an impacting spherical particle, the stress limit beyond which plastic deformation starts to occur is  $1.59Y$ . However, the maximum stress which can be found may be larger, in the form of  $\lambda Y$ , for some  $\lambda > 1.59$ . Stresses beyond  $\lambda Y$  would cause the material flow. Here,  $\lambda$  is a parameter which may vary from 1.59 in the limiting case of almost no plastic deformation and the internal load being exactly equal to the plastic deformation threshold, up to 3.20 for a very heavy impact would deform the whole particle plastically. Generally none of these limits would happen and there would be plastic deformation within the central regions and elastic deformations elsewhere.

Figure A.2 sketches these definitions. Let  $r_{tot}$  be the radius of the deformation area in the particle, and  $r_{pl} < r_{tot}$  be the radius of the plastic deformation region. As a consequence of the previous definitions,  $v_{n,I} = v_{n,lim} \Leftrightarrow \lambda = 1.59 \Leftrightarrow r_{pl} = 0$ ; and, on the other hand,  $v_{n,I} > v_{n,lim} \Leftrightarrow 1.59 < \lambda < 3.20 \Leftrightarrow 0 < r_{pl} < r_{tot}$ .

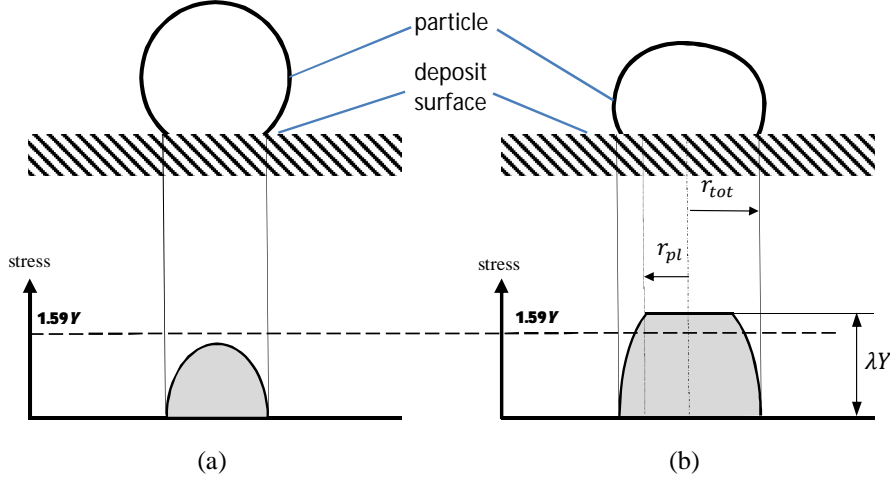


Figure A.2: Comparison of stress distribution within a particle deforming (a) elastically and (b) plastic-elastically.

An estimation of linear behavior of  $\lambda$  with the fraction of plastic to total deformation area does not appear in the original model [6] and is proposed in this thesis:

$$\lambda = 1.59 + \left(\frac{r_{pl}}{r_{tot}}\right)^2 (3.20 - 1.59) \quad . \quad (\text{A.14})$$

Unfortunately, the procedures of the original model require to know  $\lambda$  beforehand to determine the deformation radii. Hence, it is proposed here to start with an initial guess of  $\lambda$  and proceed with the following expressions and equations detailed from the next paragraph onwards. Once these are solved for  $r_{pl}$  and  $r_{tot}$ , it is possible to use them in Eq. A.14 and iterate with a better  $\lambda$  until convergence. In the CFD studies included in this work, an initial value of  $\lambda_1 = 2.10$  has been used.

The energy balance is not identical to the pure elastic case, shown in Eq. A.8. When some plastic deformation occurs, the stored energy due to plastic deformation  $E_{pl}$  and the loss of energy due to plastic material flow  $E_{loss}$  must be also accounted for:

$$E_{k,I} + E_{a,I} = E_{el} + E_{pl} + E_{loss} \quad . \quad (\text{A.15})$$

The kinetic energy was obtained already. As for the rest of terms, so far only  $E_{el}$  can be calculated directly:

$$E_{el} = \frac{2}{5} \left( \frac{2}{3} \right)^5 \frac{\pi^5 r^{*3} (\lambda Y)^5}{\left( \frac{4}{3} E^* \right)^4} \quad . \quad (\text{A.16})$$

The other terms of the balance are expressed as a function of  $F_{el}$ ,  $F$ , and known parameters:

$$E_{a,l} = \Gamma \pi \left( \left( \frac{\pi r^* \lambda Y}{2 E^*} \right)^2 + \frac{F - F_{el}}{\pi \lambda Y} \right) \quad , \quad (\text{A.17})$$

$$E_{pl} = \frac{1}{2} \left( \frac{2}{3} \pi \right)^2 \frac{r^*}{\left( \frac{4}{3} E^* \right)^2} (\lambda Y)^2 (F - F_{el}) \quad , \quad (\text{A.18})$$

$$E_{loss} = \frac{(F - F_{el})^2}{4 \pi r^* \lambda Y} \quad . \quad (\text{A.19})$$

$F$  is the force acting upon the particle to deform it against the surface.  $F_{el}$  is the limit load that would make the particle deform elastically. The term  $F - F_{el} > 0$  may be thus interpreted as the excess of force over the elastic limit, or simply, the plastic load. This equation set can be solved by substituting Eqs. A.17—A.19 into Eq. A.15. An ordinary algebraic second-degree equation  $A(F - F_{el})^2 + B(F - F_{el}) + C = 0$  is obtained for the plastic load, where the coefficients can be computed by using already known magnitudes:

$$A = \frac{1}{4 \pi r^* \lambda Y} \quad , \quad (\text{A.20})$$

$$B = \frac{\pi^2 r^* (\lambda Y)^2}{8 E^{*2}} - \frac{\Gamma}{\lambda Y} \quad , \quad (\text{A.21})$$

$$C = E_{el} - E_{k,l} - \Gamma \pi^3 \left( \frac{r^* \lambda Y}{2 E^*} \right)^2 \quad . \quad (\text{A.22})$$

The deformation radii can now be calculated from the plastic load  $F - F_{el}$ :

$$r_{pl} = \sqrt{\frac{F - F_{el}}{\pi \lambda Y}} \quad , \quad (\text{A.23})$$

$$r_{tot} = \sqrt{\left( \frac{\pi r^* \lambda Y}{2 E^*} \right)^2 + \frac{F - F_{el}}{\pi \lambda Y}} \quad . \quad (\text{A.24})$$

With  $r_{pl}$  and  $r_{tot}$  it is possible to estimate a new value of  $\lambda$  with Eq. A.14. However, Eq. A.14 may diverge if used directly. Nonetheless an under-relaxation factor  $\xi$  can be applied (Papers [IV—VII] used  $\xi = 0.70$ ) to the previous value of  $\lambda$  in the form of:

$$\lambda_{n+1} = \xi\lambda_n + (1 - \xi) \left( 1.59 + \left( \frac{r_{pl}}{r_{tot}} \right)^2 (3.20 - 1.59) \right) \quad . \quad (\text{A.25})$$

Once convergence has been reached, the magnitudes that will be needed for the sticking criterion can be computed.  $E_{el}$  and  $E_{pl}$  were obtained already, and the contact radius is:

$$r_c = \frac{3 E^* r_{tot}^3}{4 F} \quad , \quad (\text{A.26})$$

where the total load  $F$  may be computed from the plastic load ( $F - F_{el}$ ):

$$F = (F - F_{el}) + F_{el} = (F - F_{el}) + \left( \frac{2}{3}\pi \right)^3 \frac{r^{*2}}{\left( \frac{4}{3} E^* \right)^2} (\lambda Y)^3 \quad . \quad (\text{A.27})$$

### A.2.3 The sticking criterion

Now the contact radius  $r_c$ , either elastic or plastic-elastic, is determined and the stored mechanical energy can be calculated. The energy balance of a detaching particle is:

$$E_{el} + E_{pl} = E_{a,R} + E_{k,R} \quad . \quad (\text{A.28})$$

$E_{pl} = 0$  for pure elastic deformation cases. The left hand side of this balance is the internal mechanical energy of the particle at the moment of its maximum deformation, where its velocity is zero, and it has been already calculated. This is the energy available to cause a detachment. For a particle to detach and be re-entrained in the flow, some energy  $E_{a,R}$  must be spent to create new surfaces. The excess, if any, will make the particle rebound with a certain kinetic energy  $E_{k,R}$ ; but if there is not enough stored energy to create new surface, the particle would remain stuck:

$$E_{el} + E_{pl} < E_{a,R} \quad . \quad (\text{A.29})$$

The Eq. A.29 is the energy sticking criterion of a particle. The rebound surface energy may be calculated from the impact surface energy  $E_{a,I}$  with:

$$E_{a,R} = 7.09 \left( \frac{r_c^4 \Gamma^5}{E^{*2}} \right)^{1/3} + E_{a,I} \quad . \quad (\text{A.30})$$

#### A.2.4 Rebound velocities

If  $E_{a,R}$  satisfies Eq. A.29 this algorithm finishes since the particle sticks and stays in the surface to contribute to the deposit growth. Otherwise, the particle rebounds and its velocities must be calculated.

The normal rebound velocity is given by:

$$v_{n,R} = v_{n,I} \left( 1 - \left( (1 + e) \frac{C_m}{1 + C_m} \right) \right) \quad (\text{A.31})$$

where  $e$  is the coefficient of restitution of the particle impaction:

$$e = \sqrt{1 - \frac{E_{loss} + (E_{a,R} - E_{a,I})}{E_{k,I}}} \quad (\text{A.32})$$

Note that  $E_{loss} = 0$  for the pure elastic deformation case.

A rebounding particle may slip or rotate after the contact with the surface. This depends on the trajectories, restitution, and the friction coefficient. The rolling criterion is:

$$f > \frac{2 \tan \theta_I}{7(1 + e)} \quad (\text{A.33})$$

and affects directly the tangential rebound velocity calculation. If the previous equation is satisfied, the particle rolls and:

$$v_{t,R} = v_{t,I} \left( 1 - \frac{2}{7} \frac{C_m}{1 + C_m} \right) \quad (\text{A.34})$$

Otherwise, the particle slips and:

$$v_{t,R} = v_{t,I} \left( 1 - \frac{f(1 + e)}{\tan \theta_I} \frac{C_m}{1 + C_m} \right) \quad (\text{A.35})$$

### A.3 Rebound velocities for oblique impacts

When  $\theta_I > \theta_{cr}$  the microscopic roughness and friction of the impaction surface become determinant and the assumptions under which the previously sticking/rebound model was based do not apply, causing that an impacting be unable to stick under any energy condition [7]. New equations and correlations to compute the rebound velocities are thus

required. The model to compute these velocities has been proposed in Papers [IV—VII] and its equations are discussed next.

The loss of normal kinetic energy  $T_k$  is defined as:

$$T_k = \frac{v_I^2 - v_R^2}{v_I^2} \quad . \quad (\text{A.36})$$

It has been found empirically [61] that, for oblique impacts,  $T_k$  decays linearly to zero as the impaction angle  $\theta_I$  approaches to  $\pi/2$  rad. Therefore,  $T_k$  for oblique impacts can be approximated as:

$$T_k \approx T_{k,cr} \frac{\pi/2 - \theta_I}{\pi/2 - \theta_{cr}} \quad . \quad (\text{A.37})$$

$T_{k,cr}$  is the loss of kinetic energy at the limit case of  $\theta_I = \theta_{cr}$ .  $T_{k,cr}$  can be computed by testing the energy model, described in Section A.2, in the limiting case of  $\theta_I = \theta_{cr}$  and with an incident velocity  $v_I$  large enough, at least, to force a rebound. After the rebound velocities for this test case are obtained (Eqs. A.31—A.35),  $T_{k,cr}$  can be calculated from its definition in Eq. A.36 and used in Eq. A.37.

Nonetheless it could be possible to just estimate  $T_{k,cr}$  without having to go through all the calculations of the mechanistic model at each impaction event. For this purpose, the energy model has been tested for multiple particle diameters, impaction velocities and impaction angles varying within typical values of  $\theta_{cr}$  ( $45^\circ$ — $75^\circ$ ). Figure A.3 and Figure A.4 highlight the results for the  $T_k$  of rebounding particles and show that, roughly, it depends on  $\theta_I$  only, and not on the particle size or on its impaction velocity. Hence,  $T_{k,cr}$  must depend also on  $\theta_{cr}$  only, and in the same way. This dependence seems to be nearly linear, and the following regression may be used to approximate  $T_{k,cr}$  of Eq. A.37.

$$T_{k,cr} \approx 1.1621 - 0.6476 \cdot \theta_{cr}[\text{rad}] \quad . \quad (\text{A.38})$$

It is stressed that the previous expression has been deduced from impacts of particles of  $\text{K}_2\text{SO}_4$ , the properties of which were given in in Table A.1. For  $\text{SiO}_2$  particles (used in Papers [V, VII] and in Chapter 5) the behavior was also linear but with different coefficients:  $T_{k,cr} \approx 0.9857 - 0.4769 \cdot \theta_{cr}[\text{rad}]$ .

$T_k$  allows for the determination of the rebound velocity magnitude. Still the rebound direction is required. Empirical observations by Brach, Dunn and Li [61, 62] are used for this purpose. These observations reported that after oblique impacts, the particles often rebounded with unusually large normal velocities, even against intuition (i.e.,  $\theta_R < \theta_I$ ). Their findings [61, 62] adjust approximately to this correlation:

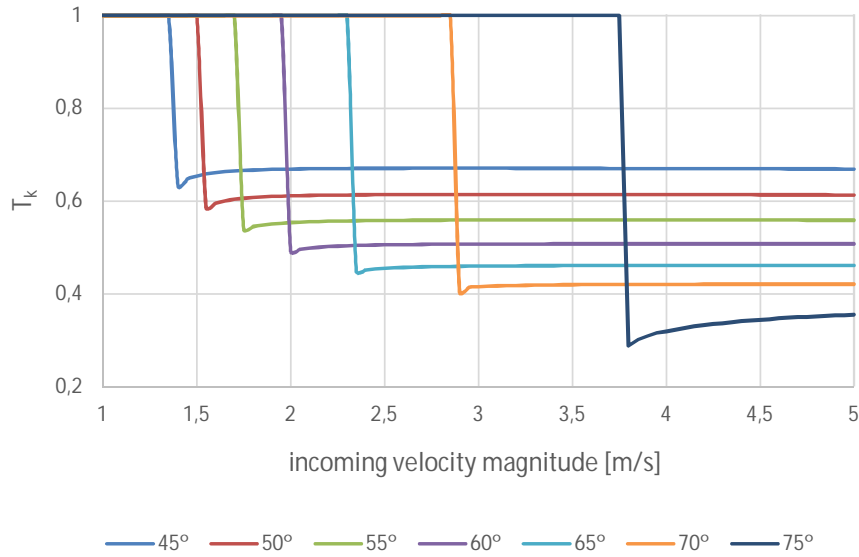


Figure A.3: Kinetic energy loss ( $T_k$ ) for  $K_2SO_4$  0.7  $\mu m$  particles at different impaction velocities  $v_I$  and angles  $\theta_I$ . For sufficiently low  $v_I$  at all angles it happens that  $T_k = 1$ : this means that the particles stick to the deposit. Calculated using the energy model of Section A.2.

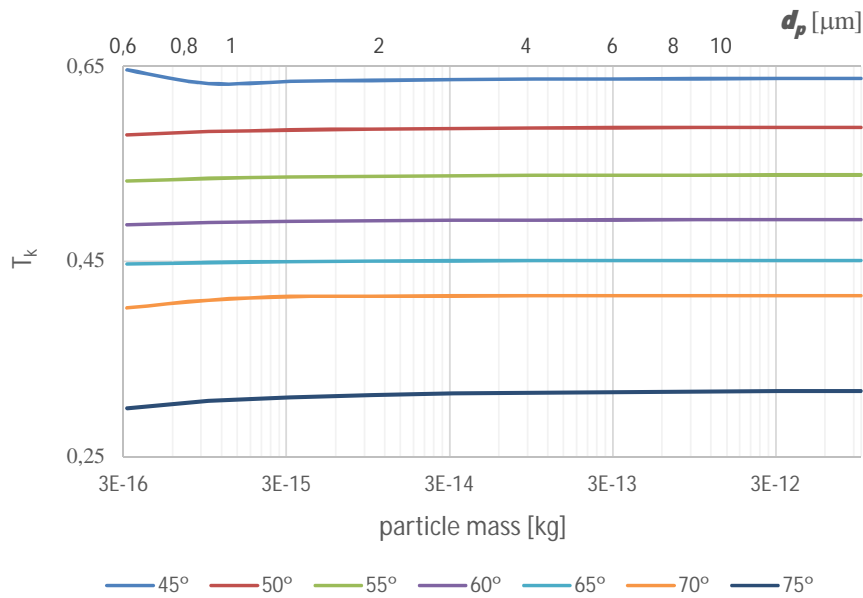


Figure A.4: Kinetic energy loss ( $T_k$ ) for differently-sized  $K_2SO_4$  particles with the same impaction velocity  $v_I = 5$  m/s and with different impaction angles  $\theta_I$ . Calculated using the energy model of Section A.2.

$$\frac{-v_{n,R}}{v_{n,I}} \approx \max\{0.75, z \cdot \theta_I - 1.20\}, \quad (\text{A.39})$$

where  $z = 2.04 \text{ rad}^{-1}$ . It seems that it is possible now to determine the rebound angle with simple trigonometry; namely  $\theta_R = \arccos(-v_{n,R}/v_R)$ . However, the observations of  $v_{n,R}$  that led to the previous correlation were somewhat biased, as stated by the original authors [61] themselves, because numerous particles rebounding almost in parallel to the impaction surface of their experiment were harder to retrieve and to account for.

It would be intuitive to think that some particles could as well experience a “mirror” rebound (i.e.,  $\theta_R = \theta_I$ ). Those particularly small observed rebound angles were caused by differences between the apparent surface orientation (determined by the macroscopic orientation of the impaction surface) and the microscopic surface orientation (where the particle actually hits) which presents accused local variations due to the surface roughness. As a consequence, any rebound direction between  $\theta_R = \arccos(-v_{n,R}/v_R)$ , with  $v_{n,R}$  calculated from the previous equation; and  $\theta_R = \theta_I$  might be possible a priori. Hence, it is suggested in this thesis to generate a pseudo-random value for  $\theta_R$  between those two thresholds and finally recalculate  $v_{n,R}$  as  $(-v_R \cos \theta_R)$ .

## Appendix B: Dynamic mesh routines for growing tube deposits

### B.1 Introduction

The deposit growth is simulated by moving the deposit-flow interface. If the only change happening to the grid was this interface displacement, soon the immediately adjacent fluid cells would collapse and reverse; and the solid cells of the deposit would become stretched. The so-called *smoothing* and *remeshing* methods, described in the FLUENT manual, [54] are applied to deform the fluid and solid cell threads to preserve grid integrity.

These capabilities may be executed after every dynamic mesh movement and are further discussed in the following section. Other different general-purpose mesh smoothing techniques are also available outside of the dynamic mesh model. These ones help maintaining a good quality grid in cases with highly unstable meshes. Tips to combine these general-purpose smoothing techniques with the dynamic mesh in-built smoothing and remeshing are given in Section B.3.

### B.2 In-built dynamic mesh smoothing and remeshing

Ansys FLUENT offers the following algorithms to be applied to those threads that have been marked as “Deforming” in the “Dynamic Mesh Zones” dialog box (Section 3.5). These routines may be applied only after deforming an interface.

#### B.2.1 Spring smoothing

The spring-based smoothing method treats the deforming grid as a network of interconnected springs. Therefore, the moving interface can be seen as a wall which is pushing these springs away, and the displacement is shared and absorbed by multiple cell layers away from the moving boundary. Thus, the nodes can re-locate and accommodate in order to share the deformation and preserve a better global mesh quality. Otherwise, the elements adjacent to the moving boundary would be too stretched or compressed, depending on in which side of the interface they are.

The damping of the spring network is controlled by a parameter called *spring constant factor*, for which, a value close to zero would lead to almost no damping. Therefore, a displacement of a zone is absorbed by cells which are far away. On the other hand, a value close to one will mean that the movement is completely absorbed by the closest cells. For this model it is suggested to use a value of zero in order to maintain possibly stretched and skewed elements far away from the fluid boundary layers. If good remeshing thresholds are set (which shall be defined and detailed better in a later section), the cells which are close to the moving boundary will maintain appropriate properties.

An alternative dynamic mesh *diffusion* smoothing method is also available, but it is more suitable for revolving surfaces [54] and hence here only the spring methods is suggested as it is adequate for translational deformations.

### B.2.2 Local-face remeshing

In spite of using spring smoothing methods, an excessive accumulated displacement of the interface will eventually lead to very coarse and stretched cells in the deposit and very small and compressed cells in the fluid. To avoid this, a local-face remeshing algorithm merges clusters of small cells into bigger cells, and reversely it splits very large cells into smaller ones. This process helps reducing the skewness of cells. The major disadvantage of a local-face remeshing is that it is only implemented for triangular cells in 2D meshes and for tetrahedral in 3D meshes. This is why quadrilateral cells cannot be used in the ash deposition model presented in this thesis and always triangular-paved meshes have been used.

There exist customizable thresholds for this cell splitting and merging. Minimum and maximum allowed cell sizes must be input to this routine. In addition, it is possible to choose a target maximum skewness to ensure that this method does not generate poor quality cells. There is not a standard way to determine good and appropriate values of these thresholds. In the first attempts of the model of this work they were obtained by trial-and-error of different threshold sets and by observing the different resulting meshes. For this purpose, the deposition collected after the first fouling sample can be used applied multiple times just to generate relatively large deformations and observe the behavior of the mesh. The thresholds used in Paper [VI] are shown in Table B.1 and they may be used as a qualitative suggestion.

Table B.1: Approximated thresholds for the local face remeshing algorithm.  $\Delta x_1$  is the length of a side of the cells adjacent to the interface (Figure 3.1). (\*): The maximum allowed cell size in the flue gas should be sufficiently larger than the largest cell of the domain, otherwise the whole grid would become finer than what was designed originally.

Threshold	Deposit cells	Flue gas cells
Minimum cell size	$\sim \Delta x_1$	$\sim 0.1\Delta x_1$
Maximum cell size	$\sim 2\Delta x_1$	$\sim 200\Delta x_1^{(*)}$
Target cell skewness	0.6	0.5

### B.2.3 Graphical examples of the effects of these methods

The necessity for these methods is best understood and justified with graphic examples of their application in the growing ash deposits modeled in this thesis. Figure B.1 shows the benefits of using these routines in the flue gas with the grid of the model of Paper [II]. Figure B.2 shows their effects on a deposit cell-zone of Paper [VI], highlighting what would occur if they were not used. Figure B.3 details the working procedure of the local face remeshing method.

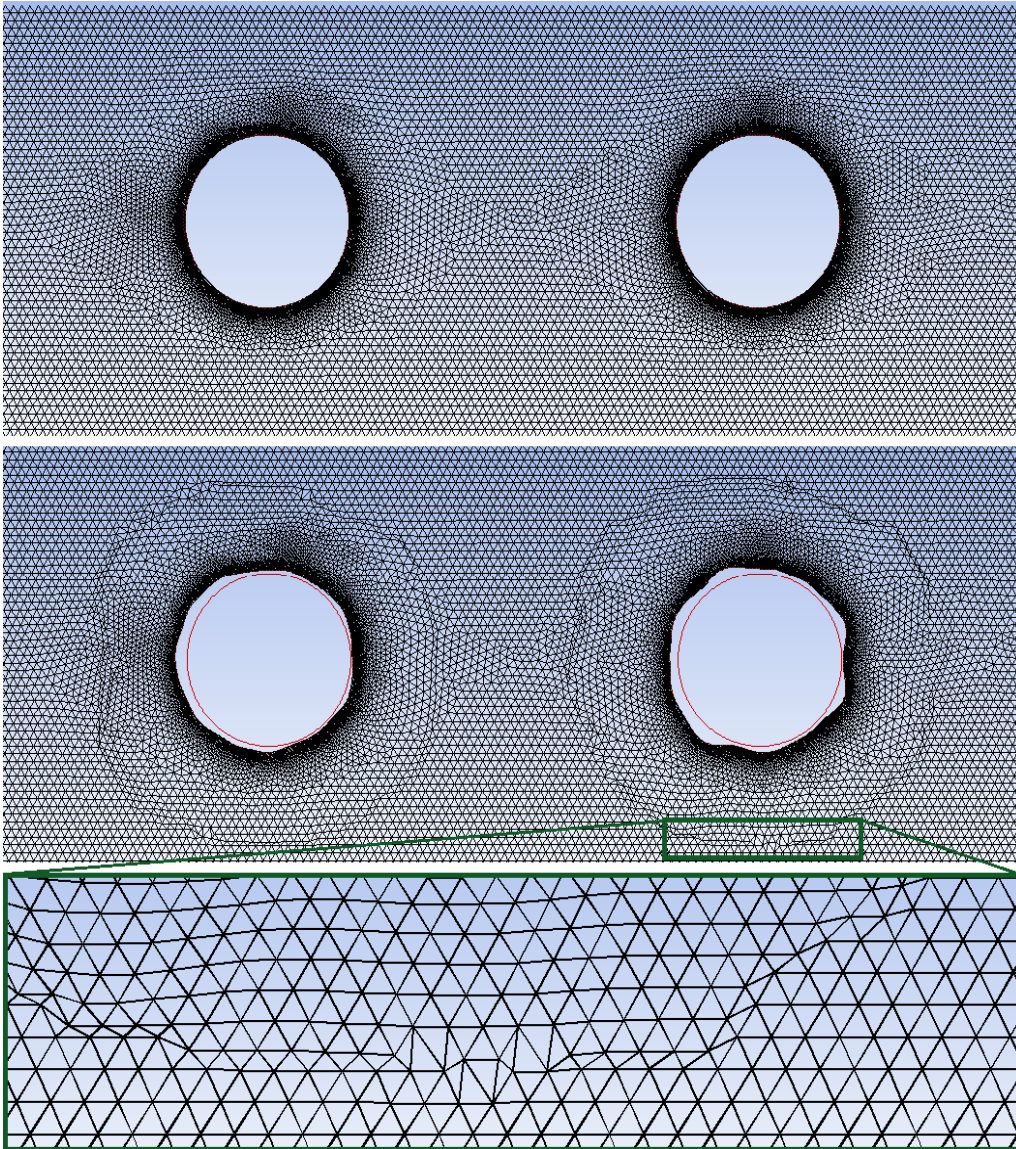


Figure B.1: Effects of rigid spring-smoothing in the flue gas (mesh of Paper [II]). Top: initial mesh (clean tubes). Middle: the same mesh after some deformation. Deposits can be observed wrapping the tubes. The spring factor is set to zero, hence the deformed cells fall somewhat far away from the tubes. Bottom: zoomed area of the lower part of the tube of the right. The line of compressed cells can be observed. Some cells around the center of this bottom subfigure have already been merged by the remeshing method. The rest of the compressed cells will be merged after subsequent deposit expansions. The remeshing method is also acting in merging some much skewed cells close to the moving boundary, although this is not appreciable in this figure.

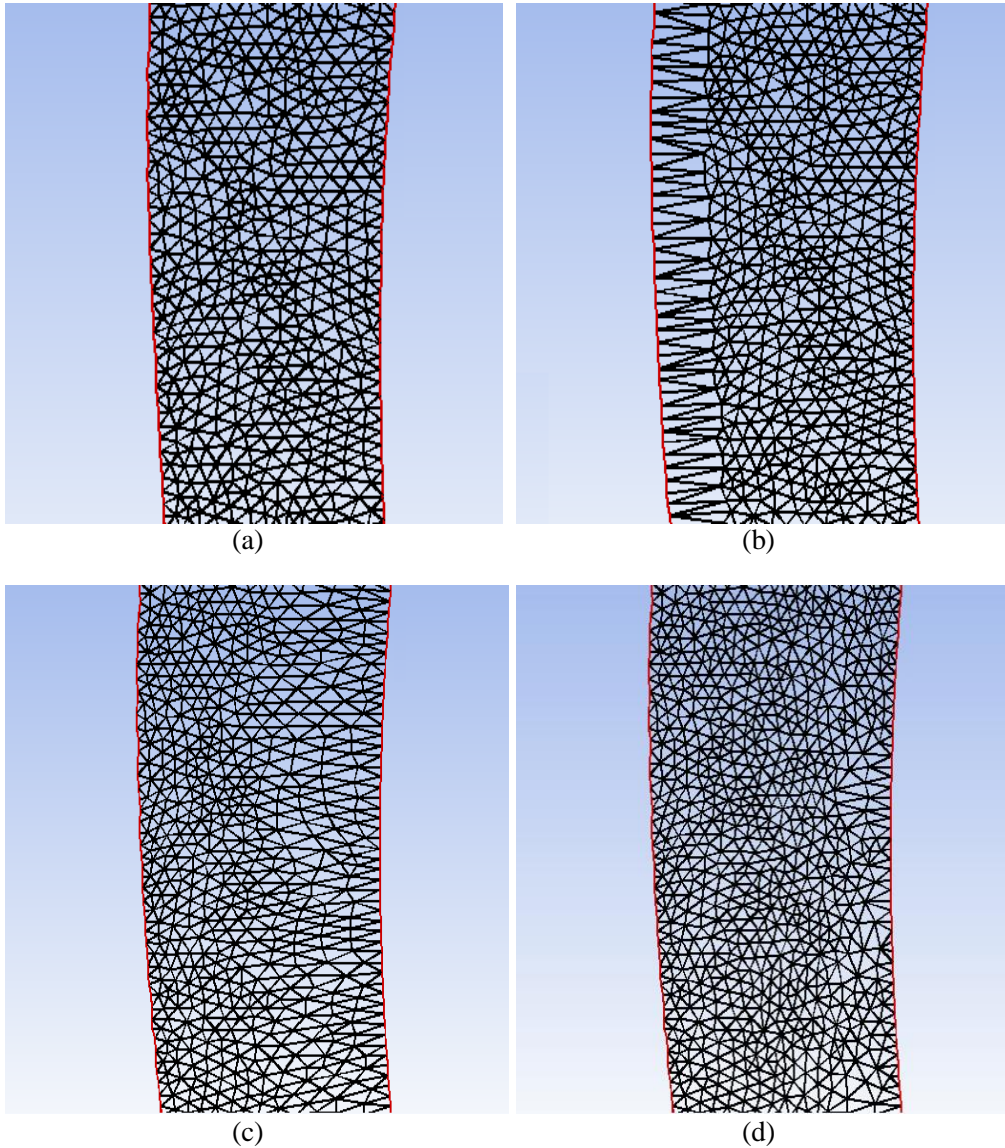


Figure B.2: Example of smoothing and remeshing effects on cell-zone deformations of a growing deposit wrapping a tube. (a): An initial condition, the left boundary will expand further to the left. (b): The same zone after a certain deformation, without any smoothing or remeshing method applied on the deposit area. The cells adjacent to the moving interface remain much stretched. (c): Same displacement with spring smoothing enabled, the spring constant factor is 1. The deformation has been shared among the cells that were far away from the moving boundary. (d): Same area as in (c) after four local-face remeshing iterations. The horizontally stretched cells of (c) have been split vertically into smaller cells to obtain less skewed elements.

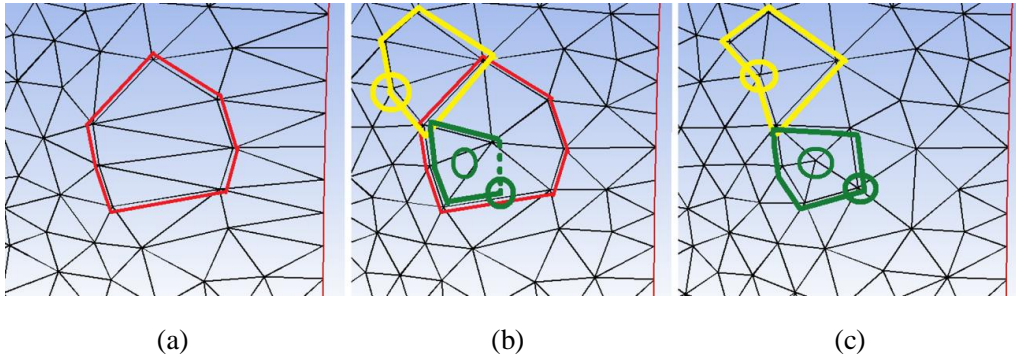


Figure B.3: Detail of some of the modifications that the local face remeshing method applies on the cells. These pictures were extracted from the process from (c) to (d) of Figure B.2. (a): A cluster of five highly-skewed cells (marked in red) will be modified. (b) The cluster that contained those five cell has been rebuilt with better quality cells (in red). Another cluster (in yellow) contains poor elements and will be fixed in the next iteration by moving the yellow-circled node and rearranging the cluster. Another set of cells (in green) is improved by creating two new cell nodes (identified inside green circles). Other cell rearrangements may be observed elsewhere within this figure.

### B.3 General smoothing and remeshing guidelines

After a dynamic mesh boundary moves, the smoothing and remeshing are applied automatically if they are enabled. However, it might happen that these methods are still not sufficient to maintain stable deformations and an overall mesh quality. Ansys FLUENT counts with other general-purpose mesh smoothing algorithms [54]. These smoothing routines differ from the already mentioned spring method on that they do not require any moving boundary or dynamic mesh setup. The spring-based smoothing only works after a boundary movement. These other methods can be called with the TUI command `/mesh/smooth`.

For instance, the skewness-based smoothing searches for a given most skewed percentile of cells and attempts to re-allocate their nodes in order to improve the quality of that cell and the neighboring ones. The face-swapping smoothing considers pairs of adjacent triangular cells. A pair of adjacent cells, together, form a quadrilateral, and one of the diagonal of this quadrilateral is a face which is shared by the two cells. This routine swaps the shared face by the other quadrilateral diagonal providing that this swapping helps improving the skewness of both cells. Other possible smoothing methods are available with slightly different features and properties [54].

It may be desirable to apply several remeshing iterations in between growth steps  $\vec{r}/n$ . However, it is not feasible to call explicitly on-demand a remeshing iteration like a general-purpose smoothing tool, i.e., outside of a dynamic mesh update. It is possible though to circumvent this by setting the moving interfaces as “Stationary” instead of “User-defined” boundaries. The cell zones must be left as “Deforming” during all the

process. Then it is possible to trigger additional iterations of the dynamic mesh without actually moving the deposit. This way, the remeshing would still be called each time on the deforming cell zones as normally while there is no actual deposit growth. After enough remeshing has been applied, the user-defined deposit-moving routine may be enabled again for a newer deposit expansion.

All the aforementioned smoothing and remeshing techniques may be executed explicitly between the deformation steps  $\vec{r}/n$ . It is recommended here to combine these tools, for instance, by applying 4–6 local face remeshing iterations and then repeating a certain number of times successive alternations of face-swapping and skewness improvement at each deformation step [VI].

The finer the grid resolution, the more unstable the dynamic mesh is. Therefore more number of steps  $n$  and intermediate iterations of smoothing and remeshing may be required. Fortunately, these smoothing and remeshing methods generally improve (within reasonable limits) the mesh quality and their cost are not significant compared to the costs of the flow solving.

#### B.4 Fixing deposit interface mesh instabilities

Even with careful remeshing and smoothing, eventually the dynamic mesh may compromise the CFD model stability. Figure B.4 highlights a remarked peak in the deposit deformation leading to its penetration into the flue gas zone cells. The spring-smoothing method was not capable of adapting the nodes sufficiently. The boundary has moved too suddenly, causing the gas-side cells to turn instead of being pushed away. These cells are said to have “negative volume” or simply to be “negative cells”. The model cannot continue from this point, the CFD solver cannot be executed with any negative cell in the grid.

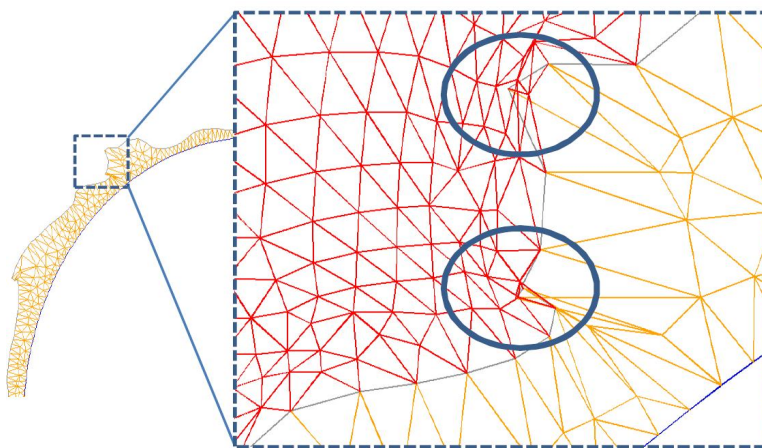


Figure B.4: Formation of negative cells (overlapping of deposits and fluid zones) [III].

The negative cells may be also caused by cracks. If the updating of the node positions is not very smooth (which is the case typically in finer grids), any concave angle between adjacent faces (looking from outside of the deposit) tends to be amplified and to generate self-reinforcing cracks. These cracks lead to the erroneous numeric solving of the flow in the area and eventually the faces of a crack would collapse and generate negative volumes. See Figure B.5.

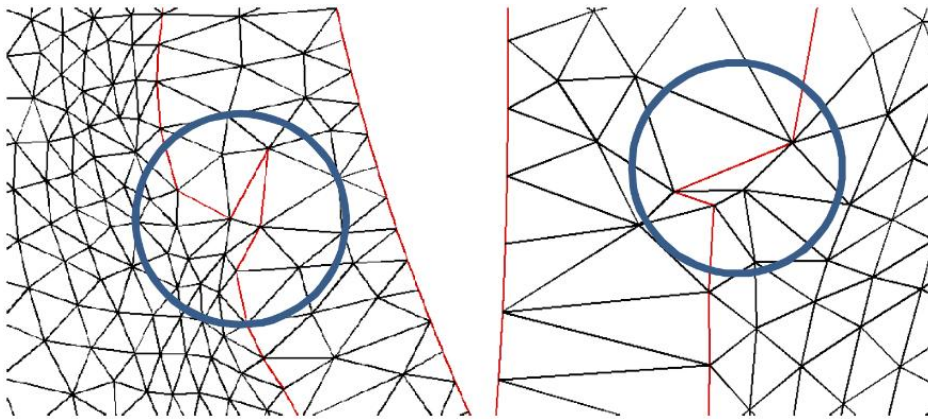


Figure B.5: Crack formation in the deposit-gas interphases [II].

This time, the negative-cell formation is not caused by insufficient remeshing/smoothing, but by the boundary movement only. It is possible to implement an automatic fixing for these cracks by alternating an auxiliary `DEFINE_GRID_MOTION` dynamic mesh routine with the actual deposit growth routine. This auxiliary routine may inspect the surfaces and search for nodes that are surrounded by faces with a concave angle beyond a threshold. Two consecutive faces in an angle  $< 135^\circ$  are prone to form a crack within the next steps, and, for tube-wrapping deposits which have 380 elements or more, it is recommended to consider crack-smoothing even for angles  $< 165^\circ$ . The surface is smoothed by displacing conveniently the nodes of the involved faces towards new positions in such a way that the angle gets closer to  $180^\circ$ . One may certainly argue that this node location fixing, if not done with care, would not respect the deposited mass (i.e., filling in a gap actually falsifies slightly the modeled results with additional deposit material). Nonetheless, for the typically fine meshes that are in need of this growth stabilization, this surface softening supposes negligible errors (especially if executed early, before the cracks grow to the point shown in Figure B.5), and yet allow for the model continuity.

## B.5 Strategy for particularly unstable grids

The stability of the dynamic mesh, although it is usually worse with finer grids, is very case-dependent and universal strategies and smoothing requirements may be difficult to

provide. For instance, in Paper [II] the simulations could continue relatively easily with just  $n = 1$  mesh movement steps per cycle, and applying once only the basic spring smoothing and remeshing. Paper [VI] made further calculations in a similar geometry with a much finer grid, and all the aforementioned methods were required combined to ensure the model stability even with  $n = 8$  steps.

Figure B.6 shows a suggestion of a possible strategy combining all these methods. These blocks may replace the steps 6 and 7 shown in Figure 3.4.

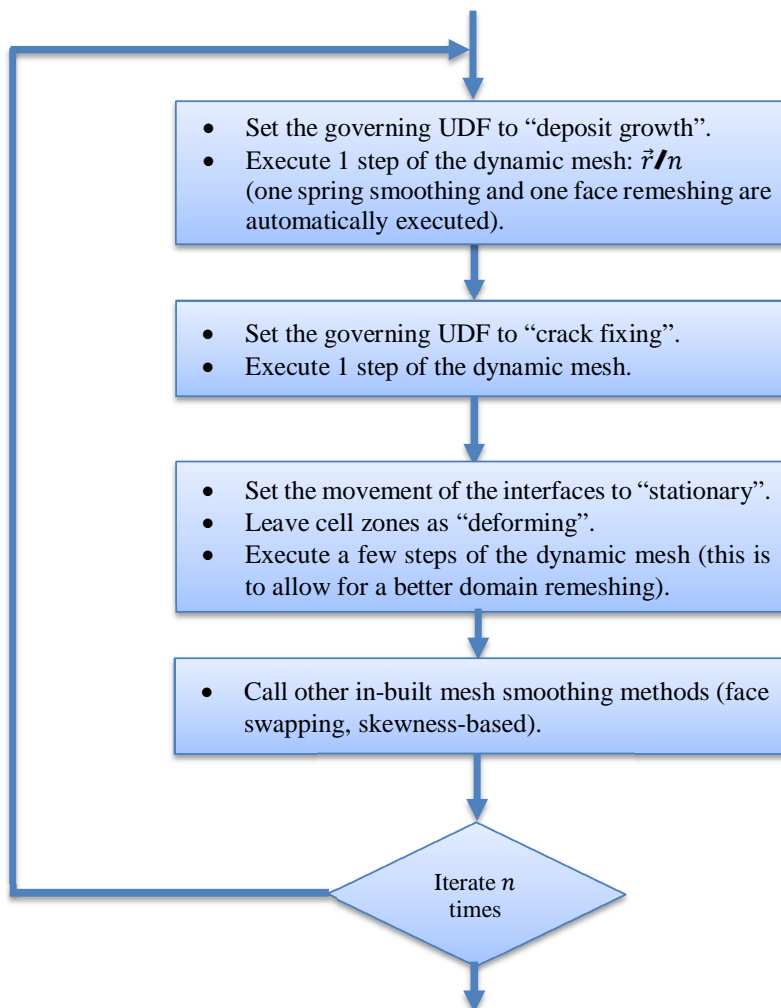


Figure B.6: Suggested possible strategy for the updating of problematic meshes. Only the first block is mandatory, for it represents the actual deposit growth. The remaining blocks are simply suggested and help preserving the mesh quality. Some cases may require multiple repetitions of these smoothing blocks (e.g., Paper [VI]), some other cases may not need those at all and will do sufficiently just with one step of spring smoothing and face remeshing (e.g. Paper [II]).

## References

- [1] L. L. Baxter, "Ash deposit formation and deposit properties. A comprehensive summary of research conducted at Sandia's combustion research facility," Livermore, California, Technical report SAND2000-8253, 2000.
- [2] E. K. Vakkilainen, *Kraft recovery boilers - principles and practice*. Helsinki, Suomen Soodakattilayhdistys, 2005.
- [3] T. Adams, J. Frederick, T. M. Grace, M. Hupa, K. Iisa, A. K. Jones, and H. Tran, *Kraft recovery boilers*. TAPPI Press: Atlanta, 1997.
- [4] R. W. Bryers, "Fireside slagging, fouling, and high-temperature corrosion of heat-transfer surface due to impurities in steam-raising fuels," *Progress in Energy and Combustion Science*, vol. 22, no. 1, pp. 29–120, 1996.
- [5] R. Weber, M. Mancini, N. Schaffel-Mancini, and T. Kupka, "On predicting the ash behaviour using computational fluid dynamics," *Fuel Processing Technology*, vol. 105, pp. 113–128, 2013.
- [6] M. C. van Beek, "Gas-side fouling in heat-recovery boilers," PhD Thesis, Technische Universiteit Eindhoven, 2001.
- [7] A. G. Konstandopoulos, "Particle sticking/rebound criteria at oblique impact," *Journal of Aerosol Science*, vol. 37, no. 3, pp. 292–305, 2006.
- [8] R. Weber, N. Schaffel-Mancini, M. Mancini, and T. Kupka, "Fly ash deposition modelling: Requirements for accurate predictions of particle impaction on tubes using RANS-based computational fluid dynamics," *Fuel*, vol. 108, pp. 586–596, 2013.
- [9] L. L. Baxter, T. Gale, S. Sinquefield, and G. Sclippa, "Influence of ash deposit chemistry and structure on physical and transport properties," in *Developments in Thermochemical Biomass Conversion*, Springer, 1997, pp. 1247–1262.
- [10] Z. Zhan, L. E. Bool, A. Fry, W. Fan, M. Xu, D. Yu, and J. Wendt, "Novel temperature-controlled ash deposition probe system and its application to oxy-coal combustion with 50% inlet O<sub>2</sub>," *Energy & Fuels*, vol. 28, no. 1, pp. 146–154, 2013.
- [11] Z. Zhan, A. Fry, Y. Zhang, and J. Wendt, "Ash aerosol formation from oxy-coal combustion and its relation to ash deposit chemistry," *Proceedings of the Combustion Institute*, vol. 35, no. 2, pp. 2373–2380, 2015.
- [12] Z. Zhan, A. Fry, and J. Wendt, "Coal ash aerosols and ash deposits during air- and oxy-coal combustion," in *Proceedings of the 8th International Symposium on Coal Combustion (8thISCC)*, Beijing, China, 2015.

- [13] G. Schumacher and L. Juniper, "Practical aspects of slagging in operating boilers," in *Proceedings of the 22nd International Conference on Impacts of Fuel Quality on Power Production*, Puchberg, Austria, 2012.
- [14] R. Creelman, C. Ward, and L. Juniper, "Understanding ash deposition in PF furnaces: the connection between coal mineral matter and deposit mineralogy," in *Proceedings of the 22nd International Conference on Impacts of Fuel Quality on Power Production*, Puchberg, Austria, 2012.
- [15] L. Juniper, R. Creelman, C. Ward, and G. Schumacher, "Tools for evaluating slagging in boiler furnaces," in *Proceedings of the 22nd International Conference on Impacts of Fuel Quality on Power Production*, Puchberg, Austria, 2012.
- [16] H. Shiai, K. Tanno, and M. Ikeda, "Estimation of properties of fly ash using the combination method of ash formation model and correlation model," in *Proceedings of the 22nd International Conference on Impacts of Fuel Quality on Power Production*, Puchberg, Austria, 2012.
- [17] K. Janka, A. Raukola, J. Wallén, S. H. Kochesfahani, G. B. Elton, and K. Matzdorf, "A study of recovery boiler fouling tendency in low-load high-solid operations," in *TAPPI Engineering Conference*, Atlanta, GA, 2000.
- [18] P. Mikkonen, E. I. Kauppinen, J. Pyykönen, J. Jokiniemi, M. Aurela, E. K. Vakkilainen, and K. Janka, "Alkali salt ash formation in four Finnish industrial recovery boilers," *Energy & Fuels*, vol. 13, no. 4, pp. 778–795, 1999.
- [19] L. L. Baxter, T. Lind, M. Rumminger, and E. I. Kauppinen, "Particle size distributions in recovery boilers," in *Proceedings of the International Chemical Recovery Conference*, Whistler, Canada, 2001.
- [20] J. Frederick, E. K. Vakkilainen, H. Tran, and S. Lien, "The conditions for boiler bank plugging by submicrometer sodium salt (fume) particles in kraft recovery boilers," *Energy & Fuels*, vol. 18, no. 3, pp. 795–803, 2004.
- [21] T. Tamminen, J. Kiuru, R. Kiuru, K. Janka, and M. Hupa, "Dust and flue gas chemistry during rapid changes in the operation of black liquor recovery boilers. Part 1: Dust composition," *TAPPI*, vol. 1, no. 5, pp. 27–32, 2002.
- [22] A. Leppänen, E. Välimäki, and A. Oksanen, "Modeling of fine fume particles in kraft recovery boiler," in *IRFR Computational Fluid Dynamics Validation Workshop*, Suomen Soodakattilayhdistys, The Finnish Recovery Boiler Committee, and TAPPI.
- [23] N. Vähä-Savo, P. Yrjas, T. Laurén, and M. Hupa, "Fast method for measurement of carry-over in a kraft recovery boiler: 'One-minute' probe," in *Proceedings of the International Chemical Recovery Conference*, Williamsburg, VA, 2010.

- [24] R. R. Horton and E. K. Vakkilainen, "Comparison of simulation results and field measurements of an operating recovery boiler." Report no. 499, The Institute of Paper Science and Technology, Atlanta, GA, 1993.
- [25] A. O. S. Costa, E. C. Biscaia, and E. L. Lima, "Mathematical description of the kraft recovery boiler furnace," *Computers & Chemical Engineering*, vol. 28, no. 5, pp. 633–641, 2004.
- [26] J. Kaila and K. Saviharju, "Comparison of recovery boiler CFD modeling to actual operations," in *PAPTAC Annual Meeting, January 28, Montreal, Canada, 13 p.*, 2015.
- [27] S. Metiäinen, *Soodakattilan Ilmansyöttömallien Kokeellinen Tutkimus, (Experimental Investigation of Recovery Boiler Air Models)*. In Finnish, Doctoral Thesis, 1991.
- [28] W. Roberts, H. Lu, E. Ip, and L. L. Baxter, "Black liquor particle and droplet reactions: experimental and model results," in *Proceedings of the International Chemical Recovery Conference, 45 Years Recovery Boiler Co-operation in Finland*, Lahti, Finland, 2009.
- [29] K. Janka, J. Wallén, and R. Backman, "Prediction of dust content and properties in kraft recovery boilers: comparison of theory and experimental results," *Pulp & Paper Canada*, vol. 105, no. 1, pp. 46–50, 2004.
- [30] A. M. Beckmann, M. Mancini, R. Weber, S. Seebold, and M. Müller, "Measurements and CFD modeling of a pulverized coal flame with emphasis on ash deposition," *Fuel*, vol. 167, pp. 168–179, 2016.
- [31] R. Israel and D. E. Rosner, "Use of a generalized stokes number to determine the aerodynamic capture efficiency of non-stokesian particles from a compressible gas flow," *Aerosol Science and Technology*, vol. 2, no. 1, pp. 45–51, 1982.
- [32] R. Wessel and J. Righi, "Generalized correlations for inertial impaction of particles on a circular cylinder," *Aerosol Science and Technology*, vol. 9, no. 1, pp. 29–60, 1988.
- [33] J. H. Cameron and K. Goerg-Wood, "Role of thermophoresis in the deposition of fume particles resulting from the combustion of high inorganic containing fuels with reference to kraft black liquor," *Fuel Processing Technology*, vol. 60, no. 1, pp. 49–68, 1999.
- [34] A. J. Eskola, J. Jokiniemi, K. E. J. Lehtinen, and E. K. Vakkilainen, "Modelling alkali salt deposition on kraft recovery boiler heat exchangers in the superheater section," in *Proceedings of the International Chemical Recovery Conference*, Tampa, FL, 1998, pp. 469–486.

- [35] A. Fry, J. Wendt, and Z. Zhan, "Predicting particle deposition characteristics on heat transfer surfaces," in *Low Rank Coal Users Seminar*, Busan, Korea, 2015.
- [36] P. Mikkanen, *Fly ash particle formation in kraft recovery boilers*. PhD Thesis, VTT publications, 2000.
- [37] S. Ishigai, S. Nakanishi, T. Fujii, E. Nishikawa, K. Akagawa, and M. Ozawa, *Steam power engineering: thermal and hydraulic design principles*. Cambridge University Press, 1999.
- [38] M. M. Zdravkovich, *Flow around circular cylinders: Volume 2: Applications*, vol. 2. Oxford university press, 2003.
- [39] R. Weber, N. Schaffel-Mancini, M. Mancini, and T. Kupka, "On importance of fluid dynamics in CFD predictions of ash deposits," in *Proceedings of the 22nd International Conference on Impacts of Fuel Quality on Power Production*, Puchberg, Austria, 2012.
- [40] H. B. Vuthaluru and R. Vuthaluru, "Control of ash related problems in a large scale tangentially fired boiler using CFD modelling," *Applied Energy*, vol. 87, no. 4, pp. 1418–1426, 2010.
- [41] A. Leppänen, H. Tran, R. Taipale, E. Välimäki, and A. Oksanen, "Numerical modeling of fine particle and deposit formation in a recovery boiler," *Fuel*, vol. 129, pp. 45–53, 2014.
- [42] A. Leppänen, E. Välimäki, A. Oksanen, and H. Tran, "Effect of temperature on fume formation and deposition - a modeling approach," in *Proceedings of the International Chemical Recovery Conference*, Tampere, Finland: Suomen Soodakattilayhdistys, The Finnish Recovery Boiler Committee, and TAPPI, 2014.
- [43] A. Leppänen, E. Välimäki, A. Oksanen, and H. Tran, "CFD-modeling of fume formation in kraft recovery boilers," *TAPPI*, vol. 12, no. 3, pp. 25–32, 2013.
- [44] A. Leppänen, E. Välimäki, and A. Oksanen, "Modeling fine particles and alkali metal compound behavior in a kraft recovery boiler," *TAPPI*, vol. 11, no. 7, pp. 9–14, 2012.
- [45] A. Leppänen, *Modeling fume particle dynamics and deposition with alkali metal chemistry in kraft recovery boilers*. Tampere University of Technology, PhD Thesis, 2015.
- [46] R. Wessel and L. L. Baxter, "Comprehensive model of alkali-salt deposition in recovery boilers," *TAPPI*, vol. 2, no. 2, pp. 19–24, 2003.
- [47] J. Jokiniemi, J. Pyykönen, P. Mikkanen, and E. I. Kauppinen, "Modeling fume

- formation and deposition in kraft recovery boilers,” *TAPPI*, vol. 79, no. 7, pp. 171–181, 1996.
- [48] S. Balakrishnan, R. Nagarajan, and K. Karthick, “Mechanistic modeling, numerical simulation and validation of slag-layer growth in a coal-fired boiler,” *Energy*, vol. 81, pp. 462–470, 2015.
- [49] B. Li, A. Brink, and M. Hupa, “CFD investigation of slagging on a super-heater tube in a kraft recovery boiler,” *Fuel Processing Technology*, vol. 105, pp. 149–153, 2013.
- [50] J. Pyykönen and J. Jokiniemi, “Modelling alkali chloride superheater deposition and its implications,” *Fuel Processing Technology*, vol. 80, no. 3, pp. 225–262, 2003.
- [51] J. Tomeczek and K. Waclawiak, “Two-dimensional modelling of deposits formation on platen superheaters in pulverized coal boilers,” *Fuel*, vol. 88, no. 8, pp. 1466–1471, 2009.
- [52] Z.-X. Tong, M.-J. Li, Y.-L. He, and H.-Z. Tan, “Simulation of real time particle deposition and removal processes on tubes by coupled numerical method,” *Applied Energy*, pp. 1–13, 2016.
- [53] H. Han, Y. L. He, W. Q. Tao, and Y. S. Li, “A parameter study of tube bundle heat exchangers for fouling rate reduction,” *International Journal of Heat and Mass Transfer*, vol. 72, pp. 210–221, 2014.
- [54] Fluent Inc., *ANSYS Fluent 14.0 user’s manual*. 2011.
- [55] Fluent Inc., *ANSYS Fluent 12 theory guide*. 2009.
- [56] E. Cunningham, “On the Velocity of Steady Fall of Spherical Particles through Fluid Medium,” *Proceedings of the Royal Society A: Mathematical, Physical and Engineering Sciences*, vol. 83, no. 563, pp. 357–365, 1910.
- [57] S. . Morsi and A. . Alexander, “An investigation of particle trajectories in two-phase flow systems,” *Journal of Fluid Mechanics*, vol. 55, no. 2, pp. 193–208, 1972.
- [58] R. A. Millikan, “The isolation of an ion, a precision measurement of its charge, and the correction of Stokes’s law,” *Physical Review (Series I)*, vol. 32, no. 4, pp. 349–397, 1911.
- [59] C. N. Davies, “Definitive equations for the fluid resistance of spheres,” *Proceedings of the Physical Society*, vol. 57, no. 4, pp. 259–270, 1945.

- [60] M. D. Allen and O. G. Raabe, "Re-evaluation of millikan's oil drop data for the motion of small particles in air," *Journal of Aerosol Science*, vol. 13, no. 6, pp. 537–547, 1982.
- [61] R. M. Brach, P. F. Dunn, and X. Li, "Experiments and engineering models of microparticle impact and deposition," *The Journal of Adhesion*, vol. 74, no. 1–4, pp. 227–282, 2000.
- [62] X. Li, P. F. Dunn, and R. M. Brach, "Lycopodium spore impacts onto surfaces," *Atmospheric Environment*, vol. 34, no. 10, pp. 1575–1581, 2000.
- [63] Fluent Inc., *ANSYS Fluent 14.0 UDF manual*. 2011.
- [64] M. García Pérez, E. K. Vakkilainen, and T. Hyppänen, "CFD for deposit formation in kraft recovery boilers," in *Proceedings of the International Chemical Recovery Conference*, Tampere, Finland, 2014: Suomen Soodakattilyhdistys, The Finnish Recovery Boiler Committee, and TAPPI, 2014.
- [65] S. Kerrigan, J. Raynor, and P. Artanis, "Fundamentals of solarite growth and typical locations," *Blizzard Society*, vol. 2, no. 1, pp. 10–20, 2015.
- [66] M. Tuomenoja, E. K. Vakkilainen, and K. Saviharju, "Effect of tube arrangement on superheater heat transfer," in *Proceedings of the 1999 Engineering Conference*, Tappi, Ahlstrom Machinery Corporation, 1999.
- [67] L. Talbot, R. K. Cheng, R. W. Schefer, and D. R. Willis, "Thermophoresis of particles in a heated boundary layer," *Journal of Fluid Mechanics*, vol. 101, no. 4, pp. 737–758, 1980.
- [68] P. Mikkanen, J. Jokiniemi, E. I. Kauppinen, and E. K. Vakkilainen, "Coarse ash particle characteristics in a pulp and paper industry chemical recovery boiler," *Fuel*, vol. 80, no. 7, pp. 987–999, 2001.
- [69] A. Ots, "Thermophysical Properties of Ash Deposit on Boiler Heat Exchanger Surfaces," in *International Conference on Heat Exchanger Fouling and Cleaning*, Crete Island, Greece, 2011, pp. 150–155.
- [70] E. K. Vakkilainen, *Chemical pulping part 2: Recovery of chemicals and energy*, vol. 2. Helsinki Paper Engineers' Association/Paperi ja Puu Oy; p. 28-33, 2008.
- [71] MEMS & Nanotechnology, "Material properties database: Silicon Dioxide (SiO<sub>2</sub>), film." [Online]. Available: <https://www.memsnet.org/material/silicondioxidesio2film/>. [Accessed: 27-Apr-2016].
- [72] P. Miskiewicz, S. Kotarba, J. Jung, T. Marszalek, M. Mas-Torrent, E. Gomar-

- Nadal, D. B. Amabilino, C. Rovira, J. Veciana, W. Maniukiewicz, and J. Ulanski, "Influence of SiO<sub>2</sub> surface energy on the performance of organic field effect transistors based on highly oriented, zone-cast layers of a tetrathiafulvalene derivative," *Journal of Applied Physics*, vol. 104, no. 5, pp. 1–5, 2008.
- [73] B. Ahlborn, M. L. Seto, and B. R. Noack, "On drag, Strouhal number and vortex street structure," *Fluid Dynamic Research*, vol. 30, pp. 379–399, 2002.
- [74] C. H. K. Williamson and G. L. Brown, "A series in  $1/\sqrt{\text{Re}}$  to represent the Strouhal–Reynolds number relationship of the cylinder wake," *Journal of Fluids and Structures*, vol. 12, no. 8, pp. 1073–1085, 1998.
- [75] V. Gnielinski, A. Zukauskas, and A. Skrinska, *Heat exchanger design handbook, vol. 2: Fluid mechanics and heat transfer*. VDI-Verlag des Verein Deutscher Ingenieure, 1983.
- [76] D. Talbor, "Hardness of solids," *Endeavour*, vol. 13, pp. 27–32, 1954.
- [77] V. Iva, R. Betism, and K. Epierda, *Dynamic mesh practice guidelines*. RBB S.A.D., 2004.



## ACTA UNIVERSITATIS LAPPEENRANTAENSIS

677. NUUTINEN, PASI. Power electronic converters in low-voltage direct current distribution – analysis and implementation. 2015. Diss.
678. RUSATSI, DENIS. Bayesian analysis of SEIR epidemic models. 2015. Diss.
679. STRAND, ELSI. Enhancement of ultrafiltration process by pretreatment in recovery of hemicelluloses from wood extracts. 2016. Diss.
680. TANNINEN, PANU. Press forming of paperboard – advancement of converting tools and process control. 2015. Diss.
681. VALTONEN, PETRI. Distributed energy resources in an electricity retailer's short-term profit optimization. 2015. Diss.
682. FORSTRÖM-TUOMINEN, HEIDI. Collectiveness within start up-teams – leading the way to initiating and managing collective pursuit of opportunities in organizational contexts. 2015. Diss.
683. MAGUYA, ALMASI. Use of airborne laser scanner data in demanding forest conditions. 2015. Diss.
684. PEIPPO, JUHA. A modified nominal stress method for fatigue assessment of steel plates with thermally cut edges. 2015. Diss.
685. MURASHKO, KIRILL. Thermal modelling of commercial lithium-ion batteries. 2016. Diss.
686. KÄRKKÄINEN, TOMMI. Observations of acoustic emission in power semiconductors. 2016. Diss.
687. KURVINEN, EMIL. Design and simulation of high-speed rotating electrical machinery. 2016. Diss.
688. RANTAMÄKI, JUKKA. Utilization of statistical methods for management in the forest industry. 2016. Diss.
689. PANOVA, YULIA. Public-private partnership investments in dry ports – Russian logistics markets and risks. 2016. Diss.
690. BAHARUDIN, EZRAL. Real-time simulation of multibody systems with applications for working mobile vehicles. 2016. Diss.
691. MARTIKAINEN, SOILI. Development and effect analysis of the Asteri consultative auditing process – safety and security management in educational institutions. 2016. Diss.
692. TORVINEN, PEKKA. Catching up with competitiveness in emerging markets – An analysis of the role of the firm's technology management strategies. 2016. Diss.
693. NORONTAUS, ANNUKKA. Oppisopimuskoulutus yritysten tuottamana koulutuspalveluna: tavoitteista vaikutuksiin. 2016. Diss.
694. HALMINEN, OSKARI. Multibody models for examination of touchdown bearing systems. 2016. Diss.
695. TALONPOIKA, ANNA-MARIA. Financial working capital – management and measurement. 2016. Diss.

696. INKINEN, HENRI. Intellectual capital, knowledge management practices and firm performance. 2016. Diss.
697. YANG, XIAOCHEN. Development of a welding production quality control and management system model for China. 2016. Diss.
698. LEMINEN, VILLE. Leak-proof heat sealing of press-formed paperboard trays. 2016. Diss.
699. LAAKSONEN, LAURI. Spectral retinal image processing and analysis for ophthalmology. 2016. Diss.
700. OINONEN, MINNA. Management of customer co-development in business-to-business markets. 2016. Diss.
701. ALATALO, SARA-MAARIA. Hydrothermal carbonization in the synthesis of sustainable porous carbon materials. 2016. Diss.
702. UZHEGOV, NIKITA. Design and material selection of high-speed rotating electrical machines. 2016. Diss.
703. RICHTER, CHRIS. Digital collaborations and entrepreneurship – the role of shareconomy and crowdsourcing in the era of smart city. 2016. Diss.
704. JAFARI, SHILA. Investigation of adsorption of dyes onto modified titanium dioxide. 2016. Diss.
705. PATEL, YOGINI. Computational modelling of non-equilibrium condensing steam flows in low-pressure steam turbines. 2016. Diss.
706. LEVCHUK, IRINA. Titanium dioxide based nanomaterials for photocatalytic water treatment. 2016. Diss.
707. AMOUR, IDRIS. Variational ensemble kalman filtering applied to data assimilation problems in computational fluid dynamics. 2016. Diss.
708. SHESTAKOVA, MARINA. Ultrasound-assisted electrochemical treatment of wastewaters containing organic pollutants by using novel Ti/Ta<sub>2</sub>O<sub>5</sub>-SnO<sub>2</sub> electrodes. 2016. Diss.
709. OLEKSIENKO, OLGA. Physico-chemical properties of sol-gel synthesized titanosilicates for the uptake of radionuclides from aqueous solutions. 2016. Diss.
710. PATALA, SAMULI. Advancing sustainability-oriented innovations in industrial markets. 2016. Diss.
711. KUORIKOSKI, TERO. Kohti resonoivaa urheilujohtamista – Tavoitteen muodostuminen urheilun kentässä. 2016. Diss.
712. LAHTELA, VILLE. Improving the properties of solid Scots pine (*Pinus sylvestris*) wood by using modification technology and agents. 2016. Diss.
713. NEVARANTA, NIKO. Online time and frequency domain identification of a resonating mechanical system in electric drives. 2016. Diss.
714. FANG, CHAO. Study on system design and key technologies of case closure welding for ITER correction coil. 2016. Diss.

